MODELING OF THE OPTICAL PROPERTIES OF

NONSPHERICAL PARTICLES IN THE ATMOSPHERE

A Dissertation

by

GUANG CHEN

Submitted to the Office of Graduate Studies
of Texas A&M University
in partial fulfillment of the requirements for the degree of

DOCTOR OF PHILOSOPHY

August 2007

Major Subject: Atmospheric Sciences

MODELING OF THE OPTICAL PROPERTIES OF

NONSPHERICAL PARTICLES IN THE ATMOSPHERE

A Dissertation

by

GUANG CHEN

Submitted to the Office of Graduate Studies
of Texas A&M University
in partial fulfillment of the requirements for the degree of

DOCTOR OF PHILOSOPHY

Approved by:

Chair of Committee,	Ping Yang
Committee Members,	George W. Kattawar
	Thomas Wilheit
	Gerald North
Head of Department,	Richard Orville

August 2007

Major Subject: Atmospheric Sciences

ABSTRACT

Modeling of the Optical Properties of Nonspherical Particles

in the Atmosphere**.** (August 2007)

Guang Chen, B.S., Jilin University;

M.S., University of Southern California

Chair of Advisory Committee: Dr. Ping Yang

The single scattering properties of atmospheric particles are fundamental to radiative simulations and remote sensing applications. In this study, an efficient technique, namely, the pseudo-spectral time-domain (PSTD) method which was first developed to study acoustic wave propagation, is applied to the scattering of light by nonspherical particles with small and moderate size. Five different methods are used to discretize Maxwell's equations in the time domain. The perfectly matched layer (PML) absorbing boundary condition is employed in the present simulation for eliminating spurious wave propagations caused by the spectral method.

A 3-D PSTD code has been developed on the basis of the five aforementioned discretization methods. These methods provide essentially the same solutions in both absorptive and nonabsorptive cases. In this study, the applicability of the PSTD method is investigated in comparison with the Mie theory and the T-matrix method. The effects of size parameter and refractive index on simulation accuracy are discussed. It is shown that the PSTD method is quite accurate when it is applied to the scattering of light by

spherical and nonspherical particles, if the spatial resolution is properly selected. Accurate solutions can also be obtained from the PSTD method for size parameter of 80 or refractive index of 2.0+j0.

Six ice crystal habits are defined for the PSTD computational code. The PSTD results are compared with the results acquired from the finite difference time domain (FDTD) method at size parameter 20. The PSTD method is about 8-10 times more efficient than the conventional FDTD method with similar accuracy. In this study, the PSTD is also applied to the computation of the phase functions of ice crystals with a size parameter of 50.

Furthermore, the PSTD, the FDTD, and T-matrix methods are applied to the study of the optical properties of horizontally oriented ice crystals. Three numerical schemes for averaging horizontal orientations are developed in this study. The feasibility of using equivalent circular cylinders as surrogates of hexagonal prisms is discussed. The horizontally oriented hexagonal plates and the equivalent circular cylinders have similar optical properties when the size parameter is in the region about from 10 to 40. Otherwise, the results of the two geometries are substantially different.

DEDICATION

This dissertation is dedicated to my family who always supported me through my life.

ACKNOWLEDGEMENTS

I would like to thank many people for helping me during my doctoral education. I would especially like to thank my advisor, Dr. Ping Yang, and the members of my committee, Dr. George W. Kattawar, Dr. Thomas Wilheit and Dr. Gerald North for their guidance and support.

I wish to thank all the people in our group for their help on my research work.

Finally, I would like to thank my family for their support in my life.

TABLE OF CONTENTS

LIST OF FIGURES

FIGURE   Page

FIGURE   Page

CHAPTER I

INTRODUCTION

Cirrus clouds, covering more than 20% of the globe [1-3], influence the terrestrial climate system on all scales through their radiative influence. For example, in the tropic region, the thermal structure of the upper troposphere is substantially impacted by the solar absorption of cirrus clouds [4]. Influences of radiative and microphysical properties of cirrus clouds on weather and climate evolutions are considered to be an outstanding problem in atmospheric research [5]. Significant research efforts have been made to understand the radiative properties of ice clouds from various perspectives [6-13]. Thus, the single scattering properties of cloud particles have been widely studied, as they are fundamental to the study of the radiative properties of cirrus clouds [14-26]. Additionally, the single scattering of ice crystals in the atmosphere is required for the remote sensing of clouds [27-29]. Recently, a great deal of research work has been dedicated to the direct and indirect effects and forcing of aerosols on climate change [30-35]. According to satellite observations, the impact of aerosols on weather evolution is believed to be significant. However, inadequate understanding of aerosol optical and microphysical characteristics makes the study difficult. Therefore, it is necessary to improve the current knowledge about the scattering of light by aerosols.

The single-scattering properties of atmospheric particles depend strongly upon

_____

This dissertation follows the style of *Journal of Quantitative Spectroscopy & Radiative Transfer.*

incident wavelength, refractive index, particle size, shape, orientation, and composition. However, in the atmosphere, particle characteristics are very complicated. As described by Hemysfield and Platt [36], shapes and sizes of ice crystals in cirrus clouds are strongly impacted by temperature and supersaturation. Ice crystals have various shapes, for example, solid and hollow hexagonal columns, droxtals, various bullet rosettes and aggregates. The sizes of ice particles range from smaller than one micron to several thousand microns. Shapes, compositions and sizes of aerosols, particularly mineral aerosols, are also highly variable [37]. The uncertainty of particle sizes and shapes makes the light scattering study difficult. Therefore, various theories and numerical methods have been developed to understand the single-scattering properties of atmospheric particles. When the maximum dimensions of particles are much smaller than the incident wavelength, Rayleigh theory pioneered by Rayleigh in 1871 [38] can be used to provide non-analytical solutions. The analytical solutions in the case of homogeneous spherical particles can be derived from the conventional Lorenz-Mie (or Mie) theory [39]. Improved Mie theory has also been developed for absorbing sphere [40] and coated sphere in an absorbing medium [41]. Furthermore, scattering properties of double sphere system [42], spheroids [43] and Chebyshev particles [44] can also be obtained analytically from theoretical methods.

However, most atmospheric particles with complex geometries cannot be solved analytically. Therefore, numerical methods have been developed for nonspherical particles. When the maximum dimension of a particle is larger than approximately 20 times the incident wavelength, the geometric optics method (GOM) provides solutions

for arbitrary convex nonspherical particles with acceptable accuracy. Takano and Liou applied GOM method to single-scattering of hexagonal ice crystals [45]. In 1996 Geometric-Optics-integral-equation method, an improved GOM method developed by Yang, was applied to nonspherical ice crystals [46]. Then, this method has been used for various ice crystals with complex geometries [47, 48].

In order to study the scattering of light by atmospheric particles with complex geometries, for example, ice crystals in cirrus clouds and mineral aerosols, the finite-difference time-domain method (FDTD) was developed. This method can be applied to arbitrary geometries with various compositions because electromagnetic boundary conditions need not be satisfied on the particle surface. The finite-difference time domain method was developed by Yee in 1966 to directly solve Maxwell's equation in the time domain [49]. Then, Yang introduced this method for light scattering by nonspherical ice crystals [19, 25, 50-51]. Single-scattering properties of aerosols can also be calculated by this method [52]. However, the FDTD method becomes impractical for large particles due to the tedious calculations associated with this size. According to numerical experiments, the FDTD method is applicable when the maximum dimension of particles is smaller than approximately 6 times the incident wavelength.

The T-matrix method [53] is a very efficient technique for symmetric particles with moderate size by rigorously solving Maxwell's equations, for example, finite circular cylinders and spheroids. However, when imaginary part of particle refractive index is very small, the conventional T-matrix method becomes ill-conditioned due to the strong impact of the ripple structure [54]. Fortunately, an improved T-matrix method has been

developed for nonabsorbing particles by substituting a matrix inversion technique associated with a lower triangular-upper triangular factorization for the conventional Gaussian elimination [54]. In atmospheric science, the T-matrix method is widely applied to scattering of light by aerosols with fixed or random orientations in which particles are approximated as symmetric geometries [55-57]. Although, this method is considered to be applicable for arbitrary geometries, for complex shapes, the algorithm becomes impractical because the calculation is difficult to converge.

There are several other methods applicable for studying light scattering, for example, the anomalous diffraction theory (ADT) [58, 59] and the discrete-dipole approximation (DDA) [60, 61]. However, for particles with complex geometries and compositions, and size in the range of approximately 6λ to 20λ (λ is the incident wavelength), there is no efficient method to be used. Unfortunately, in the atmosphere, many aerosols and ice crystals are this kind of particle. In this study, we will use the pseudo-spectral time-domain (PSTD) method pioneered by Liu for studying acoustic wave propagations [62, 63] to calculate the single-scattering properties of arbitrarily shaped particles with moderate size. Similar to the FDTD method, this method solves Maxwell's equations in the time domain. In the PSTD method, a high order accurate approximation of spatial derivative on the basis of the spectral method is employed. In contrast to the FDTD algorithm, the PSTD method is much more efficient since a coarse grid resolution can be used for acceptable accuracy due to the application of the new approximation. However, for an unbounded problem, this method suffers from a "wraparound effect." The wraparound effect describes a case in which the solution is

contaminated by spurious wave propagations pertaining to the spatial periodicity of the Fast Fourier Transform (FFT) used in the spectral method. Fortunately, perfectly matched layer (PML) boundary conditions [64, 65] can be used to eliminate the spurious wave propagations. Another limitation is that the accuracy of the PSTD method in a Cartesian grid may degrade due to Gibb's phenomenon caused by discontinuities of electromagnetic properties on a particle surface. In this study, we will investigate the influence of Gibb's phenomenon on calculation accuracy. For the partially empty cells located near the scatter surface, we will evaluate the mean electromagnetic properties in terms of permittivity and permeability to decrease Gibb's phenomenon.

The content of this dissertation is organized as follows: Chapter II generalizes formulations of the PSTD method in the Cartesian coordinate for scattering of light by atmospheric particles. Five different schemes are applied to discretize Maxwell's equations in the time domain. PML boundary conditions are used to terminate the computation domain and eliminate the wraparound effect. Transformation of near field to far field is implemented by a surface integration technique. In Chapter III, applicability of a 3-D PSTD code for dielectric particles is discussed. Accuracy of the five discretization methods is reviewed. Solutions of the PSTD method and the Mie theory are compared in terms of phase functions of spheres with various sizes and refractive indices. Influence of spatial resolution and refractive index on simulation accuracy is also discussed. Applicability of the PSTD for nonspherical particles is investigated in comparison with the T-matrix method. Phase functions of spheroids and circular cylinders with various aspect ratios are calculated from these two methods at

refractive index of 1.38+ j3.9×10^{-9}, which is a typical refractive index of oceanic aerosols. Chapter IV applies the PSTD method for ice crystals. Six geometries-hexagonal plate, hexagonal column, hollow hexagonal column, bullet rosette, aggregate and droxtal-are defined according to observations in cirrus clouds. Phase functions of these ice crystals from the PSTD and FDTD methods are compared at an incident wavelength of 3.7 μm and size parameter 20. Furthermore, the PSTD method is applied for ice crystals with size parameter 50. In Chapter V, the PSTD, FDTD and T-matrix methods are used to study horizontally oriented ice crystals. In this study, three numerical schemes are applied to the average of the particle orientations. The orientations can be arbitrary but confined to be horizontal for computing the scattering properties of ice crystals. Also discussed is the feasibility for using circular cylinders as surrogates of horizentally oriented hexagonal ice crystals in the computation of the scattering properties.

CHAPTER II

PSEUDO-SPECTRAL TIME-DOMAIN METHOD APPLIED TO LIGHT SCATTERING BY ATMOSPHERIC PARTICLES WITH ARBITRARY GEOMETRIES AND COMPOSITIONS IN THREE-DIMENSIONAL SPACE

2.1 Introduction

The finite-difference time-domain (FDTD) method has been widely used to solve Maxwell's equations in the time domain. This method has also been demonstrated to be accurate and reliable for propagations of acoustic waves in various media. In atmospheric science, the FDTD method is applied to study the scattering of light by small nonspheric particles in the atmosphere. The grid spatial resolution used in simulations determines the accuracy of this method. The typical grid spatial resolution of FDTD is about 20 cells per minimum wavelength according to numerous numerical experiments. However, the computation demand increases by the fourth order of particle size increase for 3D problems. Therefore, if the particle size is large, the FDTD method becomes impractical for the 3D case. Generally, the conventional FDTD method is applied to simulations with size parameters smaller than 20. Another limitation of the conventional FDTD method is the relatively large dispersion errors which accumulate with time steps [66]. In calculation with large time steps, a finer spatial grid resolution is necessary for acceptable accuracy. Therefore, the computation demand also goes up with

the increase of the spatial resolution. Alternatively, the pseudo-spectral time-domain (PSTD) method pioneered by Liu [63, 67] in 1997 and 1998 to solve Maxwell's equations and study propagations of acoustic waves in absorptive media can be applied to study the scattering problems with moderate sizes. In this method, spatial derivatives with high order accuracy are approximated on the basis of the spectral method. No accumulated dispersion errors are introduced in this approximation. Therefore, the PSTD method is much more efficient than the conventional FDTD method because a coarse spatial grid resolution can be used for acceptable accuracy. Another major advantage is that the PSTD method could be applied to arbitrary geometries. Similar to the FDTD method, the PSTD method discretizes the computational domain containing a scattering particle by using a grid mesh. At each grid point, electromagnetic parameters, namely permittivity, permeability, and conductivity, are specified. Because the electromagnetic boundary conditions do not need to be imposed at the particle surface in the PSTD method, it is applicable to arbitrarily shaped or inhomogeneous objects.

The spectral method was first discussed by Kreiss and Oliger [66] in 1972, who used Fourier series to approximate derivatives. In the same year, Orszag [68] also studied the advantage of the spectral method based on Chebyshev polynomials. In 1988, the spectral method was applied to solve partial differential equations in fluid dynamics [69]. In 1982 another kind of spectral method, k-space method, was developed and applied by Bojarski [70] to solve scalar acoustic waves. Then Liu [62, 71] applied k-space method to study electromagnetic and elastic waves. If the coefficients in wave equations vary smoothly, high order spatial derivatives can be obtained from both

spectral methods with about 2 to 4 grid points per minimum wavelength. In the spectral methods, the fast Fourier transform (FFT) pioneered by Cooley and Tukey [72] is employed to make the calculation more efficient. However, for an unbounded problem, the PSTD method suffers from a "wraparound effect." The wraparound effect describes a case in which the solution is contaminated by spurious wave propagations pertaining to the spatial periodicity of the FFT used in the spectral method. Fortunately, the perfectly matched layer (PML) absorbing boundary conditions [64, 65] can be used to eliminate the spurious wave propagations. Thus, it appears feasible that PSTD can be applied to the scattering of light by nonspherical particles with moderate size parameters.

This chapter is organized as follows. In the second section, physical fundamentals of the PSTD method are discussed. Then, in the third section, the finite different approximation and the spectral method are reviewed. In the fourth section, the PSTD method is used to calculate the frequency dependent near field. In this section, Maxwell curl equations are discretized in the time domain by several numerical schemes, and the corresponding time-marching equations are also given. Then transformation of the near field from time domain to frequency domain is reviewed. The fifth section recapitulates the uniaxial anisotropic perfectly matched layer (UPML) absorbing boundary condition [65], which is used to truncate the wraparound effect and eliminate the outgoing wave propagations on the computational domain boundary. The sixth section first reviews the definitions of several important scattering properties, namely the amplitude and the phase matrixes; then, recapitulates the surface integration technique, which is used to map the near field to the far field.

2.2 Physical background of the PSTD method

All electromagnetic phenomena can be described by Maxwell's equations; however, these equations are not independent of each other. Maxwell's divergence equations (Gauss's law) can be obtained from Maxwell curl equations (Faraday's law and Ampere's law). Therefore, the PSTD method can be used to study light scattering of nonspherical atmospheric particles by solving the corresponding Maxwell curl equations in time domain. As shown in Fig. A.1, the PSTD method discretizes the computational domain containing a scattering particle by using a grid mesh. The electromagnetic properties, namely permittivity, permeability, and conductivity, are specified at each grid point, and the scattering particle is defined in the grid domain. The incident wave is introduced into the computational domain and interacts with the scattering particle. As shown in Fig. A.2a, in the FDTD algorithm, the electric field components and the magnetic field components are located at the edges and at the surface centers of the grid cell, respectively [49]. However, the PSTD method applies a centered grid scheme that specifies all field components at the centers of the grid cells, as shown in Fig. A.2b. Because of this advantage, the PSTD algorithm is significantly simplified, particularly for the calculation in an anisotropic medium [65]. Furthermore, the centered grid scheme can also remove the singularity problem for electromagnetic waves in cylindrical coordinates [73].

In the present study, the rectangular Cartesian grid is employed in the PSTD method. However, for a medium with large contrasts in electromagnetic properties, the accuracy of the PSTD method in Cartesian grid may be degraded due to Gibb's

phenomenon caused by the discontinuities on the scattering particle surface. This phenomenon describes the case in which the Fourier series cannot converge to a function with discontinuity points. In an extreme case, such as the case of a perfect conductor, significant Gibb's phenomenon will be observed, and the PSTD simulation results would be incorrect. Furthermore, similar to the conventional FDTD method, the PSTD method also encounters the problem of staircasing approximation for a curved particle surface in a rectangular mesh. To avoid Gibb's phenomenon and the staircasing errors, significant efforts have been focused on the multidomain Chebyshev PSTD method in general curvilinear coordinates [73-77]. Although this elegant approach is more accurate, it is relatively inflexible when scatters have various sizes and arbitrary geometries and the algorithm becomes much more complicated. Particularly, the implementation of the PML boundary condition in curvilinear coordinates is much more complicated than in the Cartesian grid. Fortunately, in this study, ice crystals and most aerosols are nonferromagnetic and their electromagnetic properties are not so different from the vacuum. For the partially empty cells located near the scatter surface, the mean electromagnetic properties in terms of permittivity and permeability can be evaluated to decrease the discontinuities. For these reasons, the medium discontinuities and staircasing errors do not cause serious problems in this study. Thus, the rectangular Cartesian grid is still most appropriate for the present study.

In the PSTD method, the finite difference method and the spectral method are employed to approximate the temporal and spatial derivatives and discretize the corresponding Maxwell curl equations in time and space domains, respectively. As the

initial condition, a known plane incident wave, which propagates toward the scattering particle, is introduced into the computational domain. At the next time step, the excited electromagnetic field at every grid point can be obtained from the initial conditions by using the discretized Maxwell curl equations. Iteratively, the excited electromagnetic fields at any time can be computed from the corresponding fields at the last time step. Therefore, in the computational domain, the excited fields as functions of time can be calculated from the time-marching iterations. If a pulse source is chosen as the incident wave, the iterations stop when the electromagnetic fields in the computational domain are significantly weak. Otherwise, no convergent scattered fields can be obtained.

The near fields calculated from the preceding discretized Maxwell curl equations are in the time domain. The time dependent solutions should be transformed into corresponding results in the frequency domain in order to study the single-scattering properties. The discrete Fourier transform is used to implement this transform. If initial excitation is a Gaussian pulse, theoretically, the frequency spectrum of the time-dependent results should cover most of frequencies. However, in the simulation, the available frequency spectrum depends strongly on the width of the Gaussian pulse. The impertinent pulse width can cause serious numerical aliasing and dispersion, which degrade the accuracy of the numerical results. More details will be discussed in section 2.6.

In order to obtain the amplitude matrix and other scattering properties, the near fields in frequency domain should be transformed into the corresponding far fields. Both surface and volume integrations are discussed by Yang and Liou [19] for transforming

the near field to the far field. Because the volume integration approach is less accurate for the large refractive index [78] and has a relatively tedious computation, the surface integration approach was chosen for this study.

According to the preceding discussion, the PSTD method applied to scattering of light by atmospheric particles includes the following steps:

1. Discretize the computational domain containing the scattering particle by a rectangular grid mesh and obtain the time-dependent near fields from the time-marching iteration.

2. Transform the near fields from time domain to frequency domain.

3. Transform the near fields to the corresponding far fields.

2.3 The finite difference approximation and the spectral method approximation

Similar to the FDTD method, the temporal derivatives of Maxwell equations are approximated in terms of the finite difference approximation in the PSTD method. The finite difference approximation can be derived from Taylor series expansions. Keeping spatial variable x fixed at x_n, the Taylor series expansion of $f(x,t)$ about time t_i to time $t_i + \dfrac{\Delta t}{2}$ can be written as follows:

$$f(t_i + \frac{\Delta t}{2})\Big|_{x_n} = f(t_i)\Big|_{x_n} + \frac{\Delta t}{2}\frac{\partial f(t_i)}{\partial t}\Big|_{x_n} + \frac{1}{2}(\frac{\Delta t}{2})^2\frac{\partial^2 f(t_i)}{\partial t^2}\Big|_{x_n} + \frac{1}{6}(\frac{\Delta t}{2})^3\frac{\partial^3 f(t_1)}{\partial t^3}\Big|_{x_n}, \quad (2.1)$$

where Δt is the time interval between two time steps and t_1 locates in the range of t_i to $t_i + \dfrac{\Delta t}{2}$. Similarly, the Taylor series expansion of $f(x,t)$ about time $t_i - \dfrac{\Delta t}{2}$ to time t_i is given as follows:

$$f(t_i - \frac{\Delta t}{2})\Big|_{x_n} = f(t_i)\Big|_{x_n} - \frac{\Delta t}{2}\frac{\partial f(t_i)}{\partial t}\Big|_{x_n} + \frac{1}{2}(\frac{\Delta t}{2})^2\frac{\partial^2 f(t_i)}{\partial t^2}\Big|_{x_n} - \frac{1}{6}(\frac{\Delta t}{2})^3\frac{\partial^3 f(t_2)}{\partial t^3}\Big|_{x_n}, \quad (2.2)$$

where $t_2 \in (t_i, t_i + \dfrac{\Delta t}{2})$. Subtracting Eq. (2.2) from Eq. (2.1), we have:

$$f(t_i + \frac{\Delta t}{2})\bigg|_{x_n} - f(t_i - \frac{\Delta t}{2})\bigg|_{x_n} = \Delta t \frac{\partial f(t_i)}{\partial t}\bigg|_{x_n} + \frac{1}{3}(\frac{\Delta t}{2})^3 \frac{\partial^3 f(t_3)}{\partial t^3}\bigg|_{x_n}, \qquad (2.3)$$

where $t_3 \in (t_i - \frac{\Delta t}{2}, t_i + \frac{\Delta t}{2})$. It is a straightforward calculation to obtain the first partial

time derivate of $f(x,t)$ at time t_i:

$$\frac{\partial f(t_i)}{\partial t}\bigg|_{x_n} = \frac{f(t_i + \frac{\Delta t}{2}) - f(t_i - \frac{\Delta t}{2})}{\Delta t}\bigg|_{x_n} + O[(\frac{\Delta t}{2})^2], \qquad (2.4)$$

As shown in Eq. (2.4), the finite difference approximation of the first partial derivative

has second-order accuracy.

In contrast to the FDTD method, the spatial derivative terms in Maxwell's

equations are approximated by the spectral method based on the Fourier series in the

PSTD technique. According to partial integration, consider the spatial partial derivatives

of $f(x,t)$, which are transformed in *K*-space by the forward Fourier transform, keeping

time fixed at t_i:

$$\int_{-\infty}^{\infty} \frac{\partial f(x,t_i)}{\partial x} e^{-2\pi j Kx} dx = f(x,t_i) e^{-2\pi j Kx}\bigg|_{-\infty}^{\infty} + 2\pi j k \int_{-\infty}^{\infty} f(x,t_i) e^{-2\pi j Kx} dx, \qquad (2.5)$$

where j denotes imaginary unit. If $f(x,t)$ is zero at infinite boundary, it is possible to

simplify Eq. (2.5) as follows:

$$\int_{-\infty}^{\infty} \frac{\partial f(x,t_i)}{\partial x} e^{-2\pi j K x} dx = 2\pi j k \int_{-\infty}^{\infty} f(x,t_i) e^{-2\pi j K x} dx, \tag{2.6}$$

The spatial derivatives of $f(x,t)$ in x-space were obtained by applying the inverse Fourier transform to Eq. (2.6):

$$\frac{\partial f(x,t_i)}{\partial x} = \int_{-\infty}^{\infty} [2\pi j k \int_{-\infty}^{\infty} f(x,t_i) e^{-2\pi j K x} dx] e^{2\pi j K x} dK. \tag{2.7}$$

The right side of Eq. (2.7) is the exact expression of the spatial partial derivatives which can be viewed as an approximation with infinite-order accuracy. However, in the numerical algorithm, the computational domain is not infinite. On the basis of the preceding discussion, it is apparent that the computational domain is discretized by the grid mesh. Therefore, the discrete Fourier transform is employed to represent the spatial derivatives of the discrete data, substituting for the conventional Fourier transform. By analogy with Eq. (2.6), the expression of the partial derivatives of a discrete function $f(x_n,t_i)$ in k-space was obtained keeping time fixed at t_i:

$$\sum_{n=0}^{N-1} \frac{\partial f(x_n,t_i)}{\partial x} e^{\frac{2\pi j n m}{N}} = 2\pi j K_m \sum_{n=0}^{N-1} f(x_n,t_i) e^{\frac{2\pi j n m}{N}}, \tag{2.8}$$

where N is total grid points number along x direction, and K_m is the corresponding Fourier variable. In Eq. (2.8), K_m is defined as:

$$K_m = \frac{m}{N\Delta x},$$

(2.9)

where Δx is the spatial interval between to two grid points. Applying the inverse discrete Fourier transform to Eq. (2.8) gives the approximations of the spatial derivatives of $f(x_n, t_i)$ in the x-space:

$$\frac{\partial f(x_n, t_i)}{\partial x} = \frac{1}{N} \sum_{m=0}^{N-1} e^{\frac{2\pi j n m}{N}} [2\pi j K_m \sum_{n=0}^{N-1} f(x_n, t_i) e^{-\frac{2\pi j n m}{N}}].$$

(2.10)

In contrast to the finite difference approximation of the spatial derivative at grid point x_n, whose value only depends on the two values, $f(x_n - \Delta x/2, t_i)$ and $f(x_n + \Delta x/2, t_i)$, the spectral method approximation of the spatial derivative at every grid point depends on $f(x, t_i)$ values at all grid points. Therefore, the spectral method approximation has a much higher order accuracy than the finite difference approximation. Furthermore, in the spectral method, the fast Fourier transform [72], which reduces the number of computation needed from $2N^2$ to $2N \log_2(N)$, is used to make the numerical calculation more efficient.

In order to study the accuracy of the spectral method, the PSTD method is first used to simulate the transmission and reflection processes of a Gaussian pulse on a dielectric medium surface in one-dimensional case. In this simulation, the spatial interval Δx is $0.015m$, and the permittivity of medium is given as $\varepsilon = \varepsilon_0 (1.5 + 0.0j)$. The reflection coefficient from the one-dimensional PSTD method is compared with the corresponding analytic values in the frequency domain in Fig. A.4 As shown in this figure, the differences between the PSTD results and analytical solutions increase with the frequency of the incident wave. The relative error is less than 2% with frequency 4 GHz. In contrast to the finite different technique for which the spatial grid resolution is about 15 cells per wavelength, the corresponding spatial grid resolution of the spectral method at the incident frequency 4 GHz is about 4 cells per minimum wavelength.

2.4 The discretized time-domain equations for the near field

As discussed in the preceding section, the PSTD method is applied to the scattering of light by nonspherical atmospheric particles by solving Maxwell curl equations in the time domain. In the present study, all ice crystals and most aerosol particles, such as various marine, dust-like, and soil aerosols, are inhomogeneous and nonferromagnetic, and their electromagnetic properties are isotropic. Therefore, the current density terms in Maxwell's equations can be ignored, and the permeability μ is selected as μ_0, which is the permeability in vacuum. Maxwell curl equations are simplified as:

$$\varepsilon_0 \varepsilon \frac{\partial \bar{E}}{\partial t} = \nabla \times \bar{H}, \qquad\qquad (2.11a)$$

$$\mu_0 \frac{\partial \bar{H}}{\partial t} = -\nabla \times \bar{E}, \qquad\qquad (2.11b)$$

where ε_0 denotes the permittivity in vacuum and ε is relative permittivity of the dielectric medium. However, some atmospheric particles are absorptive; thus, the permittivity is complex, and the imaginary part causes the absorption. Yang and Liou [19] first introduced a method in 1996 to deal with the calculation associated with complex permittivity in the FDTD algorithm. Following this method, the PSTD method can be applied to the cases of absorption. If the harmonic time-dependent factor of the electromagnetic fields in frequency domain is defined as $\exp(-j\omega t)$, in which ω is angular frequency, the refractive index has a positive imaginary part, and the refractive index m and the relative permittivity ε are defined as:

$$\varepsilon = \varepsilon_r + j\varepsilon_i, \qquad\qquad (2.12a)$$

$$m = m_r + jm_i, \qquad\qquad (2.12b)$$

where the subscripts r and i denote the real part and imaginary part, respectively. The relations between permittivity and refractive index are represented:

$$\varepsilon_r = m_r^{\,2} - m_i^{\,2}, \qquad\qquad (2.13a)$$

$$\varepsilon_i = 2m_r m_i. \qquad\qquad (2.13b)$$

Substituting Eq. $(2.12a)$ into Eq. $(2.11a)$ and using $\exp(-j\omega t)$ as the harmonic time-dependent factor, we have:

$$\varepsilon_0\varepsilon_r\frac{\partial\vec{E}}{\partial t} + kc\varepsilon_0\varepsilon_i\vec{E} = \nabla\times\vec{H}, \qquad\qquad (2.14)$$

where $k = \dfrac{2\pi}{\lambda}$ is the wave number of the incident source in vacuum, λ is the corresponding wavelength, and c denotes the light speed in vacuum.

Before discretizing the calculation domain with the rectangular grid mesh to obtain the time-marching iterative equations of Maxwell curl equations, it is necessary to discuss the introduction of the incident source into the PSTD simulation. In the FDTD method applied to scattering of light by particles with linear electromagnetic properties, the total (incident+scattered) field and scattered field method (TF/SF) [19] is employed to introduce incident wave. As shown in Fig. A.3a, a connecting surface, the Huygens surface, is defined in the computation domain to connect the total field region and the scattered field region in this method. Inside the Huygens surface, total fields are calculated, and outside the surface, only scattered fields are calculated. The incident waves are introduced on the Huygens surface. However, if the incident wave is also introduced by using the same TF/SF method in the PSTD method, a serious Gibb's phenomenon will occur in the Fourier transform used in the spectral method due to field

discontinuity at the Huygens surface. Furthermore, the simulation will be contaminated by the noise caused by the Gibb's phenomenon. In order to eliminate the Gibb's phenomenon, there are two approaches for introducing the incident wave by the TF/SF method. As shown in Fig. A.3b, a connecting region is employed to connect the total field region and the scattered field region [79] in the first approach, and a new field $\vec{E}^{con}$ is defined:

$$\vec{E}^{con} = \rho\vec{E}^{i} + \vec{E}^{s}, \qquad\qquad (2.15)$$

where superscripts i and s denote the incident field and scattering field, respectively, and ρ is a continuous function, which smoothly changes from 0 to 1 in the connecting region. The variable ρ is 1 in the total field region, and is 0 in the scattered field region. Therefore, $\vec{E}^{con}$ is also a continuous function in every region, and the Gibb's phenomenon caused by the discontinuity is eliminated. According to the definition in Eq. (2.15), it is apparent that $\vec{E}^{con}$ becomes the total field, inside the connecting region, and, as well, $\vec{E}^{con}$ becomes the scattered field outside the region. In the connecting region, there are several choices for ρ—half of cosine function, half of a Gaussian function, half of the Blackman-Harris window function, and an integral form of the Blackman-Harris window function. However, an extra computational error will be created in the connecting region due to Gibb's phenomenon no matter which function is chosen. In addition, for this approach, the computational domain is larger than the conventional

approach due to the Huygens region, and the algorithm is relatively complicated. Therefore, another approach was selected to introduce the incident wave. Because only the medium with linear electromagnetic properties is considered in this investigation, the other approach can express the total field as the superposition of the incident and scattered field. Maxwell curl equations of the total field can be rewritten as:

$$\varepsilon_0\varepsilon_r\frac{\partial \vec{E}^s}{\partial t} + \varepsilon_0\varepsilon_r\frac{\partial \vec{E}^i}{\partial t} + kc\varepsilon_0\varepsilon_i\vec{E}^s + kc\varepsilon_0\varepsilon_i\vec{E}^i = \nabla \times \vec{H}^s + \nabla \times \vec{H}^i, \qquad (2.16a)$$

$$\mu_0\frac{\partial \vec{H}^s}{\partial t} + \mu_0\frac{\partial \vec{H}^i}{\partial t} = -\nabla \times \vec{E}^s - \nabla \times \vec{E}^i, \qquad (2.16b)$$

For the incident field, the corresponding Maxwell curl equations are

$$\mu_0\frac{\partial \vec{H}^i}{\partial t} = -\nabla \times \vec{E}^i, \qquad (2.17a)$$

$$\varepsilon_0\frac{\partial \vec{E}^i}{\partial t} = \nabla \times \vec{H}^i, \qquad (2.17b)$$

Substituting Eqs. (2.17) into Eqs. (2.16) produces Maxwell curl equations for the split scattered and incident fields:

$$\varepsilon_0\varepsilon_r\frac{\partial \vec{E}^s}{\partial t} + kc\varepsilon_0\varepsilon_i\vec{E}^s = \nabla \times \vec{H}_s + \varepsilon_0(1-\varepsilon_r)\frac{\partial \vec{E}^i}{\partial t} - kc\varepsilon_0\varepsilon_i\vec{E}^i, \qquad (2.18a)$$

$$\mu_0 \frac{\partial \bar{H}^s}{\partial t} = -\nabla \times \bar{E}^s, \qquad\qquad (2.18b)$$

In the total field region, the analytic values of the incident electrical field are used in $2.18a$, and total field is evaluated. In the scattered field and boundary regions, only the scattered fields are computed, and the incident terms in Eq. $(2.18a)$ are zero. By this method, only scattered field, which is continuous in all computational domain, is simulated by the PSTD method, and any incident waves can be introduced with the analytic values. No Gibb's phenomenon occurs on the Huygens surface.

In order to discretize Maxwell's equations in time domain, the finite different approximation is used. The finite different analog of Eqs. $(2.18a)$ and $(2.18b)$ in each Cartesian components can be written as:

$$
\begin{aligned}
&E_x^{s(n+1)}(I,J,K) \\
&= a1(I,J,K)E_x^{s(n)}(I,J,K) \\
&+ b1(I,J,K)\frac{\partial E_x^{i(n+\frac{1}{2})}(I,J,K)}{\partial t} + c1(I,J,K)E_x^{i(n+\frac{1}{2})}(I,J,K) \\
&+ d1(I,J,K)\sqrt{\frac{\mu_0}{\varepsilon_0}}\{\frac{\partial H_z^{s(n+\frac{1}{2})}(I,J,K)}{\partial y} - \frac{\partial H_y^{s(n+\frac{1}{2})}(I,J,K)}{\partial z}\},
\end{aligned}
\qquad (2.19a)
$$

$$
\begin{aligned}
&E_y^{s(n+1)}(I,J,K) \\
&= a1(I,J,K)E_y^{s(n)}(I,J,K) \\
&+ b1(I,J,K)\frac{\partial E_y^{i(n+\frac{1}{2})}(I,J,K)}{\partial t} + c1(I,J,K)E_y^{i(n+\frac{1}{2})}(I,J,K)
\end{aligned}
$$

$$+ d1(I,J,K)\sqrt{\frac{\mu_0}{\varepsilon_0}}\{\frac{\partial H_x^{s(n+\frac{1}{2})}(I,J,K)}{\partial z} - \frac{\partial H_z^{s(n+\frac{1}{2})}(I,J,K)}{\partial x}\},\tag{2.19b}$$

$$E_z^{s(n+1)}(I,J,K)$$
$$= a1(I,J,K)E_z^{s(n)}(I,J,K)$$
$$+ b1(I,J,K)\frac{\partial E_z^{i(n+\frac{1}{2})}(I,J,K)}{\partial t} + c1(I,J,K)E_z^{i(n+\frac{1}{2})}(I,J,K)$$
$$+ d1(I,J,K)\sqrt{\frac{\mu_0}{\varepsilon_0}}\{\frac{\partial H_y^{s(n+\frac{1}{2})}(I,J,K)}{\partial x} - \frac{\partial H_x^{s(n+\frac{1}{2})}(I,J,K)}{\partial y}\},\tag{2.19c}$$

And

$$\sqrt{\frac{\mu_0}{\varepsilon_0}}H_x^{s(n+\frac{1}{2})}(I,J,K)$$
$$= \sqrt{\frac{\mu_0}{\varepsilon_0}}H_x^{s(n-\frac{1}{2})}(I,J,K)$$
$$- c\Delta t\{\frac{\partial E_z^{s(n)}(I,J,K)}{\partial y} - \frac{\partial E_y^{s(n)}(I,J,K)}{\partial z}\},\tag{2.20a}$$

$$\sqrt{\frac{\mu_0}{\varepsilon_0}}H_y^{s(n+\frac{1}{2})}(I,J,K)$$
$$= \sqrt{\frac{\mu_0}{\varepsilon_0}}H_y^{s(n-\frac{1}{2})}(I,J,K)$$
$$- c\Delta t\{\frac{\partial E_x^{s(n)}(I,J,K)}{\partial z} - \frac{\partial E_z^{s(n)}(I,J,K)}{\partial x}\},\tag{2.20b}$$

$$\sqrt{\frac{\mu_0}{\varepsilon_0}} H_z^{s(n+\frac{1}{2})}(I,J,K)$$

$$= \sqrt{\frac{\mu_0}{\varepsilon_0}} H_z^{s(n-\frac{1}{2})}(I,J,K)$$

$$- c\Delta t \{ \frac{\partial E_x^{s(n)}(I,J,K)}{\partial x} - \frac{\partial E_z^{s(n)}(I,J,K)}{\partial y} \}, \tag{2.20c}$$

where superscript n, $n+1$, and $n\pm\frac{1}{2}$ denote time step number, and indices (I,J,K) denotes the grid points location. In Eqs. $(2.19a)$ through $(2.19c)$ and $(2.20a)$ through $(2.20c)$, the spatial derivatives can be approximated on the basis of the spectral method, and the terms associated with the incident electrical field can be obtained by analytic values. Additionally, by approximating the temporal derivatives of the incident electrical field in terms of the finite different method, Eq. $(2.18a)$ can be written as another form of the finite different analog:

$$E_x^{s(n+1)}(I,J,K)$$
$$= a2(I,J,K)E_x^{s(n)}(I,J,K)$$
$$+ b2(I,J,K)E_x^{i(n+1)}(I,J,K) + c2(I,J,K)E_x^{i(n)}(I,J,K)$$
$$+ d2(I,J,K)\sqrt{\frac{\mu_0}{\varepsilon_0}} \{ \frac{\partial H_z^{s(n+\frac{1}{2})}(I,J,K)}{\partial y} - \frac{\partial H_y^{s(n+\frac{1}{2})}(I,J,K)}{\partial z} \}, \tag{2.21a}$$

$$E_y^{s(n+1)}(I,J,K)$$
$$= a2(I,J,K)E_y^{s(n)}(I,J,K)$$
$$+ b2(I,J,K)E_y^{i(n+1)}(I,J,K) + c2(I,J,K)E_y^{i(n)}(I,J,K)$$

$$+d2(I,J,K)\sqrt{\frac{\mu_0}{\varepsilon_0}}\{\frac{\partial H_x^{s(n+\frac{1}{2})}(I,J,K)}{\partial z}-\frac{\partial H_z^{s(n+\frac{1}{2})}(I,J,K)}{\partial x}\},\qquad(2.21b)$$

$$E_z^{s(n+1)}(I,J,K)$$
$$=a2(I,J,K)E_z^{s(n)}(I,J,K)$$
$$+b2(I,J,K)E_z^{i(n+1)}(I,J,K)+c2(I,J,K)E_z^{i(n)}(I,J,K)$$
$$+d2(I,J,K)\sqrt{\frac{\mu_0}{\varepsilon_0}}\{\frac{\partial H_y^{s(n+\frac{1}{2})}(I,J,K)}{\partial x}-\frac{\partial H_x^{s(n+\frac{1}{2})}(I,J,K)}{\partial y}\},\qquad(2.21c)$$

2.4.1 Scheme 1

The equation of the E_x^s component is chosen as an example. Integration of the x component of the Eq. ($2.18a$) on the temporal interval $[n\Delta t,(n+1)\Delta t]$ leads to the following:

$$\int_{n\Delta t}^{(n+1)\Delta t}\{\varepsilon_0\bar{\varepsilon}_r(I,J,K)\frac{\partial E_x^s(I,J,K)}{\partial t}+kc\varepsilon_0\bar{\varepsilon}_i(I,J,K)E_x^s(I,J,K)\}dt$$
$$=\int_{n\Delta t}^{(n+1)\Delta t}\{\frac{\partial H_z^s(I,J,K)}{\partial y}-\frac{\partial H_y^s(I,J,K)}{\partial z}\}dt$$
$$+\int_{n\Delta t}^{(n+1)\Delta t}\{\varepsilon_0(1-\bar{\varepsilon}_r(I,J,K))\frac{\partial E_x^i(I,J,K)}{\partial t}-kc\varepsilon_0\bar{\varepsilon}_i(I,J,K)E_x^i(I,J,K)\}dt,\qquad(2.22)$$

The mean values of the real and imaginary parts of the permittivity at the grid points denoted by index (I,J,K), $\bar{\varepsilon}_r(I,J,K)$ and $\bar{\varepsilon}_i(I,J,K)$, can be obtained by:

$$\bar{\varepsilon}_r(I,J,K) = \frac{\displaystyle\int\limits_{(I-1)\Delta x}^{I\Delta x}\int\limits_{(J-1)\Delta y}^{J\Delta y}\int\limits_{(K-1)\Delta z}^{K\Delta z}\varepsilon_r(x,y,z)dxdydz}{\Delta x\Delta y\Delta z}, \qquad (2.23a)$$

$$\bar{\varepsilon}_i(I,J,K) = \frac{\displaystyle\int\limits_{(I-1)\Delta x}^{I\Delta x}\int\limits_{(J-1)\Delta y}^{J\Delta y}\int\limits_{(K-1)\Delta z}^{K\Delta z}\varepsilon_i(x,y,z)dxdydz}{\Delta x\Delta y\Delta z}. \qquad (2.23b)$$

In the present scheme, the temporal derivatives are discretized by the following equations:

$$\int_{n\Delta t}^{(n+1)\Delta t}\frac{\partial E_x^s(I,J,K)}{\partial t}dt = E_x^{s(n+1)}(I,J,K) - E_x^{s(n)}(I,J,K), \qquad (2.24a)$$

$$\int_{n\Delta t}^{(n+1)\Delta t}E_x^s(I,J,K)dt = \frac{\Delta t}{2}(E_x^{s(n+1)}(I,J,K) + E_x^{s(n)}(I,J,K)), \qquad (2.24b)$$

$$\int_{n\Delta t}^{(n+1)\Delta t}\frac{\partial E_x^i(I,J,K)}{\partial t}dt = \Delta t\frac{\partial E_x^{i(n+\frac{1}{2})}(I,J,K)}{\partial t}, \qquad (2.24c)$$

$$\int_{n\Delta t}^{(n+1)\Delta t}E_x^i(I,J,K)dt = \Delta t E_x^{i(n+\frac{1}{2})}(I,J,K), \qquad (2.24d)$$

$$\int_{n\Delta t}^{(n+1)\Delta t} \frac{\partial H_z^s(I,J,K)}{\partial y} dt = \Delta t \frac{\partial H_z^{s(n+\frac{1}{2})}(I,J,K)}{\partial y},$$

$$(2.24e)$$

$$\int_{n\Delta t}^{(n+1)\Delta t} \frac{\partial H_y^s(I,J,K)}{\partial z} dt = \Delta t \frac{\partial H_y^{s(n+\frac{1}{2})}(I,J,K)}{\partial z}.$$

$$(2.24f)$$

Substituting Eqs. $(2.24a)$ through $(2.24f)$ into Eq. (2.22), the coefficients of Eqs. $(2.19a)$ through $(2.19c)$ can be obtained as:

$$a1(I,J,K) = \frac{2\bar{\varepsilon}_r(I,J,K) - kc\bar{\varepsilon}_i(I,J,K)\Delta t}{2\bar{\varepsilon}_r(I,J,K) + kc\bar{\varepsilon}_i(I,J,K)\Delta t},$$

$$(2.25a)$$

$$b1(I,J,K) = \frac{2(1 - \bar{\varepsilon}_r(I,J,K))\Delta t}{2\bar{\varepsilon}_r(I,J,K) + kc\bar{\varepsilon}_i(I,J,K)\Delta t},$$

$$(2.25b)$$

$$c1(I,J,K) = -\frac{2kc\bar{\varepsilon}_i(I,J,K)\Delta t}{2\bar{\varepsilon}_r(I,J,K) + kc\bar{\varepsilon}_i(I,J,K)\Delta t},$$

$$(2.25c)$$

$$d1(I,J,K) = \frac{2c\Delta t}{2\bar{\varepsilon}_r(I,J,K) + kc\bar{\varepsilon}_i(I,J,K)\Delta t}.$$

$$(2.25d)$$

2.4.2 Scheme 2

In this scheme, before integrating on the temporal interval $[n\Delta t, (n+1)\Delta t]$, the x

component of the Eq. (2.18a) is first multiplied by a factor of $\exp(\bar{\tau} \cdot t)$ where $\bar{\tau} = kc\bar{\varepsilon}_i(I,J,K)/\bar{\varepsilon}_r(I,J,K)$. Therefore, the Eq. (2.22) can be rewritten in a compact form as:

$$\int_{n\Delta t}^{(n+1)\Delta t} \{\varepsilon_0\bar{\varepsilon}_r(I,J,K)\frac{\partial[E_x^s(I,J,K)\exp(\bar{\tau}(I,J,K)t)]}{\partial t}\}dt$$

$$= \int_{n\Delta t}^{(n+1)\Delta t} \{\frac{\partial H_z^s(I,J,K)}{\partial y} - \frac{\partial H_y^s(I,J,K)}{\partial z}\} \exp(\bar{\tau}(I,J,K)t)dt$$

$$+ \int_{n\Delta t}^{(n+1)\Delta t} \{\varepsilon_0(1-\bar{\varepsilon}_r(I,J,K))\frac{\partial E_x^i(I,J,K)}{\partial t}\} \exp(\bar{\tau}(I,J,K)t)dt$$

$$- \int_{n\Delta t}^{(n+1)\Delta t} \{kc\varepsilon_0\bar{\varepsilon}_i(I,J,K)E_x^i(I,J,K)\} \exp(\bar{\tau}(I,J,K)t)dt, \qquad (2.26)$$

For this scheme, the discretizations of the temporal derivatives of Eq. (2.26) can be expressed as follows:

$$\int_{n\Delta t}^{(n+1)\Delta t} \frac{\partial[E_x^s(I,J,K)\exp(\bar{\tau}(I,J,K)t)]}{\partial t}dt$$

$$= \exp(\bar{\tau}(I,J,K)(n+1)\Delta t)E_x^{s(n+1)}(I,J,K)$$

$$- \exp(\bar{\tau}(I,J,K)n\Delta t)E_x^{s(n)}(I,J,K), \qquad (2.27a)$$

$$\int_{n\Delta t}^{(n+1)\Delta t} \frac{\partial E_x^i(I,J,K)}{\partial t} \exp(\bar{\tau}(I,J,K)t)dt$$

$$= \frac{\partial E_x^{i(n+\frac{1}{2})}(I,J,K)}{\partial t} \exp(\bar{\tau}(I,J,K)(n+\frac{1}{2})\Delta t)\Delta t, \qquad (2.27b)$$

$$\int_{n\Delta t}^{(n+1)\Delta t} E_x^i(I,J,K)\exp(\overline{\tau}(I,J,K)t)dt$$

$$= E_x^{i(n+\frac{1}{2})}(I,J,K)\exp(\overline{\tau}(I,J,K)(n+\frac{1}{2})\Delta t)\Delta t, \qquad (2.27c)$$

$$\int_{n\Delta t}^{(n+1)\Delta t} \frac{\partial H_z^s(I,J,K)}{\partial y}\exp(\overline{\tau}(I,J,K)t)dt$$

$$= \frac{\partial H_z^{s(n+\frac{1}{2})}(I,J,K)}{\partial y}\exp(\overline{\tau}(I,J,K)(n+\frac{1}{2})\Delta t)\Delta t, \qquad (2.27d)$$

$$\int_{n\Delta t}^{(n+1)\Delta t} \frac{\partial H_y^s(I,J,K)}{\partial z}\exp(\overline{\tau}(I,J,K)t)dt$$

$$= \frac{\partial H_y^{s(n+\frac{1}{2})}(I,J,K)}{\partial z}\exp(\overline{\tau}(I,J,K)(n+\frac{1}{2})\Delta t)\Delta t, \qquad (2.27e)$$

Substituting Eqs. $(2.27a) - (2.27e)$ into Eq. (2.26) gives the coefficients of the Eqs. $(2.19a) - (2.19c)$ as:

$$a1(I,J,K) = \exp(-\overline{\tau}(I,J,K)\Delta t), \qquad (2.28a)$$

$$b1(I,J,K) = \frac{1-\overline{\varepsilon}_r(I,J,K)}{\overline{\varepsilon}_r(I,J,K)}\Delta t\exp(-\frac{\overline{\tau}(I,J,K)\Delta t}{2}), \qquad (2.28b)$$

$$c1(I,J,K) = \frac{-kc\overline{\varepsilon}_i(I,J,K)}{\overline{\varepsilon}_r(I,J,K)}\Delta t\exp(-\frac{\overline{\tau}(I,J,K)\Delta t}{2}), \qquad (2.28c)$$

$$d1(I,J,K) = \frac{-c\Delta t}{\bar{\varepsilon}_r(I,J,K)} \exp(-\frac{\bar{\tau}(I,J,K)\Delta t}{2}). \qquad (2.28d)$$

2.4.3 Scheme 3

In this scheme, Eq. (2.26) is discretized by approximating the temporal derivatives with the following expressions:

$$\int_{n\Delta t}^{(n+1)\Delta t} \frac{\partial E_x^i(I,J,K)}{\partial t} \exp(\bar{\tau}(I,J,K)t)dt$$

$$= \frac{\partial E_x^{i(n+\frac{1}{2})}(I,J,K)}{\partial t} \frac{\exp(\bar{\tau}(I,J,K)(n+1)\Delta t) - \exp(\bar{\tau}(I,J,K)n\Delta t)}{\bar{\tau}(I,J,K)}, \qquad (2.29a)$$

$$\int_{n\Delta t}^{(n+1)\Delta t} E_x^i(I,J,K) \exp(\bar{\tau}(I,J,K)t)dt$$

$$= E_x^{i(n+\frac{1}{2})}(I,J,K) \frac{\exp(\bar{\tau}(I,J,K)(n+1)\Delta t) - \exp(\bar{\tau}(I,J,K)n\Delta t)}{\bar{\tau}(I,J,K)}, \qquad (2.29b)$$

$$\int_{n\Delta t}^{(n+1)\Delta t} \frac{\partial H_z^s(I,J,K)}{\partial y} \exp(\bar{\tau}(I,J,K)t)dt$$

$$= \frac{\partial H_z^{s(n+\frac{1}{2})}(I,J,K)}{\partial y} \frac{\exp(\bar{\tau}(I,J,K)(n+1)\Delta t) - \exp(\bar{\tau}(I,J,K)n\Delta t)}{\bar{\tau}(I,J,K)}, \qquad (2.29c)$$

$$\int_{n\Delta t}^{(n+1)\Delta t} \frac{\partial H_y^s(I,J,K)}{\partial z} \exp(\bar{\tau}(I,J,K)t)dt$$

$$= \frac{\partial H_y^{s(n+\frac{1}{2})}(I,J,K)}{\partial z} \frac{\exp(\overline{\tau}(I,J,K)(n+1)\Delta t) - \exp(\overline{\tau}(I,J,K)n\Delta t)}{\overline{\tau}(I,J,K)}. \qquad (2.29d)$$

Using these expressions, the coefficients in Eqs. ($2.19a$) through ($2.19c$) are given as follows:

$$a1(I,J,K) = \exp(-\overline{\tau}(I,J,K)\Delta t), \qquad (2.30a)$$

$$b1(I,J,K) = \frac{(1 - \overline{\varepsilon}_r(I,J,K))(1 - \exp(-\overline{\tau}(I,J,K)\Delta t))}{kc\overline{\varepsilon}_i(I,J,K)}, \qquad (2.30b)$$

$$c1(I,J,K) = -(1 - \exp(-\overline{\tau}(I,J,K)\Delta t)), \qquad (2.30c)$$

$$d1(I,J,K) = \frac{(1 - \exp(-\overline{\tau}(I,J,K)\Delta t))}{k\overline{\varepsilon}_i(I,J,K)}. \qquad (2.30d)$$

2.4.4 Scheme 4

This scheme is similar to scheme 1, except that finite different approximation was used to express the temporal derivatives of the incident field. In this scheme, Eq. (2.22) can be rewritten into the form of Eq. ($2.21a$) by replacing Eqs. ($2.24c$) and ($2.24d$) with the following expressions:

$$\int_{n\Delta t}^{(n+1)\Delta t} \frac{\partial E_x^i(I,J,K)}{\partial t} dt = E_x^{i(n+1)}(I,J,K) - E_x^{i(n)}(I,J,K), \qquad (2.31a)$$

$$\int_{n\Delta t}^{(n+1)\Delta t} E_x^i(I,J,K) dt = \frac{\Delta t}{2}(E_x^{i(n+1)}(I,J,K) + E_x^{i(n)}(I,J,K)). \qquad (2.31b)$$

Discretizing Eq. (2.22) by the present scheme gives the coefficients of Eqs. (2.21a)

through (2.21c) as the following:

$$a2(I,J,K) = \frac{2\bar{\varepsilon}_r(I,J,K) - kc\bar{\varepsilon}_i(I,J,K)\Delta t}{2\bar{\varepsilon}_r(I,J,K) + kc\bar{\varepsilon}_i(I,J,K)\Delta t}, \qquad (2.32a)$$

$$b2(I,J,K) = \frac{2(1 - \bar{\varepsilon}_r(I,J,K)) - kc\bar{\varepsilon}_i(I,J,K)\Delta t}{2\bar{\varepsilon}_r(I,J,K) + kc\bar{\varepsilon}_i(I,J,K)\Delta t}, \qquad (2.32b)$$

$$c2(I,J,K) = \frac{2(\bar{\varepsilon}_r(I,J,K) - 1) - kc\bar{\varepsilon}_i(I,J,K)\Delta t}{2\bar{\varepsilon}_r(I,J,K) + kc\bar{\varepsilon}_i(I,J,K)\Delta t}, \qquad (2.32c)$$

$$d2(I,J,K) = \frac{2c\Delta t}{2\bar{\varepsilon}_r(I,J,K) + kc\bar{\varepsilon}_i(I,J,K)\Delta t}. \qquad (2.32d)$$

2.4.5 Scheme 5

In this scheme, Eq. (2.26) is rewritten into a more compact form:

$$\int_{n\Delta t}^{(n+1)\Delta t} \{\varepsilon_0 \bar{\varepsilon}_r(I,J,K) \frac{\partial [E_x^s(I,J,K)\exp(\bar{\tau}(I,J,K)t)]}{\partial t}\}dt$$

$$= \int_{n\Delta t}^{(n+1)\Delta t} \{\frac{\partial H_z^s(I,J,K)}{\partial y} - \frac{\partial H_y^s(I,J,K)}{\partial z}\}\exp(\bar{\tau}(I,J,K)t)dt$$

$$- \int_{n\Delta t}^{(n+1)\Delta t} \{\varepsilon_0 \bar{\varepsilon}_r(I,J,K) \frac{\partial [E_x^i(I,J,K)\exp(\bar{\tau}(I,J,K)t)]}{\partial t}\}dt$$

$$+ \int_{n\Delta t}^{(n+1)\Delta t} \{\varepsilon_0 \frac{\partial E_x^i(I,J,K)}{\partial t}\}\exp(\bar{\tau}(I,J,K)t)dt, \tag{2.33}$$

Similar to scheme 2, the left side and the first term of the right side of Eq. (2.33) can be discretized by the Eqs. $(2.27a)$, $(2.27d)$, and $(2.27e)$. However, the terms associated with the incident electrical field are approximated as follows:

$$\int_{n\Delta t}^{(n+1)\Delta t} \frac{\partial [E_x^i(I,J,K)\exp(\bar{\tau}(I,J,K)t)]}{\partial t}dt$$

$$= \exp(\bar{\tau}(I,J,K)(n+1)\Delta t)E_x^{i(n+1)}(I,J,K)$$

$$- \exp(\bar{\tau}(I,J,K)n\Delta t)E_x^{i(n)}(I,J,K), \tag{2.34a}$$

$$\int_{n\Delta t}^{(n+1)\Delta t} \frac{\partial E_x^i(I,J,K)}{\partial t}\exp(\bar{\tau}(I,J,K)t)dt$$

$$= \exp(\bar{\tau}(I,J,K)(n+\frac{1}{2})\Delta t)\{E_x^{i(n+1)}(I,J,K) - E_x^{i(n)}(I,J,K)\}. \tag{2.34b}$$

Therefore, the coefficients of Eqs. $(2.21a) - (2.21c)$ are obtained as follows:

$$a2(I,J,K) = \exp(-\bar{\tau}(I,J,K)\Delta t), \tag{2.35a}$$

$$b2(I,J,K) = \frac{\exp(-\frac{\overline{\tau}(I,J,K)\Delta t}{2}) - \overline{\varepsilon}_r(I,J,K)}{\overline{\varepsilon}_r(I,J,K)},$$ (2.35b)

$$c2(I,J,K) = \frac{-\exp(-\frac{\overline{\tau}(I,J,K)\Delta t}{2}) + \overline{\varepsilon}_r(I,J,K)\exp(-\overline{\tau}(I,J,K)\Delta t)}{\overline{\varepsilon}_r(I,J,K)}\Delta t,$$ (2.35c)

$$d2(I,J,K) = \frac{-c\Delta t}{\overline{\varepsilon}_r(I,J,K)}\exp(-\frac{\overline{\tau}(I,J,K)\Delta t}{2}).$$ (2.35d)

Following the preceding schemes, Maxwell's equations can be discretized in the time domain to obtain the finite different analog of Eqs. (2.18a) and (2.18b); however, to obtain a stable PSTD scheme, the temporal interval Δt must satisfy a stability condition. Similar to the stability condition of the FDTD method [80], the stability condition of the PSTD method can be obtained by the dispersion analysis [67]. For three-dimensional computation, the stability condition of the Fourier PSTD method in Cartesian coordinate is given by:

$$c\Delta t \leq \frac{2}{\pi\sqrt{\frac{1}{\Delta x^2} + \frac{1}{\Delta y^2} + \frac{1}{\Delta z^2}}}.$$ (2.36)

As shown in Eq. (2.18a), any incident source can be introduced into the PSTD

simulations. In the present study, a Gaussian pulse is chosen as the incident source, which is given by:

$$E^i(t) = \exp[-(\frac{t-t_i}{t_w})^2],$$

(2.37)

where t_i denotes the initial time of the pulse and t_w denotes the width of the pulse. By ignoring the phase shift, in frequency domain, this Gaussian pulse can be expressed as:

$$E^i(\omega) = \frac{2\sqrt{\pi}}{\omega_p} \exp[-(\frac{\omega}{\omega_p})^2],$$

(2.38)

where $\omega_p = \frac{2}{t_w}$. Therefore, the frequency spectrum depends on the pulse width t_w. As shown in Eq. (2.38), the amplitude of the ω component in the pulse dramatically decreases by t_w. By choosing the pulse width t_w too narrow, the accuracy of the simulation may degrade due to the corresponding small amplitude of the ω component in frequency domain. However, if the pulse width is too wide, a longer computation time is needed. In the present study, the pulse width t_w is given by $t_w = \frac{\lambda}{2c}$. The corresponding ω_p is $\frac{4c}{\lambda}$.

Following the preceding PSTD method, it is possible to compute the near fields

in the time domain. Therefore, it is necessary to transform the solutions in the time domain to the counterparts in the frequency domain. In the present study, this transformation is implemented by the discrete Fourier transform. If $f(l\Delta t)$ is used to denote any components of the near fields in time domain, the corresponding results $F(\omega)$ in the frequency domain are given by:

$$F(\omega) = \sum_{l=0}^{L} f(l\Delta t) \exp(j\omega l\Delta t),\qquad\qquad(2.39)$$

where L denotes the total number of the time steps in the simulation. In practice, the field values $F(\omega)$ calculated by Eq. (2.39) will be normalized by the corresponding incident wave in the frequency domain, which locates at the center of the computation domain.

2.5 Absorbing boundary conditions in the PSTD method

The PSTD method requires an appropriate absorbing boundary condition, which is applied to eliminating the wraparound effect and truncating the outgoing fields at the computational boundary. In the present study, an absorbing boundary, namely the perfectly matched layer (PML) boundary condition, is employed. The PML boundary condition was first developed by Berenger [64, 81] in 1994 and 1996. In this technique, an absorbing medium backed by a perfectly conducting layer is arranged at the outside of the computational domain to absorb the outgoing waves without any reflection. First,

a case that a TE_z (transverse electric) wave impinges on a loss medium half space located at x<0 (region 1). The TE_z electric conductivity and magnetic loss are denoted as σ_1 and σ_1^*, and the permittivity and the permeability are represented as ε_1 and μ_1, respectively. Region 2 is defined as a lossless medium half space x>0. It is easy to demonstrate that, for any incidence angle, the reflection coefficient is always equal to zero when $\varepsilon_1 = \varepsilon_2$, $\mu_1 = \mu_2$, and $\dfrac{\sigma_1}{\varepsilon_1} = \dfrac{\sigma_1^*}{\mu_1}$ are satisfied. For the three-dimensional simulation, Berenger (1996) first split the six electromagnetic field Cartesian components into 12 subcomponents and rewrote Ampere's law and Faraday's law to the corresponding subcomponents forms. By analogy with the case of the TE_z wave, if the absorbing boundary conditions are set as shown in Fig. A.5, any outgoing waves from the inner vacuum can be absorbed without reflection. On the six sides of the PML boundary, the PML layers match the inner vacuum by having zero transverse electrical conductivities and magnetic losses. For the 12 edges of the PML, only one electrical conductivity and magnetic loss equal zero. At the eight corners, all conductivities and losses are not zero. In the PML layer, the permittivity and permeability equal the corresponding values in vacuum, and all conductivities and losses have to satisfy

$$\frac{\sigma}{\varepsilon_0} = \frac{\sigma^*}{\mu_0}.$$

Berenger (1996) introduced the split field PML based on a mathematical model. The medium at the boundary layer is hypothetical. In 1995, Sacks [82] used a uniaxial anisotropic medium (UPML) to model the perfectly matched layer. In this technique,

Maxwell's equations do not need to be rewritten to the split-field forms. and the numerical algorithm is simplified. Then, in 1999, Liu applied the UPML boundary to the PSTD method [65]. In this technique, the permittivity $\overline{\overline{\varepsilon}}$ and permeability $\overline{\overline{\mu}}$ of the uniaxial anisotropic medium, which are expressed to diagonal tensors, are given by:

$$\overline{\overline{\varepsilon}} = \varepsilon_0 \begin{bmatrix} \dfrac{s_y s_z}{s_x} & 0 & 0 \\ 0 & \dfrac{s_x s_z}{s_y} & 0 \\ 0 & 0 & \dfrac{s_x s_y}{s_z} \end{bmatrix}, \tag{2.40a}$$

$$\overline{\overline{\mu}} = \mu_0 \begin{bmatrix} \dfrac{s_y^* s_z^*}{s_x^*} & 0 & 0 \\ 0 & \dfrac{s_x^* s_z^*}{s_y^*} & 0 \\ 0 & 0 & \dfrac{s_x^* s_y^*}{s_z^*} \end{bmatrix}, \tag{2.40b}$$

where s and s^* are dimensionless values, given by:

$$s_x = 1 - \frac{\sigma_x}{j\omega\varepsilon_0}, \ s_y = 1 - \frac{\sigma_y}{j\omega\varepsilon_0}, \ s_z = 1 - \frac{\sigma_z}{j\omega\varepsilon_0}, \text{ and} \tag{2.41a}$$

$$s_x^* = 1 - \frac{\sigma_x^*}{j\omega\mu_0}, \ s_y^* = 1 - \frac{\sigma_y^*}{j\omega\mu_0}, \ s_z^* = 1 - \frac{\sigma_z^*}{j\omega\mu_0}. \tag{2.41b}$$

By analogy with the split field PML condition $\dfrac{\sigma}{\varepsilon_0} = \dfrac{\sigma^*}{\mu_0}$, the anisotropic medium, which

can absorb the outgoing waves without reflection, has to satisfy the following conditions:

$$s_x = s^*_x, \ s_y = s^*_y, \ s_z = s^*_z. \qquad\qquad (2.42)$$

In Eqs. $(2.41a)$ and $(2.41b)$, values of the electrical conductivities and the magnetic

losses depend upon the location in the UPML boundary. If we assume, for example, that

a boundary with the thickness d is along the x direction and the interface of the boundary

and the inner vacuum locates at the x=0, the value of the electric conductivity is given by:

$$\sigma_x(\eta) = -\left(\frac{x}{d}\right)^m \frac{(m+1)\ln(R(0))}{2\sqrt{\frac{\mu_0}{\varepsilon_0}}d}, \qquad\qquad (2.43)$$

where R(0) represents the desired reflection error of the UPML boundary, and m is a real

number which is usually chosen within 3<m<4. The corresponding values of the

magnetic losses can be obtained from the absorbing boundary conditions.

Similar to calculation in the computational domain, to simulate the wave

absorption of the UPML boundary, it is necessary to also discretize Maxwell's equations

in the time domain also. First, Eqs. $(2.40a)$ and $(2.40b)$ are substituted into Eqs. $(2.11a)$

and $(2.11b)$ to obtain expressions of Maxwell curl equations in the UPML boundary:

$$\nabla \times \vec{H} = -j\omega\varepsilon_0 \begin{bmatrix} \dfrac{s_y s_z}{s_x} & 0 & 0 \\ 0 & \dfrac{s_x s_z}{s_y} & 0 \\ 0 & 0 & \dfrac{s_x s_y}{s_z} \end{bmatrix} \vec{E}, \qquad (2.44a)$$

$$\nabla \times \vec{E} = j\omega\mu_0 \begin{bmatrix} \dfrac{s_y^* s_z^*}{s_x^*} & 0 & 0 \\ 0 & \dfrac{s_x^* s_z^*}{s_y^*} & 0 \\ 0 & 0 & \dfrac{s_x^* s_y^*}{s_z^*} \end{bmatrix} \vec{H}. \qquad (2.44b)$$

In order to make the numerical computation more efficient, two new vectors, $\vec{A}$ and $\vec{C}$, are defined. Their Cartesian components are represented as:

$$A_x = \frac{s_z}{s_x} E_x, \quad A_y = \frac{s_x}{s_y} E_y, \quad A_z = \frac{s_y}{s_z} E_z, \qquad (2.45a)$$

$$C_x = \frac{s_z^*}{s_x^*} H_x, \quad C_y = \frac{s_x^*}{s_y^*} H_y, \quad C_z = \frac{s_y^*}{s_z^*} H_z. \qquad (2.45b)$$

Applying Eqs. $(2.45a)$ and $(2.45b)$ to Eqs. $(2.44a)$ and $(2.44b)$ shows:

$$\nabla \times \vec{H} = \varepsilon_0 \frac{\partial \vec{A}}{\partial t} + \begin{bmatrix} \sigma_y & 0 & 0 \\ 0 & \sigma_z & 0 \\ 0 & 0 & \sigma_x \end{bmatrix} \vec{A}, \tag{2.46a}$$

$$\nabla \times \vec{E} = -\mu_0 \frac{\partial \vec{C}}{\partial t} - \begin{bmatrix} \sigma_y^* & 0 & 0 \\ 0 & \sigma_z^* & 0 \\ 0 & 0 & \sigma_x^* \end{bmatrix} \vec{C}. \tag{2.46b}$$

Multiplying a factor of $\exp(\frac{\sigma_y}{\varepsilon_0} \cdot t)$ and integrating on the temporal interval $[n\Delta t, (n+1)\Delta t]$, the x component of Eq. $(2.46a)$ at the grid point denoted by index (I, J, K) is written as follows:

$$\int_{n\Delta t}^{(n+1)\Delta t} \{\varepsilon_0 \frac{\partial [A_x(I,J,K)\exp(\frac{\sigma_y(I,J,K)}{\varepsilon_0}t)]}{\partial t}\}dt$$

$$= \int_{n\Delta t}^{(n+1)\Delta t} \{\frac{\partial H_z^s(I,J,K)}{\partial y} - \frac{\partial H_y^s(I,J,K)}{\partial z}\} \exp(\frac{\sigma_y(I,J,K)}{\varepsilon_0}t)dt. \tag{2.47}$$

By analogy with scheme 2, which is used to discretize the Maxwell's equations in the computational domain, the finite different analog of Eq. (2.47) is obtained as:

$$A_x^{(n+1)}(I,J,K)$$

$$= \exp(-\frac{\sigma_y(I,J,K)}{\varepsilon_0}\Delta t)A_x^{(n)}(I,J,K)$$

$$+ \exp(-\frac{\sigma_y(I,J,K)}{\varepsilon_0}\frac{\Delta t}{2})\Delta tc\sqrt{\frac{\mu_0}{\varepsilon_0}}\{\frac{\partial H_z^{s(n+\frac{1}{2})}(I,J,K)}{\partial y} - \frac{\partial H_y^{s(n+\frac{1}{2})}(I,J,K)}{\partial z}\}. \tag{2.48a}$$

The finite different analog of the y component and z component are given by:

$$A_y^{(n+1)}(I,J,K)$$

$$= \exp(-\frac{\sigma_z(I,J,K)}{\varepsilon_0}\Delta t)A_y^{(n)}(I,J,K)$$

$$+ \exp(-\frac{\sigma_z(I,J,K)}{\varepsilon_0}\frac{\Delta t}{2})\Delta tc\sqrt{\frac{\mu_0}{\varepsilon_0}}\{\frac{\partial H_x^{s(n+\frac{1}{2})}(I,J,K)}{\partial z} - \frac{\partial H_z^{s(n+\frac{1}{2})}(I,J,K)}{\partial x}\}, \qquad (2.48b)$$

$$A_z^{(n+1)}(I,J,K)$$

$$= \exp(-\frac{\sigma_x(I,J,K)}{\varepsilon_0}\Delta t)A_z^{(n)}(I,J,K)$$

$$+ \exp(-\frac{\sigma_x(I,J,K)}{\varepsilon_0}\frac{\Delta t}{2})\Delta tc\sqrt{\frac{\mu_0}{\varepsilon_0}}\{\frac{\partial H_y^{s(n+\frac{1}{2})}(I,J,K)}{\partial x} - \frac{\partial H_x^{s(n+\frac{1}{2})}(I,J,K)}{\partial y}\}, \qquad (2.48c)$$

Similar to Eq. ($2.46a$), the finite different analogs of Eq. ($2.46b$) are written for the Cartesian component as:

$$\sqrt{\frac{\mu_0}{\varepsilon_0}}C_x^{(n+\frac{1}{2})}(I,J,K)$$

$$= \exp(-\frac{\sigma_y^*(I,J,K)}{\mu_0}\Delta t)\sqrt{\frac{\mu_0}{\varepsilon_0}}C_x^{(n-\frac{1}{2})}(I,J,K)$$

$$- \exp(-\frac{\sigma_y^*(I,J,K)}{\mu_0}\frac{\Delta t}{2})\Delta tc\{\frac{\partial E_z^{s(n)}(I,J,K)}{\partial y} - \frac{\partial E_y^{s(n)}(I,J,K)}{\partial z}\}, \qquad (2.49a)$$

$$\sqrt{\frac{\mu_0}{\varepsilon_0}}C_y^{(n+\frac{1}{2})}(I,J,K)$$

$$= \exp(-\frac{\sigma_z^*(I,J,K)}{\mu_0}\Delta t)\sqrt{\frac{\mu_0}{\varepsilon_0}}C_y^{(n-\frac{1}{2})}(I,J,K)$$

$$-\exp(-\frac{\sigma_z^*(I,J,K)}{\mu_0}\frac{\Delta t}{2})\Delta tc\{\frac{\partial E_x^{s(n)}(I,J,K)}{\partial z}-\frac{\partial E_z^{s(n)}(I,J,K)}{\partial x}\}, \qquad (2.49b)$$

$$\sqrt{\frac{\mu_0}{\varepsilon_0}}C_z^{(n+\frac{1}{2})}(I,J,K)$$

$$= \exp(-\frac{\sigma_x^*(I,J,K)}{\mu_0}\Delta t)\sqrt{\frac{\mu_0}{\varepsilon_0}}C_z^{(n-\frac{1}{2})}(I,J,K)$$

$$-\exp(-\frac{\sigma_x^*(I,J,K)}{\mu_0}\frac{\Delta t}{2})\Delta tc\{\frac{\partial E_y^{s(n)}(I,J,K)}{\partial x}-\frac{\partial E_x^{s(n)}(I,J,K)}{\partial y}\}. \qquad (2.49c)$$

Furthermore, it is also necessary to discretize the Eqs. $(2.45a)$ and $(2.45b)$ in the time domain. The x component of Eqs. $(2.45a)$ is chosen as an example. Consider the integral of the product of the x component and $\exp(\frac{\sigma_x}{\varepsilon_0}\cdot t+\frac{\sigma_z}{\varepsilon_0}\cdot t)$ on temporal interval $[n\Delta t,(n+1)\Delta t]$:

$$\int_{n\Delta t}^{(n+1)\Delta t}\exp(\frac{\sigma_z(I,J,K)}{\varepsilon_0}\cdot t)\frac{\partial}{\partial t}(A_x(I,J,K)\exp(\frac{\sigma_x(I,J,K)}{\varepsilon_0}\cdot t))dt$$

$$=\int_{n\Delta t}^{(n+1)\Delta t}\exp(\frac{\sigma_x(I,J,K)}{\varepsilon_0}\cdot t)\frac{\partial}{\partial t}(E_x^s(I,J,K)\exp(\frac{\sigma_z(I,J,K)}{\varepsilon_0}\cdot t))dt, \qquad (2.50)$$

The integrals in Eq. (2.50) are approximated as follows:

$$\int_{n\Delta t}^{(n+1)\Delta t} \exp(\frac{\sigma_z(I,J,K)}{\varepsilon_0} \cdot t)\frac{\partial}{\partial t}(A_x(I,J,K)\exp(\frac{\sigma_x(I,J,K)}{\varepsilon_0} \cdot t))dt$$

$$= \exp(\frac{\sigma_z(I,J,K)}{\varepsilon_0} \cdot (n+\frac{1}{2})\Delta t)\{A_x^{n+1}(I,J,K)\exp(\frac{\sigma_x(I,J,K)}{\varepsilon_0} \cdot (n+1)\Delta t)$$

$$- A_x^n(I,J,K)\exp(\frac{\sigma_x(I,J,K)}{\varepsilon_0} \cdot n\Delta t)\}, \tag{2.51a}$$

$$\int_{n\Delta t}^{(n+1)\Delta t} \exp(\frac{\sigma_x(I,J,K)}{\varepsilon_0} \cdot t)\frac{\partial}{\partial t}(E_x^s(I,J,K)\exp(\frac{\sigma_z(I,J,K)}{\varepsilon_0} \cdot t))dt$$

$$= \exp(\frac{\sigma_x(I,J,K)}{\varepsilon_0} \cdot (n+\frac{1}{2})\Delta t)\{E_x^{s(n+1)}(I,J,K)\exp(\frac{\sigma_z(I,J,K)}{\varepsilon_0} \cdot (n+1)\Delta t)$$

$$- E_x^{s(n)}(I,J,K)\exp(\frac{\sigma_z(I,J,K)}{\varepsilon_0} \cdot n\Delta t)\}. \tag{2.51b}$$

After applying Eqs. ($2.51a$) and ($2.51b$), the finite different analog of the x component of ($2.45a$) is given as:

$$E_x^{s(n+1)}(I,J,K)$$

$$= \exp(-\frac{\sigma_z(I,J,K)}{\varepsilon_0}\Delta t)E_x^{s(n)}(I,J,K)$$

$$+ \exp(-\frac{\sigma_x(I,J,K)+\sigma_z(I,J,K)}{\varepsilon_0}\frac{\Delta t}{2})\{-A_x^{(n)}(I,J,K)$$

$$+ \exp(\frac{\sigma_x(I,J,K)}{\varepsilon_0}\Delta t)A_x^{(n+1)}(I,J,K)\}. \tag{2.52a}$$

By analogy with ($2.52a$), the other finite different analogs of Eqs. ($2.45a$) and ($2.45b$) can be obtained as follows:

$$E_y^{s(n+1)}(I,J,K)$$

$$= \exp(-\frac{\sigma_x(I,J,K)}{\varepsilon_0}\Delta t)E_y^{s(n)}(I,J,K)$$

$$+ \exp(-\frac{\sigma_y(I,J,K)+\sigma_x(I,J,K)}{\varepsilon_0}\frac{\Delta t}{2})\{-A_y^{(n)}(I,J,K)$$

$$+ \exp(\frac{\sigma_y(I,J,K)}{\varepsilon_0}\Delta t)A_y^{(n+1)}(I,J,K)\}, \qquad\qquad (2.52b)$$

$$E_z^{s(n+1)}(I,J,K)$$

$$= \exp(-\frac{\sigma_y(I,J,K)}{\varepsilon_0}\Delta t)E_z^{s(n)}(I,J,K)$$

$$+ \exp(-\frac{\sigma_z(I,J,K)+\sigma_y(I,J,K)}{\varepsilon_0}\frac{\Delta t}{2})\{-A_z^{(n)}(I,J,K)$$

$$+ \exp(\frac{\sigma_z(I,J,K)}{\varepsilon_0}\Delta t)A_z^{(n+1)}(I,J,K)\}, \qquad\qquad (2.52c)$$

And

$$H_x^{s(n+\frac{1}{2})}(I,J,K)$$

$$= \exp(-\frac{\sigma_z^*(I,J,K)}{\mu_0}\Delta t)H_x^{s(n-\frac{1}{2})}(I,J,K)$$

$$+ \exp(-\frac{\sigma_x^*(I,J,K)+\sigma_z^*(I,J,K)}{\mu_0}\frac{\Delta t}{2})\{-C_x^{(n-\frac{1}{2})}(I,J,K)$$

$$+ \exp(\frac{\sigma_x^*(I,J,K)}{\mu_0}\Delta t)C_x^{(n+\frac{1}{2})}(I,J,K)\}, \qquad\qquad (2.53a)$$

$$H_y^{s(n+\frac{1}{2})}(I,J,K)$$

$$= \exp(-\frac{\sigma_x^*(I,J,K)}{\mu_0}\Delta t)H_y^{s(n-\frac{1}{2})}(I,J,K)$$

$$+ \exp(-\frac{\sigma_y^*(I,J,K)+\sigma_x^*(I,J,K)}{\mu_0}\frac{\Delta t}{2})\{-C_y^{(n-\frac{1}{2})}(I,J,K)$$

$$+ \exp(\frac{\sigma_y^*(I,J,K)}{\mu_0}\Delta t)C_y^{(n+\frac{1}{2})}(I,J,K)\}, \qquad (2.53b)$$

$$H_z^{s(n+\frac{1}{2})}(I,J,K)$$

$$= \exp(-\frac{\sigma_y^*(I,J,K)}{\mu_0}\Delta t)H_z^{s(n-\frac{1}{2})}(I,J,K)$$

$$+ \exp(-\frac{\sigma_z^*(I,J,K)+\sigma_y^*(I,J,K)}{\mu_0}\frac{\Delta t}{2})\{-C_z^{(n-\frac{1}{2})}(I,J,K)$$

$$+ \exp(\frac{\sigma_z^*(I,J,K)}{\mu_0}\Delta t)C_z^{(n+\frac{1}{2})}(I,J,K)\}. \qquad (2.53c)$$

2.6 The transformation of near field to far field

Following the preceding discussions, the frequency-dependent scattered waves in near field can be obtained. However, in order to obtain the single-scattering properties, for example, amplitude scattering matrix and phase matrix, the frequency-dependent near-field solution must to be transformed to far field. According to the electromagnetic equivalence principle, two approaches, surface integration technique and volume integration, can be applied to the transformation of near field to far field [19]. Because the volume integration approach is less accurate for the large refractive index and has a relatively tedious computation, the surface integration approach was chosen for this study.

Before discussing the transformation of near field to far field, this study reviews the definitions of two important scattering properties, amplitude scattering matrix and phase matrix, which describe the relation between the incident wave and the scattered wave. As shown in Fig. A.6, it is assumed that the incident wave propagates along z direction, and the incident electric field is decomposed into two components orthogonal to each other. The principal-scattering plane, which includes both the incident direction and the scattering direction, is chosen as a reference plane for the decomposition. In this plane, the horizontal component is $E_{//}^i$ and the component perpendicular to the principal scattering plane is vertical component $E_{\perp}^i$. Similarly to the incident wave, the scattered wave can be projected to the two components ($E_{//}^s$ and $E_{\perp}^s$) also. Because the electromagnetic boundary condition is linear on the scatter surface, the relation between the incident and the scattered waves can be given by:

$$
\begin{pmatrix} E_{//}^{\,s}(\bar{r}) \\ E_{\perp}^{\,s}(\bar{r}) \end{pmatrix} = \frac{\exp(jkr)}{-jkr} \begin{pmatrix} S_2 & S_3 \\ S_4 & S_1 \end{pmatrix} \begin{pmatrix} E_{//}^{\,i} \\ E_{\perp}^{\,i} \end{pmatrix},
\tag{2.54}
$$

where the vector $\bar{r}$ specifies the scattering direction, r is the distance from the scatter to the scattering observation point, k is the wave number and the S matrix is the amplitude scattering matrix. In light scattering, another important scattering property is the phase matrix, which describes the relation of the incident and scattered Stokes parameters. The Stokes parameters are defined as the follows:

$$I = E_{//}E_{//}^{*} + E_{\perp}E_{\perp}^{*}, \qquad (2.55a)$$

$$Q = E_{//}E_{//}^{*} - E_{\perp}E_{\perp}^{*}, \qquad (2.55b)$$

$$U = E_{//}E_{\perp}^{*} + E_{//}E_{\perp}^{*}, \qquad (2.55c)$$

$$V = j(E_{//}E_{\perp}^{*} - E_{//}E_{\perp}^{*}), \qquad (2.55d)$$

where the superscript asterisk denotes the corresponding conjugate complex and j is imaginary unit. I represents field intensity and Q, U, and V have the same dimension, and are used to describe the light polarization. In terms of the Stokes parameters, the phase matrix is defined by the following equation:

$$\begin{pmatrix} I^s \\ Q^s \\ U^s \\ V^s \end{pmatrix} = \frac{1}{k^2 r^2} \begin{pmatrix} P_{11} & P_{12} & P_{13} & P_{14} \\ P_{21} & P_{22} & P_{23} & P_{24} \\ P_{31} & P_{32} & P_{33} & P_{34} \\ P_{35} & P_{36} & P_{37} & P_{38} \end{pmatrix} \begin{pmatrix} I^i \\ Q^i \\ U^i \\ V^i \end{pmatrix}, \qquad (2.56)$$

where superscript s and i denote the scattered and incident light, respectively. According to the definition of the amplitude scattering matrix, the elements of the phase are shown as the following equations:

$$P_{11} = \frac{1}{2}(s_1 s_1^* + s_2 s_2^* + s_3 s_3^* + s_4 s_4^*), \qquad (2.57a)$$

$$P_{12} = \frac{1}{2}(-s_1 s_1^* + s_2 s_2^* - s_3 s_3^* + s_4 s_4^*), \qquad (2.57b)$$

$$P_{13} = \text{Re}(s_1 s_4^* + s_2 s_3^*), \qquad\qquad\qquad (2.57c)$$

$$P_{14} = \text{Im}(-s_1 s_4^* + s_2 s_3^*), \qquad\qquad\qquad (2.57d)$$

$$P_{21} = \frac{1}{2}(-s_1 s_1^* + s_2 s_2^* + s_3 s_3^* - s_4 s_4^*), \qquad\qquad (2.57e)$$

$$P_{22} = \frac{1}{2}(s_1 s_1^* + s_2 s_2^* - s_3 s_3^* - s_4 s_4^*), \qquad\qquad (2.57f)$$

$$P_{23} = \text{Re}(-s_1 s_4^* + s_2 s_3^*), \qquad\qquad\qquad (2.57g)$$

$$P_{24} = \text{Im}(s_1 s_4^* + s_2 s_3^*), \qquad\qquad\qquad (2.57h)$$

$$P_{31} = \text{Re}(s_1 s_3^* + s_2 s_4^*), \qquad\qquad\qquad (2.57i)$$

$$P_{32} = \text{Re}(-s_1 s_3^* + s_2 s_4^*), \qquad\qquad\qquad (2.57j)$$

$$P_{33} = \text{Re}(s_1 s_2^* + s_3 s_4^*), \qquad\qquad\qquad (2.57k)$$

$$P_{34} = \text{Im}(s_1^* s_2 + s_3^* s_4), \qquad\qquad\qquad (2.57l)$$

$$P_{41} = \text{Im}(s_1 s_3^* + s_2^* s_4), \qquad\qquad\qquad (2.57m)$$

$$P_{42} = \text{Im}(-s_1 s_3^* + s_2^* s_4), \qquad\qquad\qquad (2.57n)$$

$$P_{43} = \text{Im}(s_1 s_2^* - s_3 s_4^*), \qquad\qquad\qquad (2.57o)$$

$$P_{44} = \text{Re}(s_1 s_2^* - s_3 s_4^*). \qquad\qquad\qquad (2.57p)$$

Now the surface integration technique will be recapitulated. According to the electromagnetic equivalence theorem, the equivalent electric and magnetic currents on a surface including a scatter, can be used to substitute the scatter to create the same far fields. The equivalence is given by the following equtions:

$$\vec{J} = \hat{n}_s \times \vec{H}^s, \qquad\qquad\qquad (2.58a)$$

$$\vec{M} = \vec{E}^s \times \hat{n}_s, \qquad\qquad\qquad (2.58b)$$

where $\hat{n}_s$ is the unit normal vector of the surface. The Hertz vectors associated with the equivalent currents can be obtained by:

$$\vec{\Pi}_e(\vec{r}) = \oiint_\Sigma G(\vec{r}',\vec{r})\vec{J}d^2r', \qquad\qquad\qquad (2.59a)$$

$$\vec{\Pi}_m(\vec{r}) = \oiint_\Sigma G(\vec{r}',\vec{r})\vec{M}d^2r', \qquad\qquad\qquad (2.59b)$$

where Σ is the surface which encloses the scatter and the free space Green's function $G(\vec{r}',\vec{r})$ is given by:

$$G(\vec{r}',\vec{r}) = \frac{\exp(jk|\vec{r}'-\vec{r}|)}{4\pi|\vec{r}'-\vec{r}|}, \qquad\qquad\qquad (2.60)$$

The electric field induced by the equivalent currents on the surface can be obtained by:

$$\vec{E}^s(\vec{r}) = \frac{j}{k}\nabla \times \nabla \times \vec{\Pi}_e(\vec{r}) - \nabla \times \vec{\Pi}_m(\vec{r}), \qquad\qquad\qquad (2.61)$$

Substituting Eqs. ($2.59a$) and ($2.59b$) into Eq. (2.61) and letting r approach infinity

gives the scattered field in far field region as:

$$\bar{E}^s(\hat{n}) = \frac{\exp(-jkr)}{-jr}\frac{k}{4\pi}\hat{n}\times$$
$$\oiint_\Sigma \{\hat{n}_s \times \bar{E}(\bar{r}') - \hat{n}\times[\hat{n}_s \times \bar{H}(\bar{r}')]\}\exp(-jk\hat{n}\cdot\bar{r}')d^2r', \qquad (2.62)$$

where $\hat{n}$ represents the unit vector in the scattering direction. Thus, $\hat{\alpha}$ and $\hat{\beta}$ are used to

denote the unit vectors which are horizontal and perpendicular to the principal scattering

plane, respectively, and satisfy:

$$\hat{n} = \hat{\beta}\times\hat{\alpha}, \qquad (2.63)$$

Therefore, the scattered electric field can be represented as the horizontal and

perpendicular components in the form:

$$\bar{E}^s(\hat{n}) = E_\perp^s(\hat{n})\hat{\beta} + E_{//}^s(\hat{n})\hat{\alpha}, \qquad (2.64)$$

Rewriting Eq. (2.62) in the components form gives:

$$\begin{pmatrix} E_{//}^s(\hat{n}) \\ E_\perp^s(\hat{n}) \end{pmatrix} = \frac{\exp(-jkr)}{-jr}\frac{k}{4\pi}\oiint_\Sigma \begin{pmatrix} \hat{\alpha}\cdot\bar{\bar{\Im}} \\ \hat{\beta}\cdot\bar{\bar{\Im}} \end{pmatrix}\exp(-jk\hat{n}\cdot\bar{r}')d^2r', \qquad (2.65)$$

where $\bar{\bar{\Im}}$ denotes the vector, $\hat{n} \times \hat{n}_s \times \vec{E}(\vec{r}') - \hat{n} \times \hat{n} \times [\hat{n}_s \times \vec{H}(\vec{r}')]$. Assuming the incident direction is along z direction, the horizontal and the perpendicular components of the incident electric field are:

$$\begin{pmatrix} E_{//}^i \\ E_{\perp}^i \end{pmatrix} = \begin{pmatrix} \hat{\beta} \cdot \hat{x} & \hat{\beta} \cdot \hat{y} \\ -\hat{\beta} \cdot \hat{y} & \hat{\beta} \cdot \hat{x} \end{pmatrix} \begin{pmatrix} E_x^i \\ E_y^i \end{pmatrix},$$

(2.66)

where E_x^i and E_y^i indicate the incident electric field components in a Cartesian coordinate. On the basis of the Eqs. (2.54) and (2.66), the Eq. (2.65) is rewritten as:

$$\begin{aligned}
\begin{pmatrix} E_{//}^s(\hat{n}) \\ E_{\perp}^s(\hat{n}) \end{pmatrix} &= \frac{\exp(-jkr)}{-jkr} \begin{pmatrix} S_2 & S_3 \\ S_4 & S_1 \end{pmatrix} \begin{pmatrix} E_{//}^i \\ E_{\perp}^i \end{pmatrix} \\
&= \frac{\exp(-jkr)}{-jkr} \begin{pmatrix} F_{\alpha,y} & F_{\alpha,x} \\ F_{\beta,y} & F_{\beta,x} \end{pmatrix} \begin{pmatrix} \hat{\beta} \cdot \hat{x} & \hat{\beta} \cdot \hat{y} \\ -\hat{\beta} \cdot \hat{y} & \hat{\beta} \cdot \hat{x} \end{pmatrix} \begin{pmatrix} E_x^i \\ E_y^i \end{pmatrix},
\end{aligned}$$

(2.67)

where

$$\begin{pmatrix} F_{\alpha,y} \\ F_{\beta,y} \end{pmatrix} = \frac{k^2}{4\pi} \iint_{\Sigma} \exp(-ik\hat{n} \cdot \vec{r}') \begin{pmatrix} \hat{\alpha} \cdot \bar{\bar{\Im}} \\ \hat{\beta} \cdot \bar{\bar{\Im}} \end{pmatrix} d^2 r' \Big|_{E_x^i=0,E_y^i=1},$$

(2.68a)

$$\begin{pmatrix} F_{\alpha,x} \\ F_{\beta,x} \end{pmatrix} = \frac{k^2}{4\pi} \iint_{\Sigma} \exp(-ik\hat{n} \cdot \vec{r}') \begin{pmatrix} \hat{\alpha} \cdot \bar{\bar{\Im}} \\ \hat{\beta} \cdot \bar{\bar{\Im}} \end{pmatrix} d^2 r' \Big|_{E_x^i=1,E_y^i=0},$$

(2.68b)

where the subscripts ($E_x^i = 0, E_y^i = 1$) and ($E_x^i = 1, E_y^i = 0$) denote that the polarization

of the incident electric field is along the x direction and y direction, respectively.

Therefore, following the preceding discussion, the amplitude scattering matrix can be

obtained from the near fields. Using Eqs. ($2.57a$) - ($2.57o$), the phase matrix could be

calculated from the corresponding amplitude matrix.

CHAPTER III

VALIDATION OF PSEUDO-SPECTRAL TIME-DOMAIN

METHOD IN 3-D SPACE FOR LIGHT SCATTERING BY

ATMOSPHERIC PARTICLES

3.1 Introduction

Following the preceding discussion in Chapter II, a 3-D PSTD code in FORTRAN has been developed for scattering of light by arbitrary geometries. Before applying the PSTD code to atmospheric particles, this chapter discusses the applicability of the PSTD method for scattering of light. The PSTD method is first compared with the Lorenz-Mei theory. As discussed in Chapter I, scattering of light from homogeneous spheres can be precisely described by the conventional Lorenz-Mie theory (Mie theory). In this method, an analytical solution can be obtained by directly solving Maxwell's equation in the frequency domain. Therefore, the accuracy of the PSTD method for homogeneous spheres can be studied by comparison with the corresponding solution from the Lorenz-Mie theory. Furthermore, the PSTD method is compared with the T-matrix method, which is an efficient technique applied to scattering of light from rotationally symmetric particles with moderate size parameters. The solutions from this method are also analytical. Thus, the applicability of the PSTD method for light scattering of nonspherical particles can be investigated by comparison with the counterpart of the T-matrix method.

This chapter is organized as follows. As discussed in Chapter II, five different schemes are applied to discretizing Maxwell's equations in the time domain. In the second section of this chapter, the five schemes are used to carry out the phase functions for spheres. The accuracy of the schemes is investigated by comparison with the counterpart from the Mie theory. In the third section, the PSTD method is utilized to study the scattering properties of spheres with different size parameters and refractive indices. The accuracy of the PSTD method for spheres is investigated by comparison with the Mie theory. The impact of the grid spatial resolution and size parameter on the simulation accuracy are also studied in this section. In the fourth section, two geometries, circular cylinders and spheroids, are considered. The applicability of the PSTD method for oriented nonspherical particles is validated by comparison with the corresponding T-matrix solutions in terms of scattering phase functions. The fifth section draws a conclusion.

3.2 Investigation of the accuracy of the five methods used for discretizing Maxwell's equations in the PSTD method

As discussed in Chapter II, there are five different methods involved in discretization of Maxwell's equations in the time domain. To investigate the accuracy of the five methods, scattering phase functions of spheres calculated from the PSTD method based on the five discretization methods are compared with the corresponding results from Mie theory. First, the phase function of a sphere with a size parameter of 20 is calculated by the PSTD method. In this simulation, the grid spatial resolution, which is

defined as the ratio of the incident light wavelength in vacuum to the grid cell length, is

10, and the refractive index is 1.2+0.01j, where the imaginary part represents the

absorption of this medium. The phase functions from PSTD method and Mie theory are

compared in Fig. A.7 The relative errors, which are defined as the ratio of the difference

between the two solutions to the corresponding Mie results, are also given in this figure.

As shown in panel (a) of Fig. A.7, the solutions from the computations based on

discretization schemes 1, 2, and 3 are essentially the same, and in the relative error

patterns of the three schemes, no distinguishable difference is observed. The comparison

of the PSTD and Mie solutions shows considerable agreement except for some

deviations near scattering angle 90° and near the backward scattering direction. As

shown in panel (b) of Fig. A.7, the PSTD solutions based on Schemes 4 and 5 converge

with the Mie results at all scattering angles. In the relative error pattern of Panel (b), the

two discretization methods do not show any distinguishable difference, although the

PSTD solutions deviate from the Mie results at scattering angles near 90° and 180° In

Panel (c) of Fig. A.7, the absolute values of the relative errors of Schemes 2 and 5 are

plotted in a logarithmic scale. The differences of the two schemes can also be ignored.

Therefore, in the case of size parameter 20, the accuracies of the five methods are almost

indistinguishable.

Normally, in numerical simulations, errors can accumulate with simulation scale

and time steps. For example, the dispersion error of the FDTD method increases with

time steps. To compare the accuracy of the five methods for large size scale simulation,

phase function of a sphere with size parameter 50 is calculated by the PSTD method and

Mie theory, respectively. In this case, the refractive index is 1.1+0j. According to the discussion in Chapter II, for a nonabsorptive medium, discretization Schemes 1 through 5 are reduced to two schemes. For discussion in this chapter, Scheme A denotes the scheme originated from Schemes 1 through –3, and Scheme B is derived from Schemes 4 and 5. In Fig. A.8, the phase functions from Schemes A and B and the Mie theory are compared, and absolute values of the relative errors are plotted on a logarithmic scale. It is evident that the solutions of the PSTD associated with methods A and B essentially converge to the counterpart of Mie theory. The difference between the methods A and B cannot be distinguished from the patterns of relative error in logarithmic scale. Therefore, the five discretization methods provide the same accuracy for the light scattering study.

3.3 Validation of the PSTD method for sphere: comparison with the Mie theory

In this section, applicability of the PSTD method for spheres is investigated in comparison with Mie theory. Impacts of grid spatial resolution, size parameter, and refractive index on accuracy of the PSTD method are studied, where the grid spatial resolution is defined as the ratio of the incident light wavelength in vacuum to the length of the grid cell, the size parameter of sphere is the product of wave number of the incident light in vacuum and the sphere radius, and the refractive index is complex.

First, we consider the impact of grid spatial resolution. For the FDTD method, in which the spatial derivatives are approximated by the finite difference method, the accuracy of the simulation highly depends on the grid spatial resolution. Although a better solution can be obtained by increasing the spatial resolution, the much more

tedious computation associated with resolution increase makes the simulation very inefficient and even impractical. According to the numerical experiments, in the FDTD method for scattering of light, the grid spatial resolution is selected as the product of 25 and the real part of the refractive index for an acceptable accuracy. In the PSTD method, in which the spectral method is applied to the spatial derivatives in Maxwell's equations, the finer spatial resolution may also provide more accurate results. In order to discover the most efficient grid spatial resolution for an acceptable accuracy, phase functions from the PSTD method with spatial resolutions 8, 12, 16, and 20 are compared with their counterparts of Mie theory.

Figure A.9 compares the PSTD and Mie solutions at refractive index 1.05+0j and size parameter 20. In Panel (a) of this figure, a spatial resolution of 8. It is evident that the PSTD results follow the counterpart of Mie theory well at all scattering angles, although some differences are observed at scattering angles near 120°, 150°, and in a backward direction. The phase function at the spatial resolution 12 is shown in panel (b). There is a good agreement between the PSTD and Mie solutions for all scattering angles. In contrast to the results in panel (a), obvious differences are no longer observed at angles near 120°, and the difference near 150° is smaller in Panel (b). The results from the PSTD method at spatial resolutions 16 and 20 are compared with the counterparts of Mie theory in panels (c) and (d), respectively. For these two cases, the PSTD and Mie solutions are almost essentially the same except for slight deviations near the backward scattering direction. Therefore, the accuracy of the PSTD method increases with the grid spatial resolution. However, at resolution 16, the agreement of the phase functions near

the backward scattering direction is even less than with the counterparts at resolution 12. The implication is that an increase in resolution does not always provide better results.

Inside the scattering particles, the light wavelength is shorter than the wavelength in the vacuum due to the larger refractive index of the medium. Thus, keeping the length of the grid cell fixed, the ratio of the incident light wavelength in the scattering particle to the length of grid cell decreases with an increase in the refractive index. Therefore, in the FDTD method, to obtain the same accuracy, the spatial resolution needs to increase with the refractive index. In order to study the impact of refractive index on the PSTD method, phase functions are also calculated at refractive index 1.2+0j. Fig. A.10 shows the comparison of the Mie and PSTD results at size parameter 20. In panels (a), (b), (c), and (d), grid spatial resolutions are chosen as 8, 12, 16, and 20, respectively. As shown in panel (a), the PSTD solutions agree with the Mie solution at all scattering angles with some slight differences at the angles near 90° and in the backward direction. In contrast to the corresponding results at refractive index 1.05+0j, the agreement of the solutions in panel (a) does not worsen with the increase of the refractive index. The agreement of the comparison in panel (b) is better than its counterpart in panel (a) due to the increase of spatial resolution. The deviations near 90° and the backward direction obviously became smaller. The solution in panel (c) is almost the same as the result in panel (b) except for a slight decrease in the deviation near the backward direction. As shown in panel (d), the PSTD results at resolution 20 essentially converge with the Mie results at all scattering angles except for very slight differences at the backward direction.

According to the preceding discussion, it is evident that accuracy of the PSTD

method will increase with the spatial resolution, although in some special cases, agreement of the phase functions with the finer spatial resolution can be less pronounced at some scattering angles. On the basis of numerical experiments, the grid spatial resolution in the PSTD method can be determined as 10 multiplied by the largest real part of the refractive index in the computational domain for size parameters smaller than 20. Comparison of the solutions in Figs. A.9 and A.10 shows that the accuracy of the PSTD method is not as sensitive to the refractive index of the scattering particle as the FDTD method.

Secondly, the impact of the size parameter on the PSTD method is studied. In numerical simulation in the time domain, some errors increase with the calculation scale and time steps. This means that some simulation errors may increase with size parameter. For example, as discussed by Taflove [83], the dispersion errors of the FDTD method accumulate with the time steps. The accuracy of the FDTD method decreases with an increase in the scale of the computational domain. Additionally, in the FDTD method for scattering of light, obvious errors are frequently observed at the scattering angles near the backward direction in terms of phase function at large size parameters. In the PSTD method, almost no dispersion errors which accumulate with time steps are observed due to the application of the spectral method to the approximation of the spatial derivatives of the electromagnetic fields. However, in numerical simulations, calculation errors which increase with the computational scale and time steps cannot be entirely avoided. In addition, in the PSTD code, the phase differences of the scattered field and the incident field may increase with the size parameters and time steps because the analytic

incident field is introduced in the simulation. Therefore, the accuracy of the PSTD method at large size parameter needs to be investigated.

Figure A.11 shows the comparisons of the PSTD and Mie results in terms of phase functions at refractive index 1.05+0j. Two size parameters, 30 and 50, are involved in this study. According to the preceding discussion, the grid spatial resolution of the PSTD method is selected as 10. As shown in the left panel, the PSTD phase function is essentially the same as the counterpart of Mie theory at size parameter 30 except for a slight difference at the angles near 160°. The solutions at size parameter 50 are compared in the right panel. The PSTD and Mie results are essentially the same except for a very slight difference near 90°. It is evident that the accuracy of the PSTD method does not diminish with the increase of the size parameter. Especially at size parameter 50, no obvious difference is observed at the backward direction, whereas the FDTD method frequently creates obvious errors as the size parameter increases.

The phase functions of the PSTD method at refractive index 1.6+0j are compared with the counterpart of the Mie theory in Fig. A.12. The grid spatial resolution is selected as 16. As shown in the left panel of this figure, the PSTD solutions converge with the corresponding Mie results at most of the scattering angles. Some differences are observed at some scattering angles where the maxima or minima of the phase functions occur. The phase functions of the PSTD method also deviate slightly from the counterpart of Mie theory at the scattering angles near 180°. As shown in the right panel where the size parameter is 50, the solutions of the PSTD and Mie agree well at most of the scattering angles. The simulation errors of the PSTD method frequently occur at

some angles where the phase functions have slight oscillations and backward direction. In contrast to the comparison in the left panel, the accuracy of phase functions at size parameter 50 does not become worse, but rather is better at some scattering angles, for example the backward direction.

According to the discussions about Figs. A.11 and A.12, it is evident that the accuracy of the PSTD solution for the same spatial resolution does not degrade with the size parameter increase. In some cases, the agreement of the comparisons of the PSTD and Mie at the larger size parameters is even better. The reason for this phenomenon of the larger size simulation having better accuracy is discussed first by review of the discussion in Chapter II. Using the PSTD method, the discrete Fourier transform (DFT) is used in the spectral method, which approximates the spatial derivatives in Maxwell's equation. The accuracy of the derivative approximation can increase with the number of grid points involved in DFT. The accuracy of the simulation at the large size parameter, therefore, is improved because the computational domain includes more grid points. To demonstrate this assumption, the phase functions of a sphere with size parameter 80 are calculated from the PSTD method at refractive index 1.05+0j. In this case, a spatial resolution of 8 is selected. The results are compared with the corresponding Mie solutions in Fig. A.13. As shown in this figure, the PSTD results essentially converge with the counterparts of Mie theory and show almost no distinguishable difference. The accuracy of the phase functions at size parameter 80 is better than the counterparts at size parameters 30 or 50 and spatial resolution 10 which are shown in Fig. A.11. Furthermore, the agreement of this comparison is much better than the case at size

parameter 20 and resolution 8, which is shown in Fig. A.9. Therefore, the accuracy of the PSTD method does not degrade with the increase of the size parameter, and the applicability of the PSTD method for large size particles is validated.

As discussed in Chapter II, the accuracy of the PSTD method may be degraded due to Gibb's phenomenon caused by the discontinuities of the electromagnetic properties, such as refractive index, on the scattering particle surface. In the atmosphere, the real part of the refractive index of most of ice crystals and aerosols is smaller than 2. To study the impact of Gibb's phenomenon on the PSTD method for measurement of light scattering of the atmospheric particles, the phase functions of a sphere with size parameter 40 are calculated by both the PSTD method and Mie theory at refractive index 2.0+0j. In this case, the spatial resolution is 18. As shown in Fig. A.14, the PSTD solutions follow the corresponding Mie results well at most of the scattering angles, although some differences are observed at some angles where the phase functions achieve maxima or minima. Therefore, for most of the atmospheric particles, the PSTD method for the scattering of light can provide an acceptable accuracy, which does not degrade with the increase of the size parameter. According to numerous numerical experiments, the spatial resolution at large size simulation can be determined as follows. When size parameter is larger than 30 and the real part of refractive index is smaller than 1.5, spatial resolution can be selected to be about 12. When the real part of refractive index is larger than 1.5 and smaller than 2.0, spatial resolution is determined to be about 9 multiplied by the real part of the refractive index.

3.4 Validation of the PSTD method for nonspherical particles: comparison with T-matrix method.

The single-scattering properties of rotationally symmetric particles with fixed orientation have also been discussed by Mishchenko et al. [57] using the rigorous T-matrix method. Analytical results can be obtained from this method. In this section, the phase functions of oriented cylinders and spheroids are calculated from the PSTD method. The applicability of the PSTD method for nonspherical particles is investigated by comparison with the T-matrix method in terms of phase functions.

Two geometries, spheroid and circular cylinder, are considered in this study. A spheroid is defined in terms of its vertical radius (polar radius hl) and horizontal radius (equatorial radius ha). The aspect ratio for this spheroid is defined as hl/ha. A spheroid for which the aspect ratio is larger than 1 is called a prolate spheroid; otherwise, it is called an oblate spheroid. A circular cylinder is specified in terms of the radius of its cross section (r) and height (h). The aspect ratio for this particle is defined as h/r. The size parameters of the two geometries are defined as k (the wave number = $2\pi/\lambda$) multiplied by the largest dimension of the particles, where λ is the incident wavelength. Therefore, the size parameter of a prolate spheroid is k2hl and the size parameter of an oblate spheroid is k2ha. For a circular cylinder, when h is larger than 2r, size parameter is defined as kh; otherwise, size parameter is defined as k2r.

Normally, for oriented particles, four angles, θ_i, φ_i, θ_s, and φ_s, specify the incidence scattering configuration. As shown in the left panel of Fig. A.15, incident angle (θ_i) and azimuth angle (φ_i) define the incident direction in a laboratory

coordinate system. As shown in Fig. A.15, the orientations of spheroids and cylinders in the laboratory coordinate system are specified by choosing the z axis as the symmetry axis of the two geometries. This symmetry of the particle orientation leads to the simplification of the incidence scattering configuration in which only three angles, θ_i, θ_s, and φ_s, are used. For oriented scattering particles, their single-scattering properties depend on both the scattering angle (θ_s) and the azimuth angle (φ_s) of a scattering plane to which the scattering properties are referred. The principal scattering plane, a plane with $\varphi_s = 0$, contains the zenith and incident directions.

First, the PDTD and T-matrix methods are used to compute the phase functions of an oriented spheroid at refractive index (1.381, 3.9×10^{-9}), which is a typical refractive index of oceanic aerosols. In this section, the grid spatial resolution for the PSTD method is selected as 12. The solutions are compared for a scattering azimuth angle, φ_s, of $0°$, and two incident angles, $0°$ and $30°$.

Figure A.16 shows the comparisons for an oblate spheroid with aspect ratio 0.5 and size parameter 20. In the left panel, the PSTD solutions at incident angle $0°$ agree well with the corresponding T-matrix results at all scattering directions, except for differences at some angles where the phase functions achieve maxima or minima and at the backward direction. In the right panel, the solutions from the PSTD and T-matrix methods at incident angle $30°$ are essentially the same. Only slight deviations are observed at the scattering angles near $170°$.

Figure A.17 is essentially the same as Fig. A.16 except for an aspect ratio of 2.

As shown in the left panel, at the incident angle 0°, the solutions of the PSTD and T-matrix methods agree very well at all scattering directions. Slight differences are observed at some scattering angles where the minima of phase function occur. In the right panel, the phase functions at the incident angle 30° change smoothly with the scattering angles, and the PSTD solutions essentially converge with the corresponding T-matrix results.

To investigate the impact of the size parameter on the PSTD method, the phase functions of a spheroid with aspect ratio of 2 and size parameter 50 are compared in Fig. A.18. As shown in the left panel, at the incident angle 0°, the PSTD solutions are essentially the same as the T-matrix results, except for slight differences near the scattering angle 160°. The agreement of the solutions at size parameter 50 is even better than the results at size parameter 20, which is shown in the left panel of Fig. A.17. As shown in the right panel, the phase functions from PSTD method deviates from the counterpart of the T-matrix method at the scattering angles near 130° and 160°.

Secondly, the phase functions of a circular cylinder with fixed orientation are calculated from the PSTD and T-matrix methods. The solutions are also compared for a scattering azimuth angle, φ_s, of $0°$, and two incident angles, 160° and 30°. Figure A.19 shows the comparison of the PSTD and T-matrix solutions at aspect ratio 1 and size parameter 20. As shown in the left panel, at the incident angle $0°$, the phase functions from the PSTD method deviates from the counterpart of the T-matrix only at scattering angles $20°$ and $95°$. At incident angle $30°$, the solutions of the PSTD and T-matrix methods are essentially the same. Figure A.20 compares with Fig. A.19 except for a size

parameter of 50. In this case, for both of the incident angles, $0^{°}$ and $30^{°}$, the PSTD solutions agree with the T-matrix results very well except for the differences at the angles where the maxima or minima of the phase functions occurs.

Figures A.21 and. A.22 compare with Figs. A.19 and A.20, respectively, except an aspect ratio 4 is used for the computations in Figs. A.21 and A.22. In Fig. A.21, the PSTD solutions converge well to the corresponding T-matrix results except at some scattering angles where the phase functions achieve maxima or minima, particularly for the case in which the incident angle is 0°. The calculations for size parameter 50 are compared in Fig. A.22, where it is shown that the phase functions frequently oscillate with the scattering angles. The solutions of the two methods agree very well except for the differences at some angles where the maxima or minima of the phase functions occur.

In this section, the comparison of the PSTD and T-matrix solutions demonstrate the excellent applicability of the PSTD method for the nonspherical particles with moderate and large sizes. Although some differences are observed at some scattering angles where the phase functions achieve maxima or minima, the accuracy of the PSTD method for nonspherical particles does not degrade with the increase in the size parameter; particularly, no errors which increase with the size parameter are observed at the backward direction. Therefore, the solutions for randomly oriented particles may be more accurate because the impact of errors is weakened by the orientation average. In contrast to the solutions for sphere discussed in Section 3.3, the PSTD method for nonspherical particles with moderate size provides better accuracy.

3.5 Summary and conclusion

A 3-D PSTD code, in which the five discretization methods discussed in Chapter II are used, has been developed for light scattering. The comparison of the PSTD method and Mie theory in terms of phase functions for a sphere with size parameters 20 and 50 demonstrates that the five different discretization methods provide the same accuracy, for both absorption and nonabsorption. The applicability of the PSTD method for scattering of light by sphere is the validated by comparison with Mie theory at different refractive indexes and size parameters. According to the numerical experiments, the grid spatial resolution is determined as follows: For the cases of size parameters smaller than 30, the grid spatial resolution can be determined as 10 multiplied by the real part of the refractive index (m_r). Otherwise, if m_r is smaller than 1.5, the resolutions is selected as 12, and if m_r is larger than 1.5 and smaller than 2.0, the spatial resolution is determined as 9 multiplied by m_r. In comparison with the Mie theory, some differences are observed at the scattering angles where the maxima or minima of the phase function occur as the solutions frequently oscillate. However, no obvious errors which accumulate with the increase of the scale of the computational domain or the time steps occur in the PSTD method; particularly, no errors accumulate with size parameter at the backward direction, whereas in the FDTD method, obvious errors frequently occur as the particle size increases. In some cases, the accuracy of the PSTD method increases with the size parameter because the approximation of the spatial derivatives obtained from the spectral method is more accurate due to more grid cells being involved in the simulation. Additionally, the agreement of the comparison of the PSTD and Mie solutions at

refractive index (2.0+0j) demonstrates that Gibb's phenomena caused by the discontinuities of the refractive index at the surface of the scattering particles does not create an obvious impact on the accuracy of the simulation in the case of m_r smaller than 2.0. Furthermore, the PSTD method is applied to the rotationally symmetric particles, spheroids and circular cylinders, and the solutions are compared with their counterparts of the T-matrix method at different incident angles and size parameters. The applicability of the PSTD method for nonspherical particles is validated by the excellent agreement of the comparisons. In contrast to the application to sphere, the solutions for nonspherical particles have the better accuracy.

CHAPTER IV

APPLICATION OF PSEUDO-SPECTRAL TIME-DOMAIN

METHOD TO LIGHT SCATTERING BY ICE CRYSTALS

4.1 Introduction

Cirrus clouds, which cover more than 20% of the globe, influence climate evolutions on all scales though their strong influences on the radiative budget of the terrestrial and atmospheric system. Significant research efforts have focused on the radiative properties of ice clouds from various perspectives [6–13]. Inasmuch as they are fundamental to the understanding of radiative properties, the scattering of light by ice particles is studied for various applications [14–26]. Additionally, remote sensing of cirrus clouds also requires a strong understanding of the single-scattering properties of ice crystals.

Laboratory experiments have demonstrated that the shape and size of ice particles are highly dependent on various factors, including temperature and supersaturation. According to observation of cirrus clouds [84], ice crystal morphologies include various geometries, for example, complex bullet rosettes and aggregates, although in the atmosphere, most ice crystals have a basic hexagonal structure. Various techniques are used to study the scattering of light by ice crystals due to the numerous geometries and size parameters of ice particles in cirrus clouds. The geometric-optic-integral-equation (GOM) method was used by Yang in 1996 [22] to investigate scattering properties of ice

crystals with size parameters larger than 60. The light scattering by small ice crystals with arbitrary shapes can be studied by the finite-different time domain method [17, 19]. For this method, the upper limit of size parameter is about 20. The T-matrix method is usually used for rotationally symmetric particles [57], although it may also be applied to quasi hexagonal prisms [18]. However, ice crystals with moderate size parameters and complex geometries cannot be characterized by all of these methods. In this study, the PSTD method is used to study the single-scattering properties of nonspherical ice crystals with small and moderate size parameters. In the PSTD method, a coarse spatial grid resolution is adequate for acceptable accuracy because of a high order approximation of spatial derivative based on the spectral method. In contrast to the FDTD method, in which the spatial resolution is about 25 to 30, the spatial resolution of the PSTD method is selected as approximately 12 when the real part of the refractive index is not too large. Therefore, in 3-D cases, the PSTD method is about 8 times more efficient than the conventional FDTD method. Additionally, when the refractive index of scattering particles is very close to one, the PSTD method provides much better accuracy than the FDTD method in which phase function has an obvious error at the scattering angles near the backward direction.

This chapter first compares the phase functions of the PSTD and FDTD methods with the corresponding Mie results at the refractive index of 1.05+0j. Furthermore, six ice crystal habits (hexagonal plate, hexagonal solid column, hexagonal hollow column, bullet rosette, aggregate, and droxtal) are defined in the PSTD method. The PSTD solutions of these ice crystals with fixed orientation are compared with the

corresponding FDTD results in term of phase function at size parameter 20 and wavelength 3.7 μm. Then, the phase functions of the ice crystals with size parameter 50 are also calculated by the PSTD method.

4.2 Application for ice crystals: comparison of the pseudo-spectral time-domain and finite-difference time-domain methods

4.2.1 Spheres with very small refractive index

The FDTD method has been widely used for various applications and demonstrated to be reliable in most electromagnetic simulations. However, for this method, when the variation of refractive index on particle surface is very tiny, an obvious error is observed in the phase functions near the backscattering direction. In this section, the phase function of a sphere with refractive index of 1.05+0j and size parameter of 20 is calculated from the PSTD, FDTD, and Mie methods. In the PSTD method, the spatial resolution is 8; in the FDTD method, the spatial resolution is 26. In Fig. A.23, the phase functions of PSTD and FDTD methods are compared with the corresponding results from Mie theory. As shown in this figure, the FDTD solutions are essentially the same as the Mie results, as the scattering angle is smaller than 160°. However, at scattering angles 160° to 180°, the phase function of the FDTD method substantially deviates from the corresponding counterpart of the Mie theory. In comparison of phase functions, the PSTD solutions agree very well with the Mie results at all scattering directions except for slight differences at the scattering angles 90°, 130°,

160°, and 180°. Therefore, in contrast to the FDTD method, which has an obvious error in terms of phase function at the backward scattering direction, the PSTD method provides an accurate solution with very coarse spatial resolution, as the particle refractive index is very close to one.

4.2.2 Hexagonal plates and columns

A hexagonal prism is the basic structure of ice crystals in cirrus clouds. As shown in the left panel of Fig. A.24, a hexagonal prism is specified in terms of its side length (a) and length (L). Its aspect ratio is defined as 2a/L. Thus, when aspect ratio is larger than one, this geometry is a hexagonal plate in which size parameter is defined as k (the wave number = $2\pi/\lambda$) multiplied by a; otherwise, this geometry becomes a hexagonal column with size parameter $\pi L/\lambda$. According to observed data from ice crystal clouds by Auer and Veal [85], Mitchell and Arnott [59] specified hexagonal columns by determining the crystal width D (D=2a) as follows:

$$D = \begin{cases} 0.7L^{1.0} & L < 100\mu m \\ 6.96L^{0.5} & L \geq 100\mu m \end{cases}, \tag{4.1}$$

where the units of width and length of the column are measured in microns. For hexagonal plates, the relation between particle width (D) and length (L) is presented by Pruppachar and Klett [86] as shown in Eq. (4.2):

v

$$L = 1.7916D^{0.474} \qquad 10\,\mu m \leq D \leq 3000\,\mu m, \tag{4.2}$$

where units selected are also microns. Therefore, when particle size is very small, the aspect ratio of the hexagonal prism is approximately equal to one.

As discussed in Chapter II, four angles, θ_i, φ_i, θ_s, and φ_s are used to specify the incidence scattering configuration, where incident angle (θ_i) and the azimuth angle (φ_i) define the incident direction and scattering angle (θ_s) and the corresponding azimuth angle (φ_s) define the scattering direction. The orientation of a hexagonal prism in a laboratory coordinate is shown in the right panel of Fig. A.24 in which the z axis is selected as the principal axis of this particle.

Phase functions of a hexagonal ice plate with size parameter 20 are calculated from the PSTD and FDTD methods at $\theta_i = 45°$, $\varphi_i = 0°$ and incident wavelength of 3.7 μm. The solutions are compared in the left panel of Fig. A.25 at $\varphi_s = 0°$. According to the discussion in Chapter III in this study, spatial resolution of the PSTD method is selected as 14. In the FDTD simulation, spatial resolution is 32. As shown in the panel, the solutions of the two methods agree well at all scattering angles except for the difference at scattering angle $85°$. Thus, in this study, the PSTD method is about 8 to 10 times more efficient than the FDTD method for similar accuracy. The PSTD method can be applied to a larger-scale calculation. Phase function of a hexagonal ice plate with size parameter 50 obtained from the PSTD method is shown in the right panel of Fig. A.25 at $\theta_i = 45°$, $\varphi_i = 0°$ and $\varphi_s = 0°$. The spatial resolution of this calculation is 12.

Figure A.26 shows phase functions of hexagonal ice columns. In the left panel, the PSTD method solutions are compared with the corresponding FDTD method results at size parameter 20. In this calculation, the spatial resolution of the FDTD method is changed to 28. As shown in this figure, there is good agreement between the two methods except for the differences at scattering angles near $85°$, $110°$, $130°$, and $160°$. In contrast to the comparison in Fig. A.25, in Fig. A.26, the FDTD results with coarser spatial resolution obviously deviate from the corresponding PSTD solutions at several scattering angles, particularly if the difference at $85°$ is larger. Therefore, the differences between the two methods are more likely caused by the simulation errors of the FDTD method rather than the PSTD method. In the right panel of Fig. A.26, phase function of the hexagonal column with size parameter of 50 calculated by the PSTD method is shown at $\theta_i = 45°$, $\varphi_i = 0°$ and $\varphi_s = 0°$.

4.2.2 Hollow hexagonal column

The hollow hexagonal column is one very important ice crystal habit. In cirrus clouds, it has been found that 90% hexagonal columns are hollow type. As shown in the left panel of Fig. A.27, cavity depth (d) is used to specify the ice column with hollow structure in addition to its side length (a) and length (L). Similar to the solid hexagonal column, the aspect ratio of the hollow column can be obtained by Eq. (4.1). In this study, cavity depth (d) is selected as:

$$d = 0.25L.\tag{4.3}$$

The orientation of the hollow hexagonal column in a laboratory coordinate is shown in the right panel of Fig. A.27, in which the principal axis of the column is selected as the z axis and the x axis passes through one edge of this column. Incident angles θ_i and φ_i are defined in this coordinate also.

Figure A.28 is essentially the same as Fig. A.25 except for the geometry of the hollow hexagonal ice column. In the left panel, solutions of the PSTD and FDTD methods are compared at size parameter 20; in the right panel, the PSTD method solutions are shown at size parameter of 50. It is evident that at a size parameter of 20, the PSTD solutions with spatial resolution 14 are essentially the same as the FDTD results with spatial resolution 32 at all scattering angles except for the differences at the scattering angles where the maxima or minima of phase functions occurs. Therefore, the PSTD method is approximately 8 to 10 times efficient than the FDTD method.

4.2.3 Bullet rosette

As discussed by Heymsfield and Miloshevich in 2002 [87], in ice clouds, the bullet is one of the most important structures, and nearly all of the ice crystals with maximum dimensions larger than 100 μm are either bullet rosettes or bullet rosette aggregates. In this study, a rosette which consists of six bullets is defined. As shown in the right panel of Fig. A.29, in a laboratory coordinate, the rosette is specified by arranging the six bullets along the forward and backward directions of the x, y, z axes. A single bullet of

this rosette is shown in the left panel of Fig. A.29. Following Yang's definition [23], a bullet is specified in the terms of its side length (a), length (L) and the pyramidal tip high (h). Aspect ratio of the bullet (2a/L) can be obtained from the following relation:

$$D = 2.3104L^{0.63}, \tag{4.4}$$

where D (D=2a) is the width of the bullet and the unit of d and L is micron. According to Greenler [88], keeping the inclination angle referred to the principal axis of the bullet 28°, the pyramidal tip high (h) is determined as:

$$h = 0.4605a, \tag{4.5}$$

where the unit of h is micron. Size parameter of this geometry is defined as kL.

Phase functions of an ice bullet rosette with size parameter 20 are calculated by the PSTD and FDTD methods. The solutions are compared in the left panel of Fig. A.30 at $\theta_i = 45°$, $\varphi_i = 0°$ and $\varphi_s = 0°$. It is evident that the solutions of the two methods are essentially the same except for some slight differences at the scattering angles of 30°, 90°, and 150°. Therefore, the PSTD method (in which spatial resolution is 14) is much more efficient than the FDTD method (with a spatial resolution of 32) for similar accuracy. The bullet rosette phase functions from the PSTD method are also shown in the right panel of this figure at size parameter of 50 and spatial resolution of 12.

4.2.4 Aggregate

Aggregate is normally observed in the terrestrial atmosphere. In this study, we construct the geometry by following the discussion of Yang and Liou [48]. The numerical definition of this geometry in laboratory coordinate is shown in Fig. A.31, in which eight hexagonal columns with the different spatial coordinates, size parameters, and aspect ratios are tightly attached without overlap. Size parameter is defined as the maximum dimension (D) multiplied by π/λ.

Solutions of aggregate ice crystals are shown in Fig. A.32, which is essentially the same as Fig. A.30 except for the geometry of aggregate. In the left panel, the PSTD solutions with spatial resolution 14 are compared with the corresponding FDTD results with spatial resolution 32 at size parameter of 20. The two methods agree very well except for slight differences at the scattering angles of 30° and 60°.. Phase functions of aggregate with size parameter of 50 are efficiently calculated by the PSTD method and are shown in the right panel.

4.2.5 Droxtal

Small ice crystals are frequently observed in the uppermost layer of cirrus clouds and polar stratospheric clouds where the temperature is extremely low. These small ice particles were described as "quasi–spherical," and their optical properties were calculated by the Lorenz-Mie theory. However, the single-scattering properties of a particle are highly sensitive to its geometry. A more realistic numerical geometry, droxtal, is used to describe the small ice crystals. Yang [25] first applied the FDTD method to

droxtal in 2003 and discussed the deviation between droxtal and sphere solutions. The scattering properties of this geometry were calculated by the GOM method [48].

This study, following the definition of droxtal given by Yang [25], specifies this convex geometry in terms of its peripheral sphere. As shown in Fig. A.33, the droxtal structure consists of 12 isosceles trapezoid faces: six rectangular faces at the center of the crystal and two hexagonal faces at the top and bottom of the crystal. In this figure, the geometry is defined in a coordinate frame in which both the mass center of this ice crystal and the center of its peripheral sphere are located at the origin of this frame. The z axis crosses the center of the top of this crystal, and the y axis passes through the center of a rectangular face. As shown in the figure, all vertices of convex geometry located on the peripheral sphere are specified in terms of R, α_1 and α_2, where R is the radius of the peripheral sphere. From Fig. A.33, we can determine the h_1 and h_2 from the follow relations:

$$h_1 = R\cos(\alpha_1),\ h_2 = R\cos(\alpha_2), \tag{4.6}$$

where in this study the two angles, α_1 and α_2 are selected as $32.35°$ and $71.81°$, respectively. For droxtal, we define size parameter as kR, where k is the wave number.

Figure A.34 shows the phase functions of ice droxtals at incident wavelength 3.7 μm. In the left panel, the solutions of the PSTD and FDTD methods are compared at size parameter of 20 and $\theta_i = 45°$, $\varphi_i = 0°$ and $\varphi_s = 0°$. In this comparison, the PSTD solutions follow the corresponding FDTD results at most scattering directions except for

differences at some scattering angles where the phase function maxima or minima occur. Phase function of an ice droxtal with size parameter of 50 is also calculated by the PSTD method. The solutions are shown in the right panel of Fig. A.34.

4.3 Conclusion

In this chapter, the PSTD method was applied to the scattering of light by ice crystals with various geometries. Phase function of a sphere with refractive index of 1.05+0j and size parameter of 20 was calculated from the PSTD and FDTD methods, respectively. The solutions from the two methods were compared with the corresponding Mie results. In this comparison, the FDTD solutions with spatial resolution of 26 substantially deviated from the Mie method at scattering angles160° through 180°. The PSTD method with a very coarse spatial resolution of 8 agreed very well with the Mie theory at all scattering angles. Six ice crystal shapes (hexagonal plate, hexagonal column, hollow hexagonal column, bullet rosette, aggregate and droxtal) were defined by the PSTD method. The solutions of the PSTD and FDTD methods were compared in terms of phase functions of these six ice habits with size parameter of 20 and incident wavelength of 3.7. It is evident that the PSTD method with a spatial resolution of about 15 provides similar accuracy to the FDTD method with a resolution of about 35. The PSTD method is approximately 8 times more efficient than the FDTD method. Therefore, the phase functions of ice crystals with size parameter 50 can be calculated by this method.

CHAPTER V[*]

HORIZONTALLY ORIENTED HEXAGONAL AND CIRCULAR ICE CRYSTALS: APPLICATION AND COMPARISON OF THE LIGHT SCATTERING METHODS, PSTD, FDTD AND T-MATRIX

5.1 Introduction

Understanding of the radiative properties of cirrus clouds that cover more than 20% of the globe is essential to better understanding of the terrestrial climate system and its evolution [89–92]. The pristine ice crystals within cirrus clouds have hexagonal structures, which are associated with various optical phenomena in the atmosphere [93]. In addition to the nonspherical effect of ice crystals, the orientations of these particles is also important to their optical properties. In the atmosphere, large ice crystals tend to have horizontal orientations in terms of the spatial orientations of their longest axes, as demonstrated by Platt using LIDAR measurements for ice plates [94]. Stephens [95] demonstrated the importance of the shapes and orientations of nonspherical particles in radiation transfer calculations. While the errors associated with the neglect of nonsphericity of ice crystals in dealing with cirrus radiative properties can be substantial, the influence of the specific orientations of the long cylinders on cloud albedo,

---

[*] Part of this chapter is reprinted with permission from "Scattering phase functions of horizontally oriented hexagonal ice crystals" by Guang Chen, Ping Yang, G.W. Kattawar and M.I. Mishchenko, 2006, *J. Quant. Spectro. Rad. Transfer*.,100,91-102,Copyright [1999] by Elsevier Science Ltd.

absorption, and emission can also be significant in comparison with the case for randomly oriented ice crystals. Therefore, the scattering properties of oriented crystals should be studied as functions of both the scattering zenith and azimuth angles. Rockwitz [96] has discussed the scattering properties of horizontally oriented ice columns using the ray-tracing method, which is used in cases with very large size parameters. The single-scattering properties of oriented particles with rotational symmetric geometries have also been discussed by Mishchenko et al. [57] using the rigorous T-matrix method.

This study first compares the solutions based on the FDTD and T-matrix methods for the phase matrix of oriented circular cylinders. The phase matrix elements P_{11}, P_{12}, P_{33}, and P_{34} from the two methods are compared at wavelengths of 0.55 μm and 12 μm. The comparison validates the applicability of the FDTD method for oriented particles. Furthermore, we apply the FDTD method to the scattering of light by horizontally oriented hexagonal particles at size parameter 10 in which several schemes are employed to average the particle orientations. The PSTD method, whose applicability for oriented particles has been validated in Chapters III and IV, is then used to investigate the scattering of light by horizontally oriented hexagonal ice plates with various aspect ratios and size parameters at wavelengths 0.532 μm and 1.064 μm. Note that horizontally oriented particles, such as columns, can have arbitrary orientations with one-dimensional freedom in terms of the arbitrary orientations of their principal axes in a horizontal plane. Horizontally oriented particles can have, arbitrary orientations with 2-D freedom for the case where the particle principal axes are arbitrarily oriented in a

horizontal plane where the particles may also have random rotational angles around their axes. Therefore, the resultant anisotropic phase functions depend on scattering zenith angle and also on the azimuthal angle of the scattering plane of interest. Lee et al. [97] investigated the feasibility of using circular cylinders as surrogates of randomly oriented hexagonal ice crystals in the computation of the scattering properties of the latter. In this study, we investigate the feasibility and errors associated with using circular cylinders as surrogates for hexagonal columns or plates in computing the optical properties of horizontally oriented ice crystals. The T-matrix theory [57] is used to calculate the scattering properties of circular cylinders.

5.2 Definitions

Two geometries, circular cylinders and hexagonal prisms, are considered in this study. Similar to characterization in the section 4.2.2, a circular cylinder is specified in terms of the radius of its cross section (r) and length (L). A hexagonal prism is defined in terms of its side length (a) and length (L). The aspect ratios for these particles are defined as r/L for circular cylinders and a/L for hexagonal prisms. The size parameters of the particles are defined as k (the wave number = $2\pi/\lambda$) multiplied by the largest dimension of the particles, where λ is the incident wavelength. When L is larger than 2r or 2a, size parameters are defined as kL; otherwise, size parameters are defined as ka or kr.

In this study, we use six angles, φ_p, θ_p, ψ_p, θ_i, θ_s, and φ_s to specify the incidence scattering configuration for oriented particles. Consider the scattering of

sunlight by ice crystals in the atmosphere. As shown in Fig.A.35, the incident angle with respect to the zenith direction is denoted by θ_i. For scattering particles with horizontal orientations, their single-scattering properties depend on both the scattering angle (θ_s) and the azimuth angle (φ_s) of a scattering plane to which the scattering properties are refereed. The principal scattering plane, a plane with $\varphi_s = 0$, contains the zenith and incident directions. An interesting point to note is that some oriented particles (e.g., circular plates with vertical orientations of their axes) are mirror-imaging symmetrical about the principal plane. This symmetry leads to some unique features of the scattering properties of the particles, as will be demonstrated in Section 3.

In the present numerical computation, we defined a laboratory coordinate system, OXYZ, and a particle coordinate system, $OX_pY_pZ_p$. The particle system is fixed to the corresponding scattering particle and rotates with the particle. The relative orientation of the particle coordinate system with respect to the laboratory system is specified by three Euler angles, φ_p, θ_p and ψ_p, where $\varphi_p \in [0,2\pi]$ is the counterclockwise rotation about the z axis, $\theta_p \in [0,\pi]$ is the rotation about the new rotated x-axis, and $\psi_p \in [0,2\pi]$ is the rotation about the new z axis again, as shown in the upper panel of Fig. A.36. Note that to define the particle system, the rotations specified by the three Euler angles are those by sequentially given by φ_p, θ_p and ψ_p. The lower panels of Fig. A.36 show the geometries of a hexagon and a circular cylinder in the particle system.

As described by Platt [94], ice plates (L < 2a) or columns (L > 2a) in ice clouds prefer to have their longest dimension oriented horizontally. In this case, the

corresponding phase matrix elements are functions of scattering zenith angle, θ_s and azimuthal angle, φ_s. In this study, three schemes are applied to the average of the particle orientations that can be arbitrary but confined to be horizontal for computing the scattering properties of hexagonal particles. As shown in the left panel of Fig. A.37, hexagonal plates can have random rotational angles about their symmetry axis (z axis), whereas their principal axes are vertically oriented. In the present computation of the scattering properties of hexagonal plates, 120 orientations with the rotation angles from 0°to 360°with a resolution of 3° are used. As shown in the right panel of Fig. A.37, the hexagonal columns can have 1-D or 2-D arbitrary orientations. For the 1-D orientations, the particles can have arbitrary rotation about the z axis. The number of orientations assumed for the present computation is 18 with a resolution of 20°for the rotation about the z axis from 0° to360°. For the arbitrary orientation, the columns not only rotate horizontally about the z axis, but also spin about their symmetry axes. In this case, the orientation resolution is 18×24, where 18 indicates the rotations about the z axis and 24 indicates the rotations about the principal axis (with a resolution of15°). In this study, the scattering properties of horizontally oriented particles are also compared with those of 3-D randomly oriented particles. For the 3-D randomly oriented particles, 24×18×360 orientations are accounted for, where 24 is the number of the incident azimuth angles, 18 is the number of the incident zenith angles, and 360 is the number of the scattering azimuth angles. We find little improvement on the accuracy of the results, if the angular resolution for averaging the particle orientations increases further. The mean phase

matrix averaged for particle orientations can be written as follows:

$$\langle P(\theta_s,\varphi_s)\rangle = \frac{\int_{\varphi_1}^{\varphi_2}d\varphi_p\int_{\theta_1}^{\theta_2}\sin\theta_p d\theta_p\int_{\psi_1}^{\psi_2}P(\varphi_p,\theta_p,\psi_p,\theta_s,\varphi_s)C_{sca}(\varphi_p,\theta_p,\psi_p,\theta_s,\varphi_s)d\psi_p}{\int_{\varphi_1}^{\varphi_2}d\varphi_p\int_{\theta_1}^{\theta_2}\sin\theta_p d\theta_p\int_{\psi_1}^{\psi_2}C_{sca}(\varphi_p,\theta_p,\psi_p,\theta_s,\varphi_s)d\psi_p} \quad , \quad (1)$$

where $P(\varphi_p,\theta_p,\psi_p,\theta_s,\varphi_s)$ and $C_{sca}(\varphi_p,\theta_p,\psi_p,\theta_s,\varphi_s)$ are the phase matrix and the

scattering cross section for one specific orientation, respectively.

In the FDTD and PSTD methods the grid resolution specified in terms of

$n=\lambda/\Delta s$, where λ is the incident wavelength, is a key parameter that determines the

accuracy of the numerical solutions and the corresponding computational effort. In this

study, for the FDTD method, we select $n = 25m_r$, in which m_r is the real part of the

refractive index of the particle; for the PSTD method, we select $n = 12$.

5.3 Validation of the FDTD method for oriented particles

The FDTD and T-matrix methods are used to compute the phase matrices for a circular cylinder with a unit aspect ratio and a fixed orientation at wavelengths of 12 μm and 0.55 μm. The complex refractive index of ice at these two wavelengths are (1.2799, 0.4133) and (1.311, 0.311×10^{-8}) taken from the data sets of Warren [98]. As shown in the left panel at the bottom of the Fig. A.36, in the laboratory coordinate system, the Z axis is chosen as the symmetry axis of the ice cylinder. The solutions are compared for a scattering azimuth angle, φ_s, of $0°$, and two incident angles, $30°$ and $60°$. According to the discussion in the preceding discussion, we notice that at a scattering azimuth angle of $0°$, the scattering plane coincides with the principal plane. If a particle has a symmetric geometry about the principal plane, the mirror-imaging symmetry about the scattering plane is observed, which does not change with the scattering angle. Therefore, in the corresponding amplitude matrix, S_3 and S_4 are expected to be zero due to the transformation properties associated with the scattering properties of a scattering particles (or a particle) consisting of a two mirror-imaging symmetric components. Consequently, in the corresponding phase matrix, elements of P_{13}, $P_{14,}$ P_{23}, P_{24}, P_{31}, $P_{32,}$ P_{41} and P_{42} are zero, and P_{22}/P_{11} is unit. Note that the deviation of P_{22}/P_{11} from unity can normally be regarded as an indication of the nonsphericity of a scattering particle [99, 100]. This indication is not always true for particles with specific orientations. Phase element, $P_{22}/P_{11,}$ of a fixed oriented hexagonal column is shown in Fig. A.38 at a wavelength of 12 μm and an incident angle of $30°$. We observe that P_{22}/P_{11} is one as incident azimuth angle is zero (left panel) and P_{22}/P_{11} is a function of the scattering

zenith angle at an incident azimuth angle of $15°$ (right panel). The relations given by $P_{12}=P_{21}$, $P_{33}=P_{44}$ and $P_{43}=-P_{34}$ are also noticed. In the following P_{11}, P_{12}, P_{33} and P_{34} are discussed. It should be pointed out the comparison of the FDTD and T-matrix solutions for the scattering phase functions of ice crystals has been reported by Baran et al [101].

Figure A.39 shows the phase matrix elements P_{11}, P_{12}, P_{33} and P_{34} at a wavelength of 0.55 μm and an incident angle of $30°$. It is evident that the FDTD solution agrees well with the counterparts from the T-matrix at all scattering angles. For P_{11}, solutions are slightly different for angles near150º. For P_{12} and P_{43}, the FDTD and T-matrix results are essentially the same. For P_{33}, excellent agreement of the two solutions is also noticed except slight differences near 150º.

Figure A.40 is the same as Fig. A.39 except for an incident angle of 60º. In this case, the FDTD solutions essentially converge with the T-matrix results in terms of the phase function P_{11}. For the other three phase matrix elements, the FDTD solutions also agree with the T-matrix counterparts, except for P_{43}/P_{11} at 120º and 165º where the minima in these two quantities are occurred.

Figures A.41 and A.42 are the same as Figs. A.39 and A.40, respectively, except a wavelength of 12 μm is used for two computations reported in Figs. A.41 and A.42. At the 12-μm wavelength, ice is quite absorptive, as the imaginary part of the refractive index is 0.4133. Again, the FDTD solutions agree well with the T-matrix solutions except at some scattering angles where the maxima or minima of the phase matrix elements occur, particularly in the case when the incident angle is 30º (Fig. A 41).

5.4 Single-scattering properties of horizontally oriented hexagonal ice crystals and circular cylinders

The phase functions for the horizontally oriented hexagonal ice plates with an aspect ratio (a/L) of 2 are computed with the FDTD method on the basis of the previously described 1-D scheme for averaging the particle's horizontal orientations. The numerical computations are carried out at the wavelengths of 0.55 μm and 12 μm with three incident angles, 0º. 30º, and 60º. Figure A.43 shows the variations of phase functions of both hexagonal and cylindrical ice plates versus the scattering zenith and azimuth angles. Overall, the phase functions for the two particle geometries are quite similar. An interesting effect associated with the phase functions is the scattering maxima observed at $\theta_s = 120^\circ$ and $\varphi_s = 90^\circ$. These maxima are caused by the external reflection associated with the top face of ice plates.

Figure A.44 shows phase functions of horizontally oriented hexagonal columns with an aspect ratio of a/L=1/6 for two incident angles, 30º and 60º.The solutions on the basis of the previously described 1-D and 2-D orientation averaging schemes are shown in the first and second rows of Fig. A.44, respectively. The third row shows the phase functions of horizontally oriented circular ice cylinders. As a circular cylinder is rotationally symmetric about it principal axis, only 1-D orientation average is required. The reflection peaks caused by the external reflection of the column side faces are not significant as compared with the case for horizontally oriented plates. A comparison of the results in the first and second rows of Fig. A.44 indicates that at the scattering angles between 0º and 60º, the hexagonal columns with the two orientation-averaging schemes

have similar optical properties, and the relative differences due to the two different orientation-averaging schemes are less than 10%. At the other scattering angles, only slight differences are noticed. Therefore, the rotation about the principal axes of the columns does not have a significant influence on the mean phase functions.

Circular cylinders have been suggested as surrogates for hexagonal ice crystals in the literature. For example, Lee et al. [97] noticed that circular cylinders have similar scattering and absorption properties as hexagonal ice crystals when a random orientation condition is imposed at infrared wavelengths. The results shown in Figs. A.43 and A.44 indicate that circular cylinders can also be used as surrogates for hexagonal ice crystals even if horizontal orientations are considered. At the two wavelengths of 12 μm and 0.55 μm, the relative differences between the equivalent cylinder and the hexagonal plate are less than 4% in the forward direction and are less than 10% in the backward direction for all tilted incident cases. Therefore, in the cases of size parameter 10, a circular cylinder can be used as a surrogate for a horizontally oriented hexagonal plate in the computation of its scattering properties.

The influence of size parameter on the agreement of hexagonal plates and cylinders is investigated. On the basis of the previously described 1-D scheme for averaging the particle's horizontal orientations, the PSTD method is used to compute the phase functions for the horizontally oriented hexagonal ice plates with various aspect ratios (a/L) and size parameters (k2a) at the incident angle of 0°. Considering the symmetry of the incident configuration, in this study, the phase functions for the horizontally oriented plates depend only on the scattering angles (θ_s). The numerical

computations are carried out at the wavelengths of 0.532 μm and 1.064 μm. According to the data sets of Warren [98], the complex refractive index of ice at these two wavelengths are (1.3117, 2.6139×10^{-9}) and (1.3004, 1.9330×10^{-9}). The phase functions of ice circular cylinders with the same aspect ratios (r/L) and size parameters (k2r) are also calculated by the T-matrix method at the two wavelengths. The solutions from the PSTD and T-matrix methods are compared at aspect ratios, 0.5, 1, 2, and the largest dimension of the particles (2a or 2r), 2, 4, 6, 8 μm.

Figure A.45 shows the variations of phase functions of both hexagonal and cylindrical ice plates versus the aspect ratios and largest dimension of the particles at wavelength 0.532 μm. When the largest dimension is smaller than 6 μm—the corresponding size parameter is about 35—the phase functions for the two-particle geometries are quite similar for all aspect ratios in which the similarity increases with the particle size. However, in the cases of 2a=2r=8 μm, the solutions of the hexagonal plates with aspect ratios 0.5 and 2 obviously deviate from the corresponding results of the cylinders. The reflection peaks caused by the external reflection of the top face of the ice plates are also observed at the backward scattering direction.

Figure A.46 is substantially the same as Fig. A.45 except for incident wavelength of 1.064 μm. Similar to the cases of wavelength 0.532 μm, maxima of the phase functions due to the external reflection of the top face occurs at the backward direction. Overall, the circular cylinder results agree with the solutions of hexagonal plates at most of the scattering angles except in the case of aspect ratio 2 and 2a=2r=2 μm in which obvious discrepances are observed in the comparison. Therefore, when size parameter is

in the region of approximately from 10 to 40, a circular cylinder can be used as a surrogate for a horizontally oriented hexagonal plate with various aspect ratios in the computation of its scattering properties.

Figure A.47 shows the comparison of phase functions for 1-D horizontally and 3-D randomly oriented ice crystals. An incident angle of 0° is used for the computation for the horizontally oriented particles. The randomly oriented results are substantially different from the horizontally oriented solutions. Particularly for the strong absorption case, the back scattering of horizontally oriented plates caused by the external reflections is approximately 50 times of the counterpart of the randomly oriented particle.

5.5 Conclusions

We compared the FDTD method for the computation of the scattering properties of oriented nonspherical particles with solutions from the T-matrix method. The PSTD method is used to calculate the phase functions of horizontally oriented hexagonal ice plates with various aspect ratios and particle sizes. Three numerical schemes are used to average the particle horizontal orientations for hexagonal plates and columns. The corresponding randomly oriented solutions are also calculated with the FDTD method. The phase functions of horizontally oriented hexagonal plates are sensitive to the scattering azimuth angle, and are substantially different from the randomly oriented results. In the cases of size parameter 10, the phase functions of the equivalent cylinders agree well with the corresponding counterparts of hexagonal ice crystals at all incident angles at a wavelength of 12 μm. At a wavelength of 0.55 μm,

some discrepancies are noted at the scattering angles when the reflection peaks for the horizontal oriented plate results occur. The comparisons of phase functions for the hexagonal columns with 1-D and 2-D orientation-averaging schemes indicate that the results are not sensitive to the rotation of the particles around their principal axes. When the size parameter is in the region from about 10 to 40, the solutions of the horizontally oriented hexagonal plates with various aspect ratios follow the corresponding results of the equivalent cylinders at most of scattering angles. The agreement of the two geometries increases with the particle size. Otherwise, when the size parameter is too small or too large, the results of the equivalent cylinders may obviously deviate from the solutions of the hexagonal plates. Therefore, the equivalent circular cylinders can be applied as surrogates for hexagonal columns at moderate size parameter.

CHAPTER VI

CONCLUSION AND SUMMARY

In the atmosphere, nonspherical particles with size parameter in the range of 20 to 60 cannot be accurately calculated by known single-scattering methods and theories. This study applies the pseudo-spectral time-domain (PSTD) method (which was first developed for acoustic wave propagation) to study scattering properties of arbitrary geometries with moderate size. In contrast to the FDTD method, a high order accurate approximation of spatial derivative is employed for more efficient simulation in the PSDT method. In this method, Maxwell's equations can be discretized by five different methods in the time domain. Perfectly matched layer (PML) conditions are employed to eliminate the wraparound effect and truncate the computation region. Furthermore, we evaluate the mean electromagnetic properties in terms of permittivity and permeability to decrease Gibb's phenomenon associated with the discontinuity of the particle surface. Applicability of the PSTD method for light scattering is feasible.

3-D PSTD codes associated with the five discretization methods in the Cartesian coordinate provide essentially the same solutions in both nonabsorptive and absorptive cases. In comparison with the Mie theory, the PSTD method provides excellent agreement in terms of phase functions at any scattering direction. Although some slight errors occur at the scattering angles where phase functions have the maxima or minima, no accumulated error, which increases with the simulations scale and time, is observed in this method. Phase functions from the two methods even agree well at size parameter 80.

According to the numerical experiments, the grid spatial resolution of the PSTD method can be selected as follows: When size parameter is smaller than 30, the grid spatial resolution can be determined as 10 multiplied by the real part of the refractive index (m_r); otherwise, if m_r is smaller than 1.5, the resolutions is selected as 12; and if m_r is larger than 1.5 and smaller than 2.0, the spatial resolution is determined as 9 multiplied by m_r. Phase functions of spheroid and circular cylinders with various aspect ratios are calculated by the PSTD method. In comparison with the T-matrix method, the PSTD method shows better agreement for nonspherical particles.

The PSTD method is applied to light scattering of nonspherical ice crystals. Six geometries (hexagonal plate, hexagonal column, hollow hexagonal column, bullet rosette, aggregate and droxtal) are defined in this study. The PSTD and FDTD solutions of these ice crystals are compared at size parameter 20 and incident wavelength 3.7 μm. The PSTD method is about 8-10 times more efficient than the conventional FDTD method for an acceptable accuracy. Phase functions of the ice crystals with size parameter 50 are also calculated by the PSTD method.

Scattering properties of horizontally oriented ice crystals are calculated by the PSTD, the FDTD and T-matrix methods. In this study, three numerical methods are employed to average the particle orientations. The feasibility of using a circular cylinder as a surrogate of the horizontally oriented hexagonal prism is discussed in the phase function comparisons of the two geometries. When size parameter is in the region of approximately 10 to 40, hexagonal ice crystals and circular cylindrical ice particles have similar optical properties; particularly, at a strongly absorbing wavelength, if the two

particle geometries have the same length and aspect ratio. When size parameter is smaller than 10 or larger than 40, the results of the equivalent circular cylinders substantially deviated from the corresponding solutions of the hexagonal ice crystals.

REFERENCES

1. Ackerman T.P., Liou K.N., Valero E.P.J. and Pfiste L. Heating rates in tropical anvils. J. Atmos. Sci. 1988 ; 45: 1606-1623.

2. Bretherton F.P. and Suomi V.E. First internal satellite cloud climatology project regional experiment (FIRE) research plan. National Climatic Program Office, 1983.

3. Wylie D.P. and Menzel W.P. Two years of cloud cover statistics using VAS. J. Climate 1989; 2: 380-392.

4. Ramaswamy V. and Ramanathan V. Solar absorption by cirrus clouds and the maintenance of the tropical upper troposphere thermal structure. J. Atmos. Sci. 1989; 46: 2293-2310.

5. Stephens G.L. Tsay S., Stackhouse P.W.Jr. and Flatau P.J. The relevance of the microphysical and radiative properties of cirrus clouds to climate and climate feedback. J. Atmos. Sci. 1990; 47: 1742-1753.

6. Liou K.N., Takano Y. and Yang P. Light scattering and radiative transfer by ice crystal clouds: applications to climate research. In Mishchenko M.I., Hovenier J.W., and Travis L.D. Light Scattering by Nonspherical Particles: Theory, Measurements, and Geophysical Applications, San Diego: Academic Press, 2000; p. 417–449.

7. Fu Q., Yang P., and Sun W.B. An accurate parameterization of the infrared radiative properties of cirrus clouds for climatemodels. J. Clim. 1998; 25: 2223–2237.

8. Fu Q., Sun W.B. and Yang P. On model of scattering and absorption by cirrus nonspherical ice particles at thermal infrared wavelength. J. Atmos. Res. 56, 2937–

2947 (1999).

9. Chepfer H., Goloub P., Riedi J., Haan J.D., Hovenier J. W., and Flamant P.H. Ice crystal shapes in cirrus clouds derived from POLDER-1_ADEOS-1. J. Geophys. Res. 2001; 106: 7955–7966.

10. Baran A.J. Simulation of infrared scattering from ice aggregatesby use of a size-shape distribution of circular ice cylinders. Appl. Opt. 2003;42: 2811–2818.

11. Minnis P., Heck P.W. and Young D.F. Inference of cirrus cloud properties from satellite observed visible and infrared radiances. Part II: verification of theoretical radiative properties. J. Atmos. Sci. 1993; 50: 1305–1322.

12. Reichardt J., Reichardt S., Hess M. and McGee T.J. Correlations among the optical properties of cirrus-cloud particles: microphysical interpretation. J. Geophys. Res. 2002; 107: 4562.

13. Mishchenko M.I., Rossow W.B., Macke A. and Lacis A.A. Sensitivity of cirrus cloud albedo, bidirectional reflectance and optical thickness retrieval accuracy to ice particle shape. J. Geophys. Res. 1996;101: 16973–16985.

14. Takano Y. and Liou K.N. Solar radiative transfer in cirrus clouds. Part I. Single-scattering and optical properties of hexagonal ice crystals J. Atmos. Sci. 1989; 46: 3–19.

15. Takano Y. and Liou K.N. Radiative transfer in cirrus clouds. III. Light scattering by irregular ice crystals. J. Atmos. Sci. 1995; 52: 818–837.

16. Macke A., Mueller J., and Raschke E. Single scattering properties of atmospheric ice crystal. J. Atmos. Sci. 1996; 53: 2813–2825.

17. Sun W., Fu Q., and Chen Z. Finite-difference time-domain solution of light scattering by dielectric particles with perfectly matched layer absorbing boundary conditions. Appl. Opt. 1999; 38: 3141–3151.

18. Baran A. J., Haveman S., Francis P. N., and Yang P. A study of the absorption and extinction properties of hexagonal ice columns and plates in random and preferred orientation, using exact T-matrix theory and aircraft observations of cirrus. J. Quant. Spectrosc. Radiat. Transfer 2001; 70: 505–518.

19. Yang P. and Liou K.N. Finite-difference time domain method for light scattering by small ice crystals in three-dimensional space. J. Opt. Soc. Am. 1996; A 13: 2072–2085.

20. Muinonen K. Scattering of light by crystals: a modified Kirchhoff approximation. Appl. Opt. 1989; 28: 3044–3050.

21. Macke A. Monte Carlo calculations of light scattering by large particles with multiple internal inclusions. In Mishchenko M. I., Hovenier J. W., and Travis L. D. Light Scattering by Nonspherical Particles: Theory, Measurements, and Applications, San Diego: Academic Press, 2000; p. 309–322.

22. Yang P. and Liou K. N. Geometric-optics-integral-equation method for light scattering by nonspherical ice crystals. Appl. Opt. 1996; 35: 6568–6584.

23. Yang P., Liou K. Wyser N., K. and Mitchell D. Parameterization of scattering and absorption properties of individual ice crystals. J. Geophys. Res. 2000; 105: 4699–4718.

24. Yang P., Gao B. C., Baum B. A., Hu Y. X., Wiscombe W. J., Tsay S. C., Winker D.

M. and Nasiri S. L. Radiative properties of cirrus clouds in the infrared (8–13μm) spectral region J. Quant. Spectrosc. Radiat. Transfer 2001; 70: 473–504.

25. Yang P., Baum B. A., Heymsfield A. J., Hu Y. X., Huang H.-L., Tsay S.-C., and Ackerman S. Single-scattering properties of droxtals. J. Quant. Spectrosc. Radiat. Transfer 2003; 79–80: 1159–1180.

26. Yang P., Mlynczak M. G., Wei H. L., Kratz D. P., Baum B. A., Hu Y. X., Wiscombe W. J., Heidinger A. and Mishchenko M. I. Spectral signature of ice clouds in the far-infrared region: single-scattering calculations and radiative sensitivity study. J. Geophys. Res. 2003; 108: 4569, 10.1029/2002JD2002JD003291.

27. Baum B. A., Kratz D.P., Yang P., Ou S.C., Hu Y., Soulen P. and Tsay S.C. Remote sensing of cloud properties using MODIS airborne simulator imagery during SUCCESS. I. Data and Models. J. Geophys. Res. 2000; 105: 11,767-11,780.

28. King M.D., Platnick S., Yang P., Arnold G. T., Gray M. A. Riedi J. C., Ackerman S.A. and Liou K. N. Remote sensing of liquid water and ice cloud optical thickness, and effective radius in the arctic: application of air-borne multispectral MAS data. J. Atmos. And Ocean. Technol. 2004; 21: 857-875.

29. Gao B.-C., Meyer K. and Yang P. A new concept on remote sensing of cirrus optical depth and effective ice particle size using strong water vapor absorption channels near 1.38 and 1.88 μm. IEEE Trans. Geosci. Remote Sens. 2004; 42: 1891-1899.

30. Loeb N.G., Manalo-Smith N. Top-of-atmosphere direct radiative effect of aerosols over global oceans from merged CERES and MODIS observations. J Climate 2005;

18: 3506-3526.

31. Lohmann U, Feichter J. Global indirect aerosol effects: a review. Atmos Chem Phys 2005;5:715–737.

32. Bates TS, Anderson TL, Baynard T., Bond T., Boucher O., Carmichael G., Clarke A., Erlick C., Guo H., Horowitz L., Howell S. Kulkarni S., Maring H., McComiskey A., Middlebrook A., Noone K., O'Dowd CD, Ogren J., Penner J., Quinn PK, Ravishankara AR, Savoie DL, Schwartz SE, Shinozuka Y., Tang Y., Weber RJ, Wu Y. Aerosol direct radiative effects over the northwest Atlantic, northwest Pacific, and North Indian Oceans: estimates based on in-situ chemical and optical measurements and chemical transport modeling. Atmos Chem Phys 2006; 6: 1657–1732.

33. Schulz M, Textor C, Kinne S., Balkanski Y., Bauer S., Berntsen T., Berglen T., Boucher O., Dentener F., Guibert S., Isaksen ISA, Iversen T., Koch D., Kirkevag A., Liu X., Montanaro V., Myhre G., Penner JE, Pitari G., Reddy S., Seland O., Stier P., Takemura T. Radiative forcing by aerosols as derived from the AeroCom present-day and pre-industrial siulations. Atmos Chem Phys 2006; 6: 5225–46.

34. Penner JE, Quaas J., Storelvmo T., Takemura T., Boucher O., Guo H., Kirkevag A., Kristjansson JE., Seland O. Model intercomparison of indirect aerosol effects. Atmos Chem Phys 2006; 6: 3391–405.

35. Yu H, Kaufman YJ, Chin M., Feingold G., Remer LA, Anderson TL, Balkanski Y., Bellouin N., Boucher O., Christopher S., DeCola P., Kahn R., Koch D., Loeb N., Reddy MS, Schulz M., Takemura T., Zhou M. A review of measurement-based

assessments of the aerosol direct radiative effect and forcing. Atmos Chem Phys 2006; 6: 613–66.

36. Heymsfield A.J., and Platt C.M.R. A parameterization of the particle size spectrum of ice clouds in terms of the ambient temperature and ice water content. J. Atmos. Sci. 1984; 41:846-855.

37. World Climate Program, Report of the expert meeting on aerosols and their climatic effects. Williamsburg, Virginia, 28-30 March 1983, Report WCP-55, World Meteorological Organization. 1983; p. 107.

38. Rayleigh JWS. On the light from the sky, its polarization and colour. Phil. Mag. 1871; 41:107-120, 274-279.

39. Mie G. Beigrade zur optik truber medien, speziell kolloidaler metallosungen. Ann. Physic. 1908; 25:377-445.

40. Kattawar G. W. and Plass G. N. Electromagnetic scattering from absorbing spheres. Applied Optics 1967; 6:8:1377-1382.

41. Yang P., Gao B.C. Wiscombe W. J., Mishchenko M. I., Platnick S. E., Huang H.-L., Baum. B. A., Hu Y. X, Winker D. M., Tsay S.C. and Park S. K. Inherent and apparent scattering properties of coated or uncoated spheres embedded in an absorbing host medium. Applied Optics 2002; 41:15:2740-2759.

42. Videen G., Ngo D. and Hart M.B. Light scattering from a pair of conducting osculating spheres. Opt. Comm. 1996; 125: 275-287.

43. Asano S. and Yamamoto G. Light scattering by a spheroidal particle. Appl. Opt. 1975; 14: 29-49.

44. Mugnai A. and Wiscombe W.J. Scattering from nonspherical Chebyshev particles. Appl. Opt. 1986; 25:1235-1244.

45. Takano Y. and Liou K.N. Solar radiative transfer in cirrus clouds. Part I: single scattering and optical properties of hexagonal ice crystals. J. Atmos. Sci. 1989; 46: 3-19.

46. Yang P. and Liou K.N. Geometric-Optics-integral-equation method for light scattering by nonspherical ice crystals. Appl. Opt., 1996; 35: 6568-6584.

47. Yang P. and Liou K.N. Single-scattering properties of complex ice crystals in terrestrial atmosphere. Contr. Atmos. Phys. 1998; 71:223-248.

48. Zhang Z.B., Yang P., Kattawar G.W., Tsay S.-C., Baum B.A., Huang H.-L., Hu Y.X. Heymsfield A.J. and Reichardt J. Geometric optics solution to light scattering by droxtal ice crystals. Appl. Opt. 2004; 43: 2490-2499.

49. Yee K. S. Numerical solution of initial boundary value problems involving Maxwell's equation in isotropic media. IEEE Transactions on Antennas and Propagation 1966; AP-14: 302-307.

50. Yang P. and Liou K.N. Light scattering by hexagonal ice crystal: comparison of finite-difference time domain and geometric optics methods. J. Opt. Soc. Amer. 1995; A12: 162-176.

51. Yang P., Liou K.N. and Arnott W.P. Extinction efficiency and single-scattering albedo of ice crystals in laboratory and natural cirrus clouds. J. Geophys. Res. 1997; 102: 21,825-21,835.

52. Yang P., Liou K.N., Mishchenko M.I. and Gao B.-C. An efficient finite-difference

time domain scheme for light scattering by dielectric particles: application to aerosols. Appl. Opt. 2000; 39: 3727-3737.

53. Waterman P.C. Symmetry, unitarity and geometry in electromagnetic scattering. Phys. Rev. 1971; D3: 825-839.

54. Mishchenko M. I., and Travis L. D. Capabilities and limitations of a current FORTRAN implementation of the T-matrix method for randomly oriented rotationally symmetric scatterers. J. Quant. Spectrosc. Radiat. Transfer 1998; 60: 309-324.

55. Borrmann S., Luo B. and Mishchenko M. Application of the T-matrix method to the measurement of aspherical (ellipsoidal) particles with forward scattering optical particle counters. J. Aerosol Sci. 2000; 31: 789-799.

56. Wielaard D.J., Mischenko M.I., Macke A. and Carlson B.E. Improved T-matrix computations for large, nonabsorbing and weakly absorbing nonspherical particles and comparison with geometrical-optics approximation. Appl. Opt. 1997; 36: 4305-4313.

57. Mishchenko MI. Calculation of the amplitude matrix for a nonspherical particle in a fixed orientation. Appl. Opt. 2000; 39:1026-1031.

58. Van de Hulst H. C. Light Scattering by Small Particles. New York: Wiley, 1957.

59. Mitchell D. L. and Arnott W.P. A model prediction the evolution of ice particle size spectra and radiative properties of cirrus clouds. Part II: dependence of absorption and extinction on ice crystal morphology. J. Atmos. Sci. 1994; 51:817-832.

60. Purcell E. M. and Pennypacker C. P. Scattering and absorption of light by

nonspherical dielectric grains. Astrophys. J. 1973; 196:705-714.

61. Draine B.T. The discrete-dipole approximation and its application to interstellar graphite grains. Astrophys. J. 1988; 333: 848-873.

62. Liu Q.H. Generalization of the K-space formulation to elastodynamic scattering problems. Journal of the Acoustical Society of America 1995; 97: 1373-1379.

63. Liu Q.H. The pseudo-spectral time-domain (PSTD) algorithm for acoustic waves in absorptive media. IEEE Transactions on Ultrasonics Ferroelectrics and Frequency Control 1998; 45: 1044-1055.

64. Berenger JP. A perfectly matched layer for the absorption of electromagnetic waves. Journal of Computational Physics 1994; 114(2): 185 - 200.

65. Liu QH. PML and PSTD algorithm for arbitrary lossy anisotropic media. IEEE Microwave and Guided Wave Letters 1999; 9(2):48-50.

66. Kreiss H.-O. and Oliger J., Comparison of accurate methods for the integration of hyperbolic equations. Tellus 1972; 24:199-215.

67. Liu QH. The PSTD algorithm: a time-domain method requiring only two cells per wavelength. Microwave and Optical Technology Letters 1997; 15(3): 158-165.

68. Orszag S.A. Comparison of pseudospectral and spectral approximation. Stud. Appl. Math. 1972; 51: 253-259.

69. Canuto C., Hussani M. Y., Quarteroni A. and Zang T. Spectral Methods in Fluid Dynamics. New York: Springer-Verlag 1988.

70. Bojarski N.N. The k-space formulation of the scattering problem in the time domain. J. Acoust. Soc. Amer. 1982; 72: 570-584

71. Liu Q.H. Transient electromagnetic modeling with the generalized k-space (GKS) method. Microwave Opt. Tech. Lett. 1994; 7 (18): 842-848.

72. Cooley J.W. and Tukey J.W. Algorithm for the machine computation of complex Fourier series. Math. Comput. 1965; 19: 297-301.

73. Tian B., Liu QH. Nonuniform fast cosine transform and Chebyshev PSTD algorithm. Progress in Electromagnetics Research 2000; 28:259-279

74. Yang B., Gottlieb D., and Hesthaven JS., Spectral simulation of electromagnetic wave scattering. Journal of Computational Physics 1997; 134(2):216-230

75. Hesthaven JS. Spectral collocation time-domain modeling of diffractive optical elements. Journal of Computational Physics 1999; 155(2):287–306.

76. Yang B, Hesthaven JS. A pseudospectral method for time-domain computation of electromagnetic scattering by bodies of revolution. IEEE Transactions on Antennas and Propagation 1999; 47(1):132–141.

77. Yang B, Hesthaven JS. Multidomain pseudospectral computation of Maxwell's equations in 3-D general curvilinear coordinates. Applied Numerical Mathematics 2000; 33(1–4): 281–289.

78. Zhai P.W., Lee Y.K., Kattawar G.W., Yang P. Implementing the near- to far-field transformation in the finite-difference time-domain method. Applied Optics 2004; 43:3738-3746.

79. Gao X., Mirotznik M.S., Prather D.W. A method for introducing soft sources in the PSTD algorithm. IEEE Transactions on Antennas and Propagation 2004; 52(7): 1665-1671.

80. Taflove A., Brodwin M.E. Numerical solution of steady-state electromagnetic scattering problems using the time-dependent Maxwell's equations. IEEE Trans. Microwave Theory Tech. 1975; MTT-23:623-630.

81. Berenger J. P. Three-dimensional perfectly matched layer for the absorption of electromagnetic waves. Journal of Computational Physics 1996; 127(2): 363-379.

82. Sacks Z.S., Kingsland D.M., Lee R., Lee J.F. A perfectly matched anisotropic absorber for use as an absorbing boundary condition. IEEE Transactions on Antennas and Propagation 1995; 43 (12): 1460-1463

83. Taflove A. and Hagness S.C. Computational Electrodynamics: The Finite-Difference Time-domain Method. Boston: Artech House, 2005.

84. Heymsfield A.J. and Iaquinta J. Cirrus crystal terminal velocities. J. Atmos. Sci. 2000; 5: 916-938.

85. Auer A.H. and Veal D.L. The dimension of ice crystals in natural clouds, J. Atmos. Sci. 1970; 27: 919-926.

86. Pruppacher H.P. and Klett J.D. Microphysics of clouds and precipitation. D. Reidel, Norwell, Mass., 1980: 714.

87. Heymsfield A.J. and Miloshevich L.M. Parameterization for the cross-sectional area and extinction of cirrus and stratiform ice cloud particles. J. Atmos. Sci. 2002; 60: 936-956.

88. Greenler R.G. Rainbow, Halos, and Glories. New York: Cambridge Univ. Press, 1980.

89. Donner, L., Seman CJ., Sden B.J., Hemler RS., Warren JC., Strom J., and

Liou KN. Large-scale ice clouds in the GFDL SKYHI general circulation model. J. Geophys. Res. 1997;102:21745-21768.

90.   Liou K.N. and Takano Y. Light scattering by nonspherical particles: remote sensing and climatic implications. Atmos. Res. 1994; 31: 271-298.

91.   Liou KN. Influence of cirrus clouds on weather and climate processes: a global perspective. Mon. Weather Rev. 1986;114:1167-1199.

92.   Hartmann DL., Ockert-Bell ME., and Michelsen ML. The effect of cloud type on earth's energy balance: global analysis. J. Clim. 1992; 5:1281-1304.

93.   Hobbs PV. Ice Physics. London: Oxford U. P. 1974.

94.   Platt CMR. Lidar backscatter from horizontal ice crystal patterns. J. Appl. Meterol. 1978;17:482-488.

95.   Stephens GL. Radiative transfer on a linear lattice: application to anisotropic ice crystal clouds. J. Atmos. Sci. 1980;37:2095-2104.

96.   Rockwitz KD. Scattering properties of horizontally oriented ice crystal columns in cirrus clouds. Part 1. Appl. Opt. 1989;28:4103-4110.

97.   Lee YK., Yang P., Mishchchenko MI., Baum BA., Hu Y., Huang H-L., Wiscombe WJ., and Baran AJ. On the use of circular cylinders as surrogates for hexagonal pristine ice crystals in scattering calculations at infrared wavelengths. Appl. Opt. 2003;42:2653-2664.

98.   Warren S. Optical constants of ice from the ultraviolet to the microwave. Appl. Opt. 1984; 23:1206-1225.

99.   Mishchenko MI., Travis LD., and Lacis AA. Scattering, Absorption, and Emission

of Light by Small Particles. Cambridge: Cambridge University Press, 2002.

100. Born CF. and Huffman DR. Absorption and Scattering of Light by Small Particles. New York: John and Wiley &Sons, 1983.

101. Baran AJ., P. Yang, and Havemann S. Calculation of the single-scattering properties of randomly oriented hexagonal ice columns: a comparison of the T-matrix and the finite-difference time-domain methods. Appl. Opt. 2001;40: 4376-4386.

APPENDIX
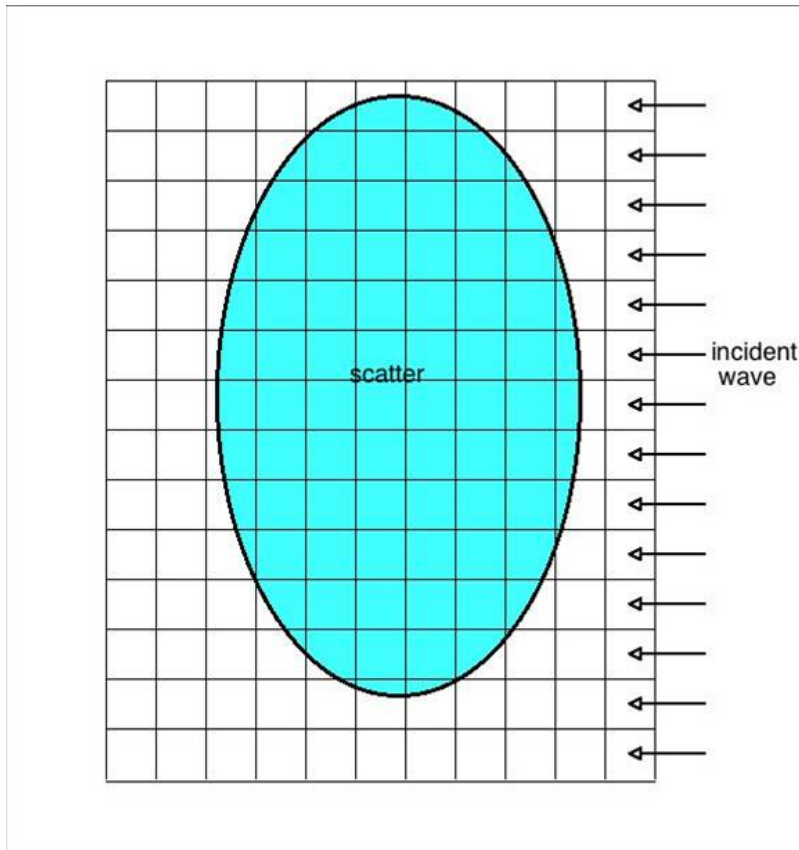
Fig. A.1 Conceptual diagram for the near field computation by the PSTD method.
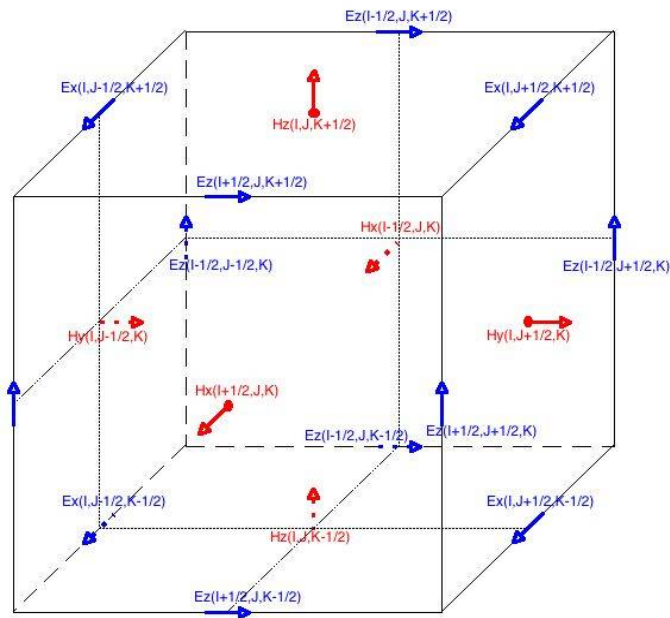
(a)
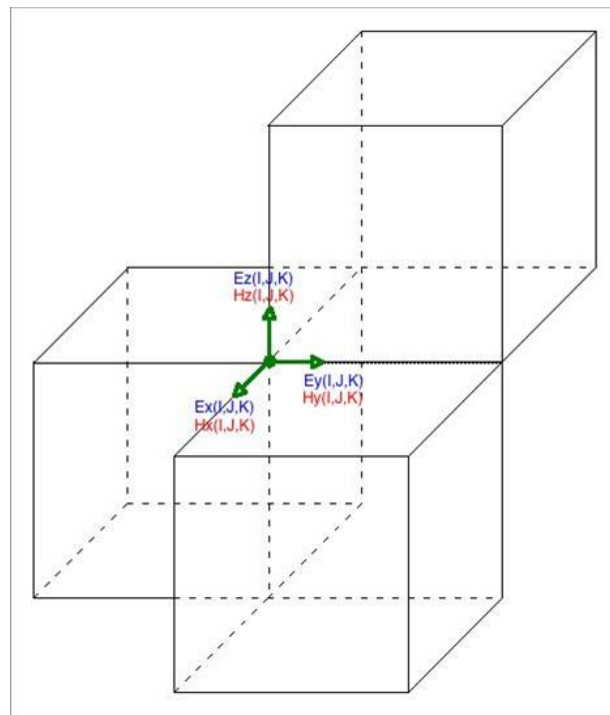
(b)

Fig. A.2 Field components locations on a grid cell.
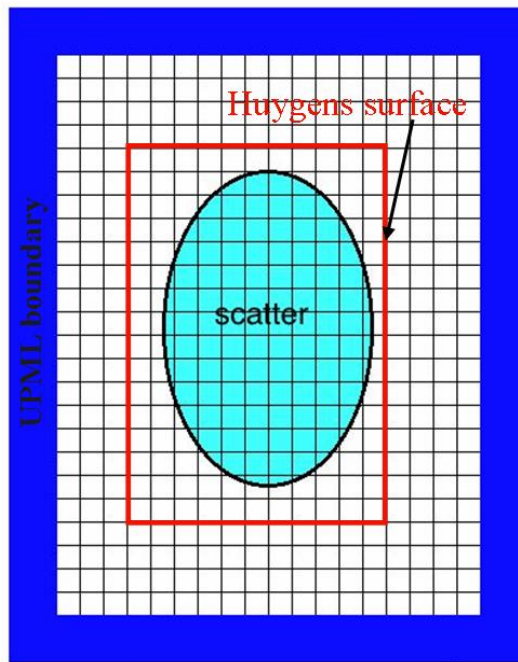
(a)
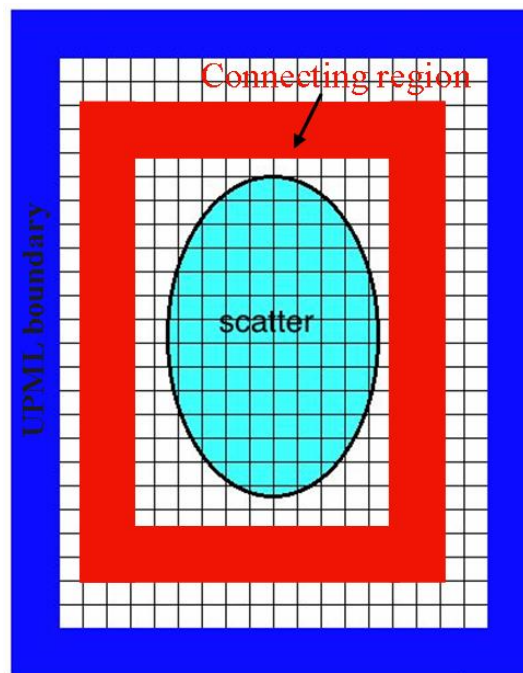
(b)

Fig. A.3 Conceptual diagram for the TF/SF technique
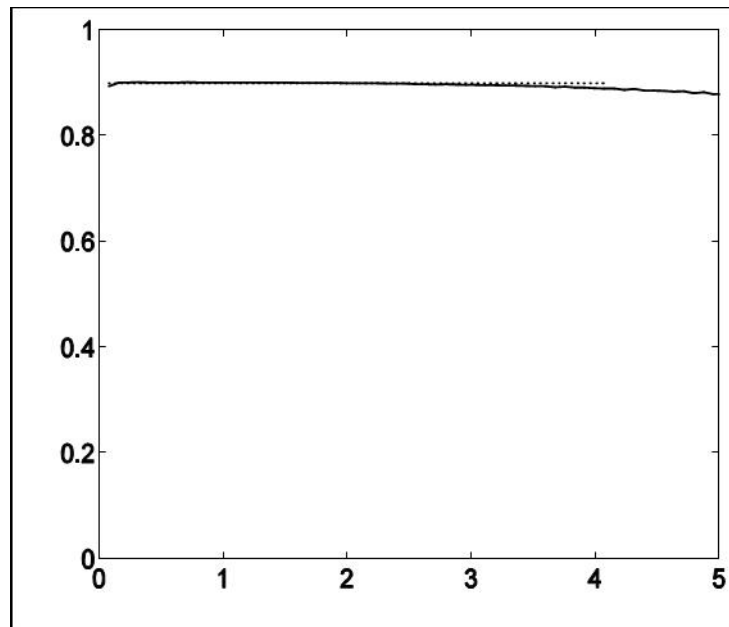
Fig. A.4 The transmission coefficients on a dielectric surface.
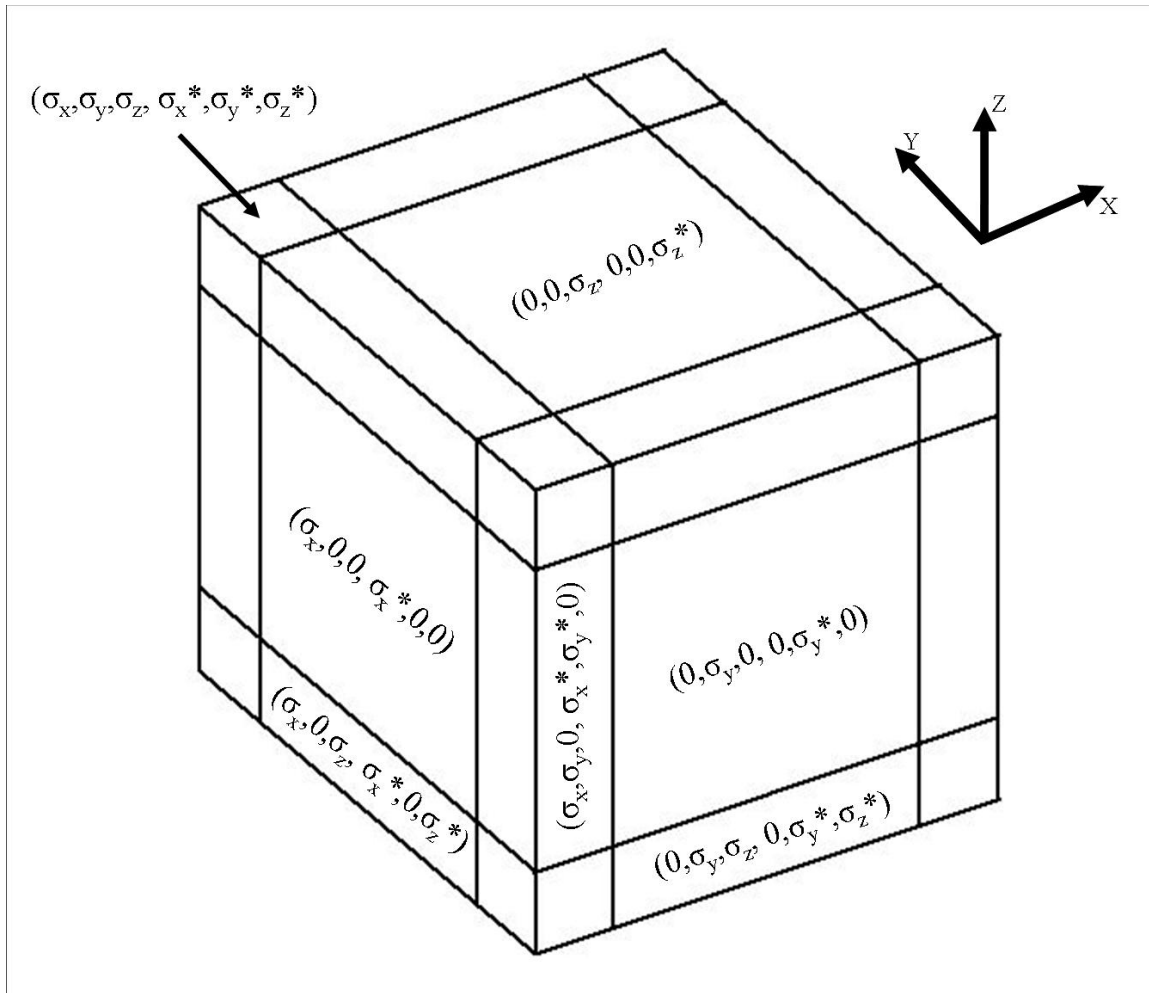
Fig. A.5 Conceptual diagram of the PML boundary applied to the PSTD method.
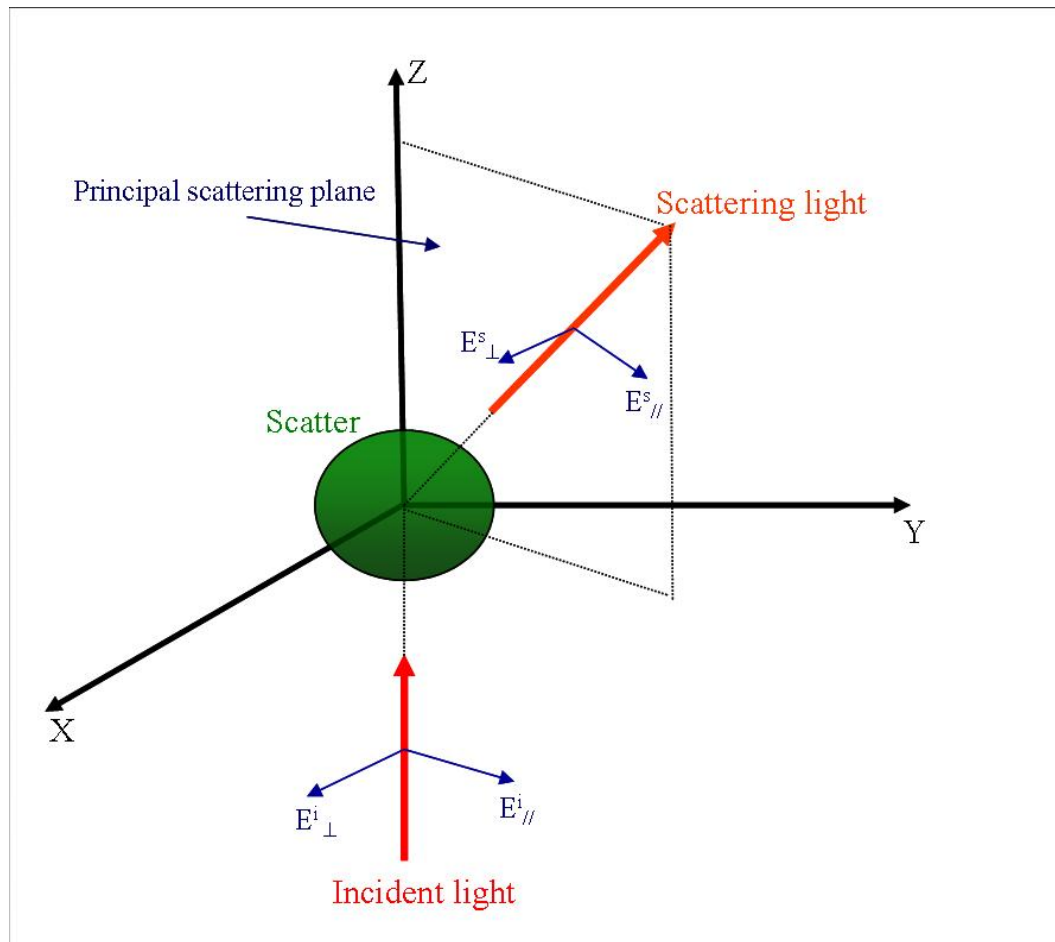
Fig. A.6 Incident and scattering light geometry.

(a)

(b)

(c)
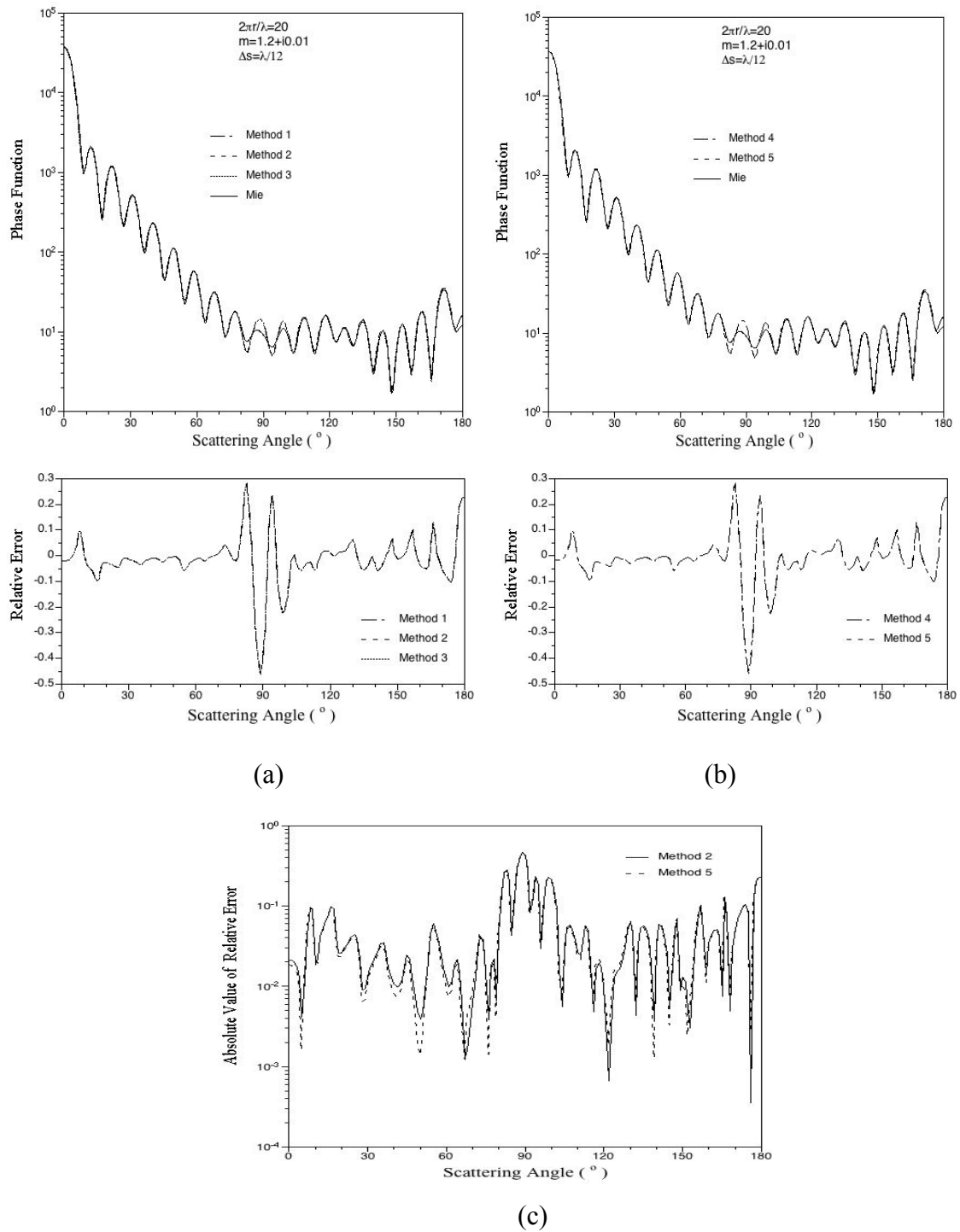
Fig. A.7. Comparison of phase functions for a sphere computed based on the five discretization schemes at refractive index 1.2+0.01j and size parameter 20.
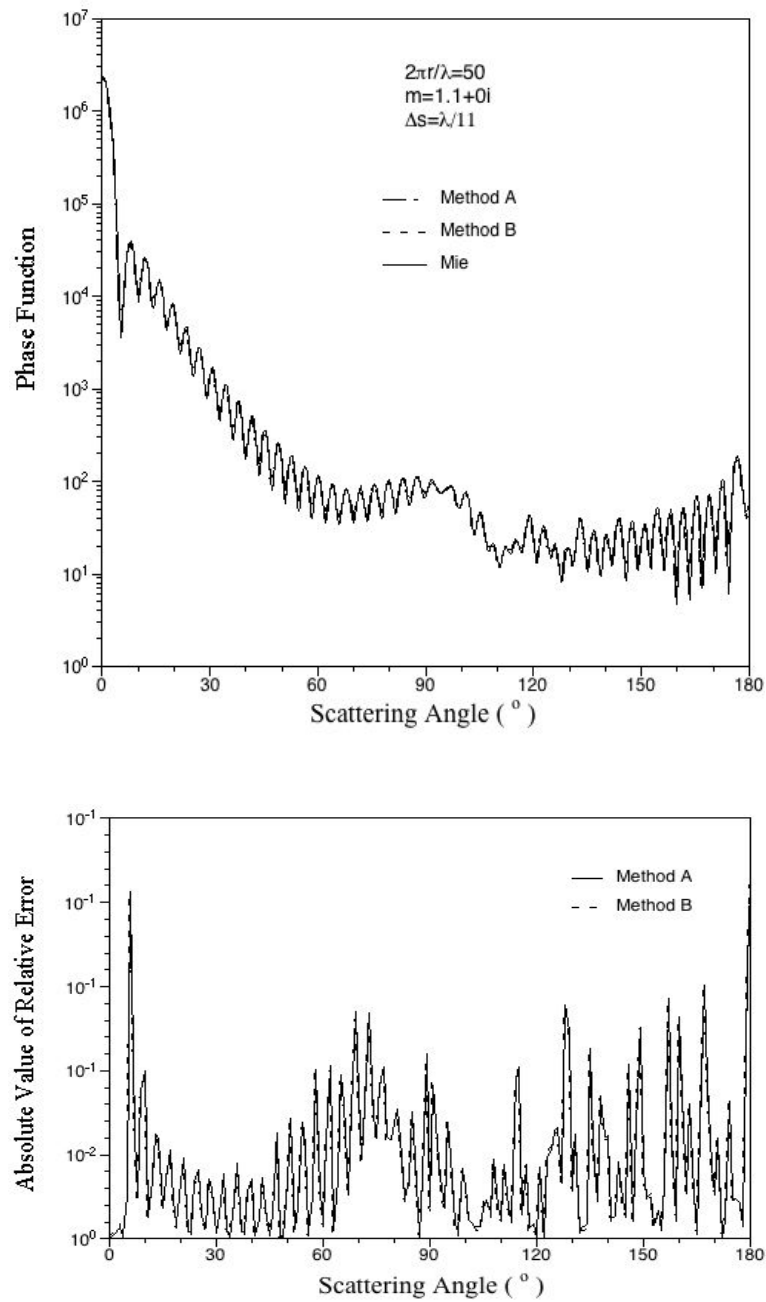
Fig. A.8. Comparison of phase functions for a sphere computed based on two different discretization methods at refractive index 1.1+0j and size parameter 50.

(a)   (b)

(c)   (d)
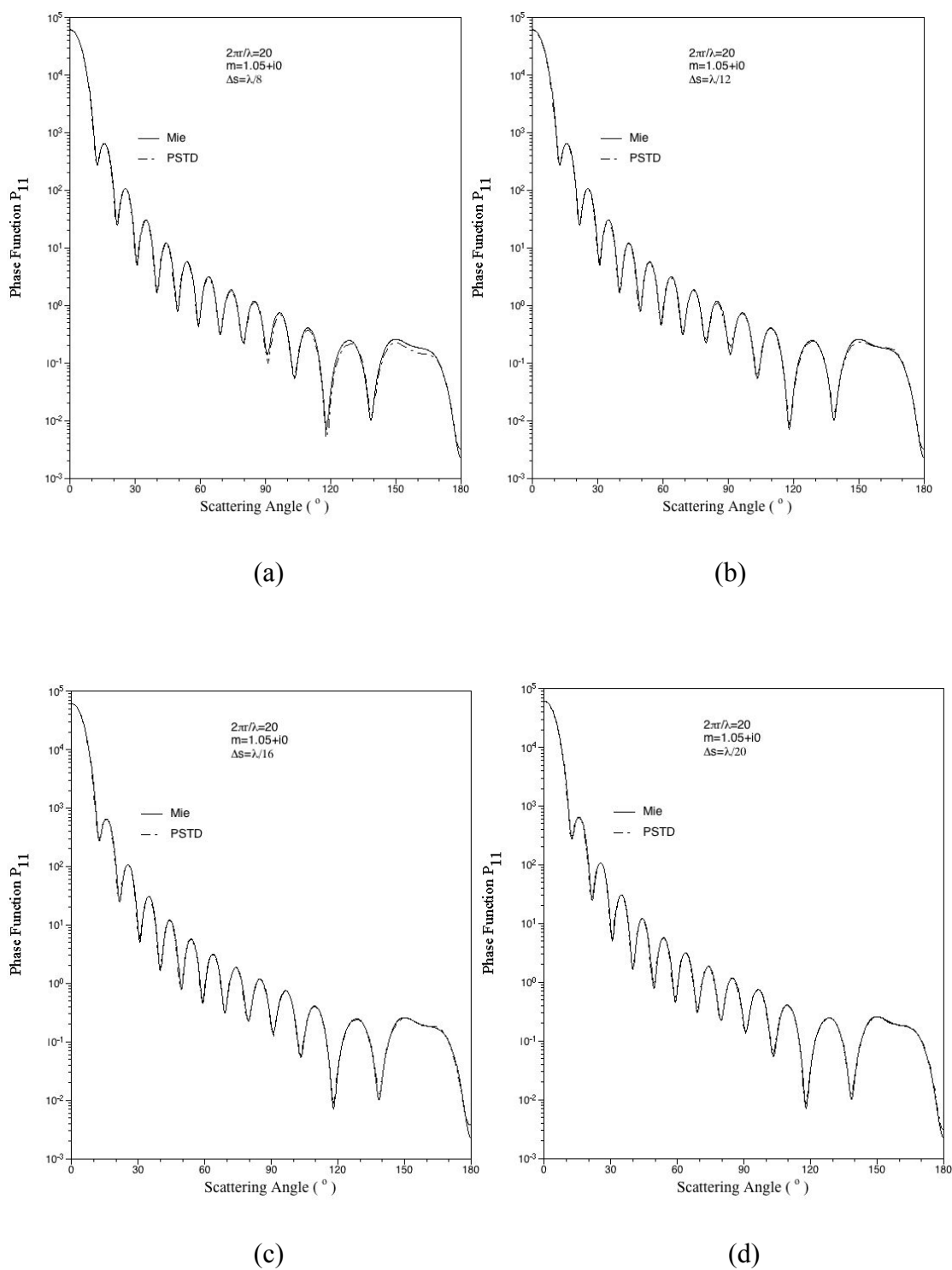
Fig. A.9. Comparison of phase functions for a sphere with various grid spatial resolutions at refractive index 1.05+0j and size parameter 20.

(a)

(b)

(c)

(d)
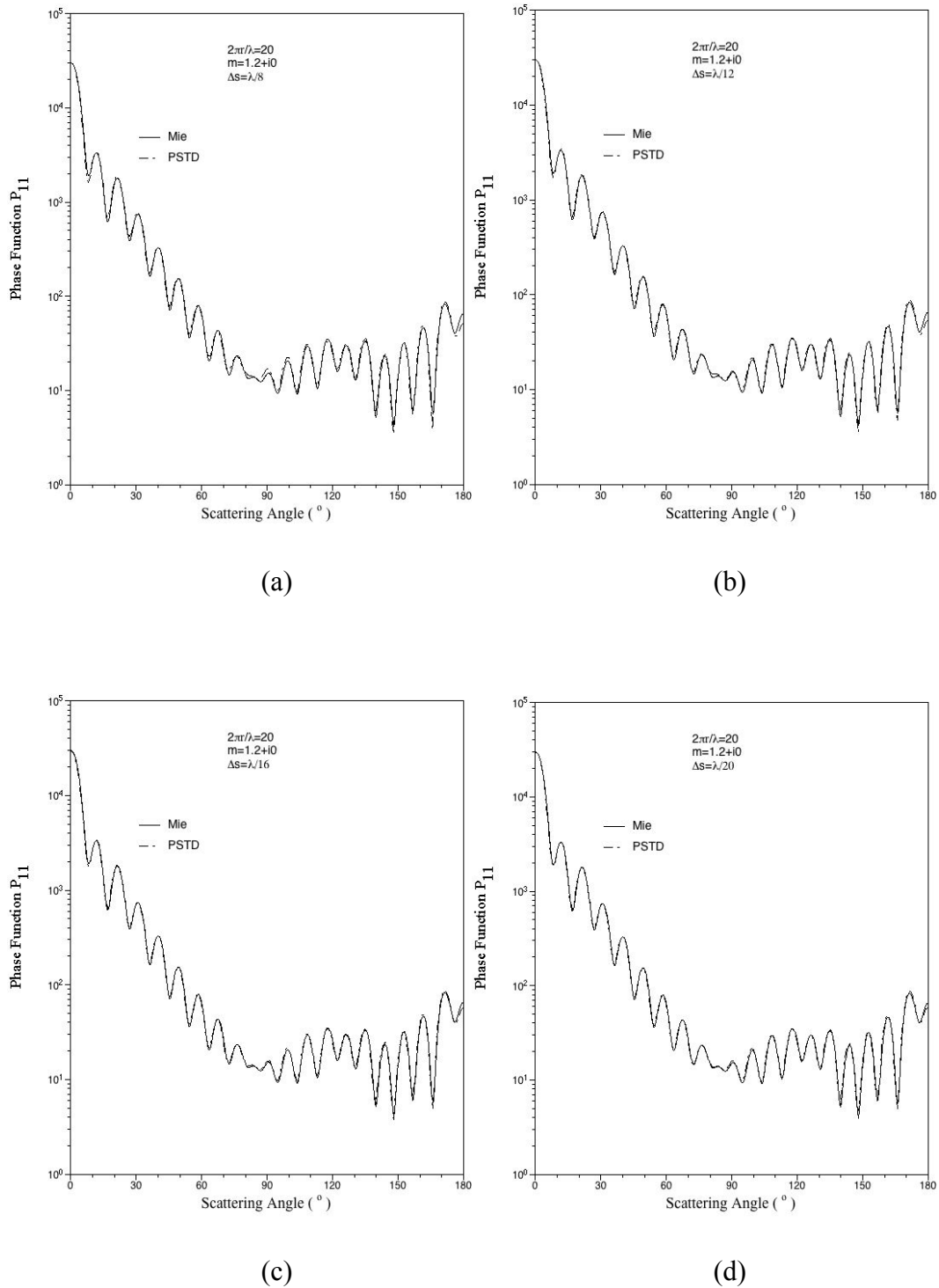
Fig. A.10. Comparison of phase functions for a sphere with various grid spatial resolutions at refractive index 1.2+0j and size parameter 20.
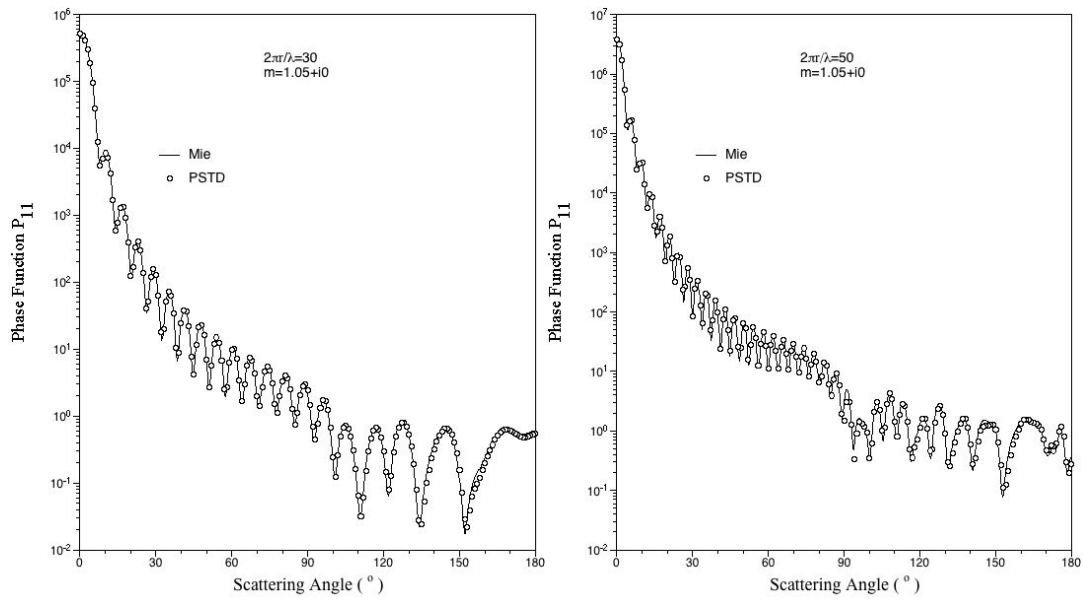
Fig. A.11. Comparison of PSTD and Mie solutions in terms of phase functions at refractive index 1.05+0j and spatial resolution 10. Size parameters are 30 and 50, respectively.
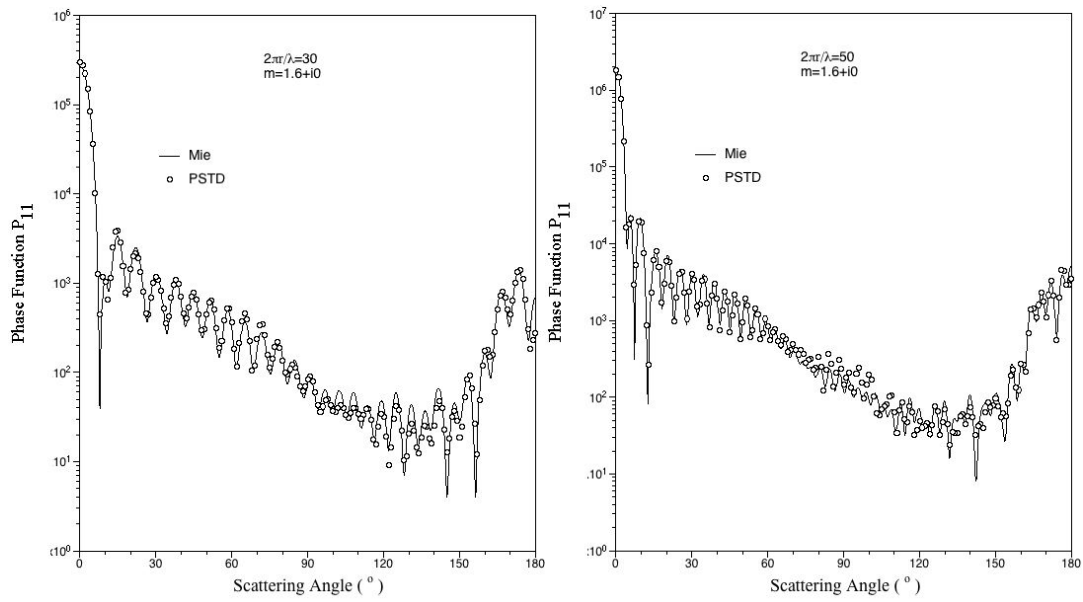
Fig. A.12. Comparison of PSTD and Mie solutions in terms of phase functions at refractive index 1.6+0j and spatial resolution 16. Size parameter is 30 and 50, respectively.
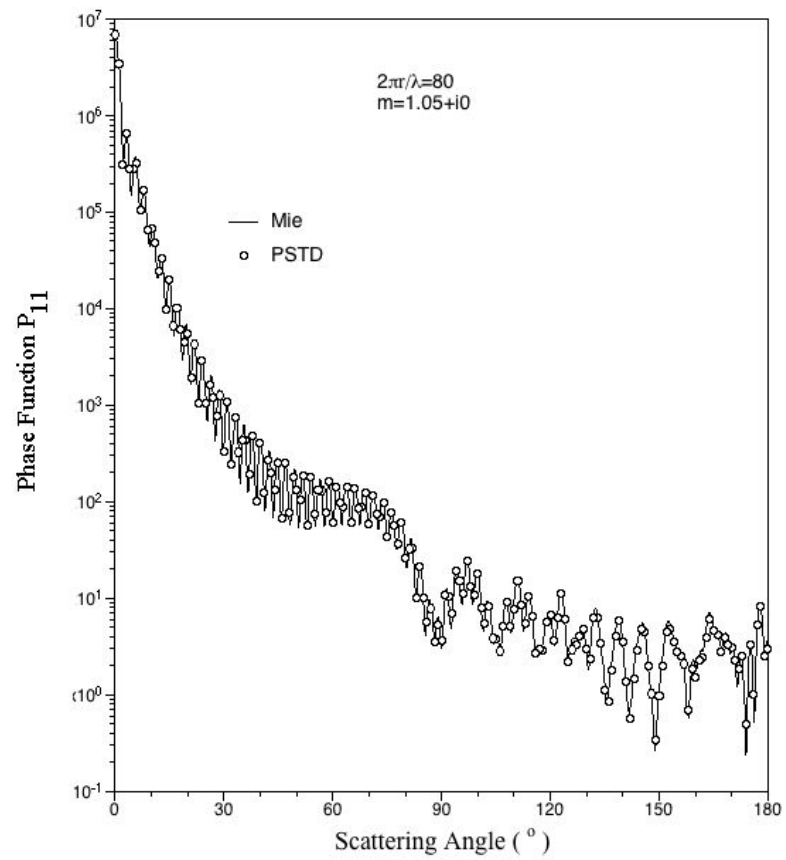
Fig. A.13. Comparison of PSTD and Mie solutions in terms of phase functions at size parameter 80, refractive index 1.05+0j and spatial resolution 8.
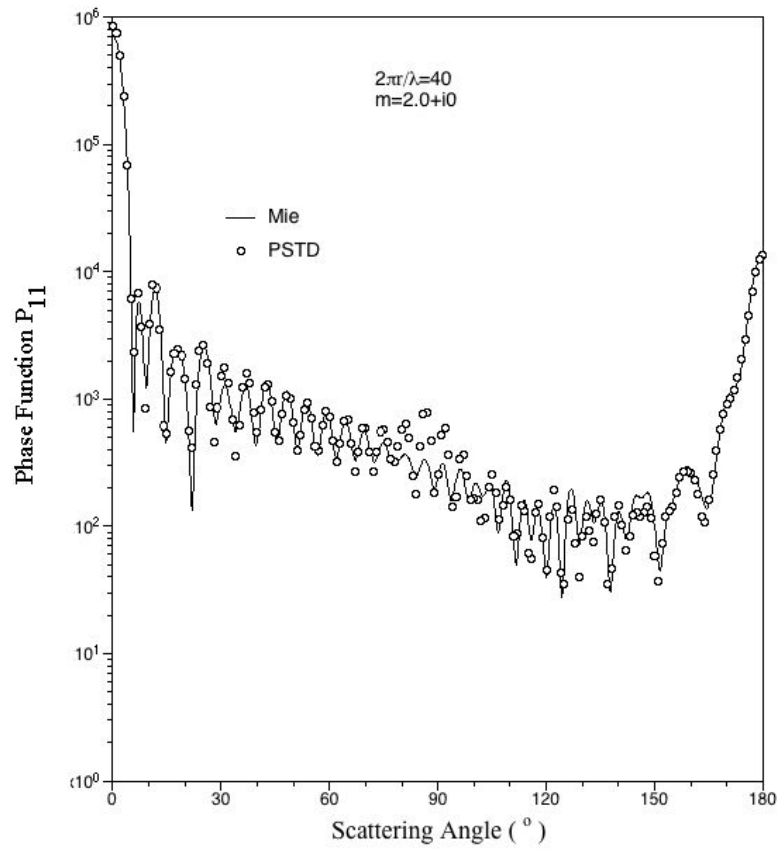
Fig. A.14 Comparison of the PSTD and Mie solutions in terms of phase functions at size parameter 40, refractive index 2.0+0j and spatial resolution 18.
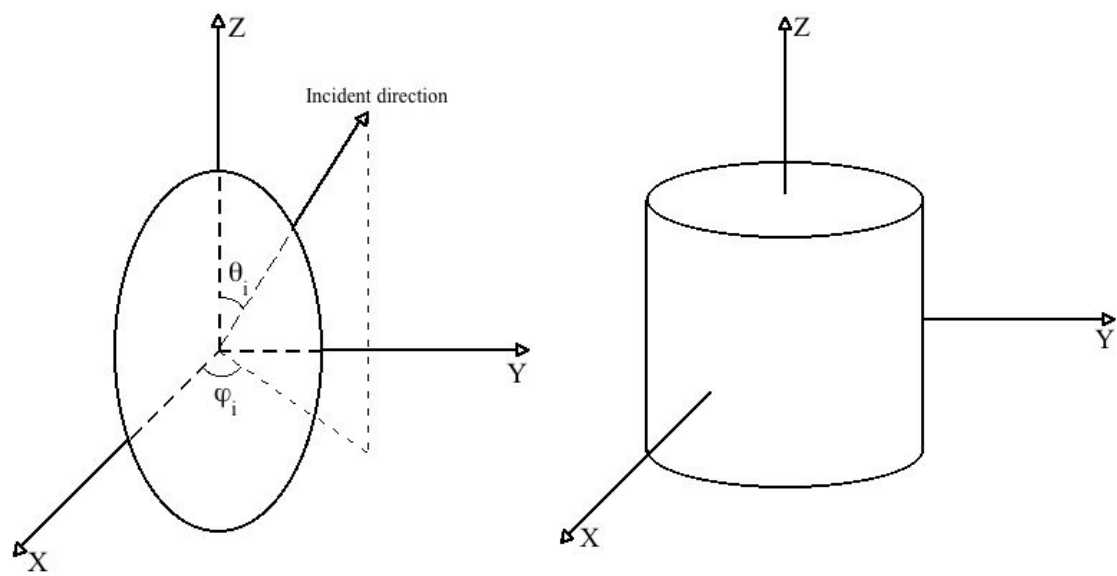
Fig. A.15. Orientations of spheroid and circular cylinder in the laboratory coordinate.
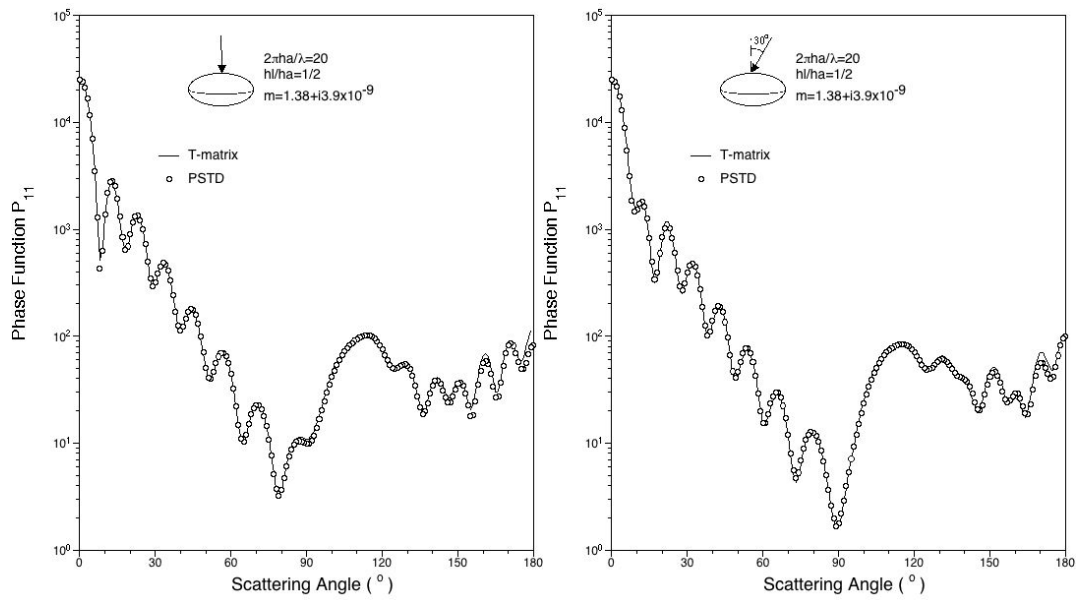
Fig. A.16 Comparison of PSTD and T-matrix solutions in terms of phase functions for an oblate spheroid with aspect ratio 0.5 and size parameter 20.
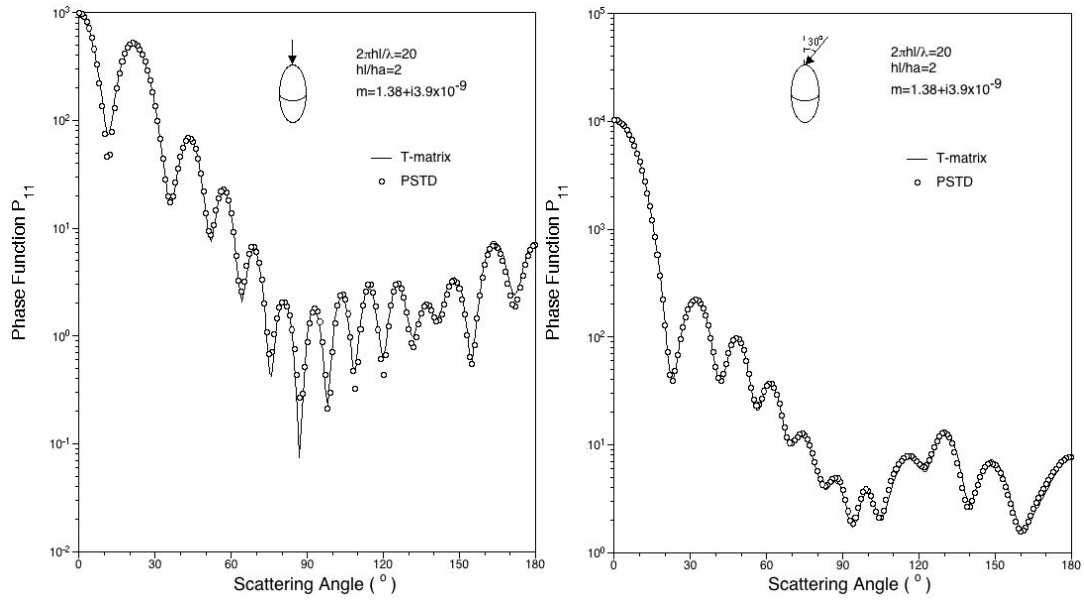
Fig. A.17. Comparison of PSTD and T-matrix solutions in terms of phase functions for an oblate spheroid with aspect ratio 2 and size parameter 20.
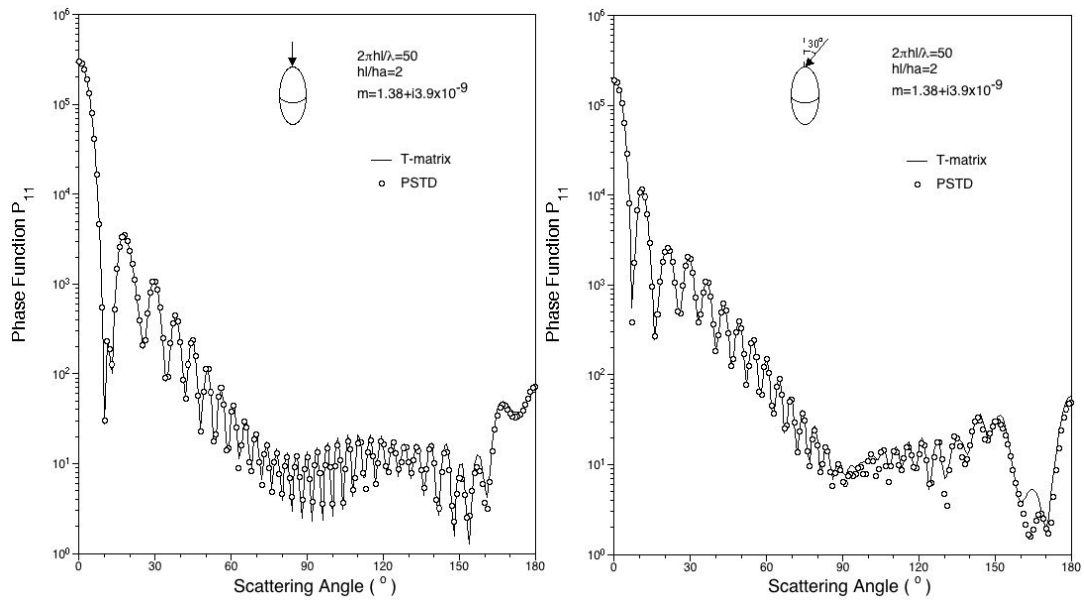
Fig. A.18. Comparison of PSTD and T-matrix solutions in terms of phase functions for an oblate spheroid with aspect ratio 2 and size parameter 50.
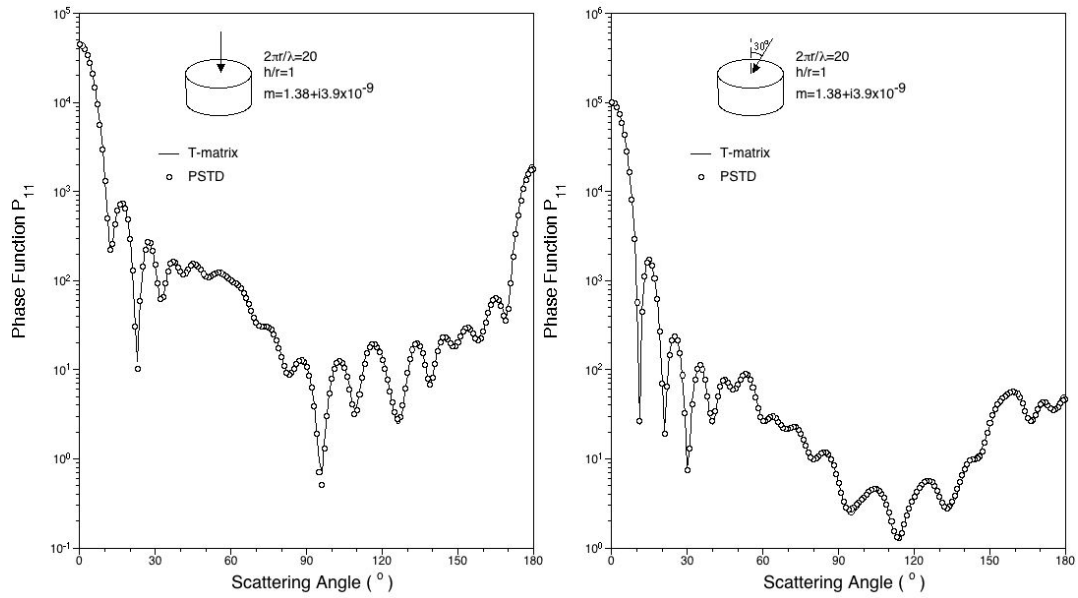
Fig. A.19. Comparison of PSTD and T-matrix solutions in terms of phase functions for circular cylinder with aspect ratio 1 and size parameter 20.
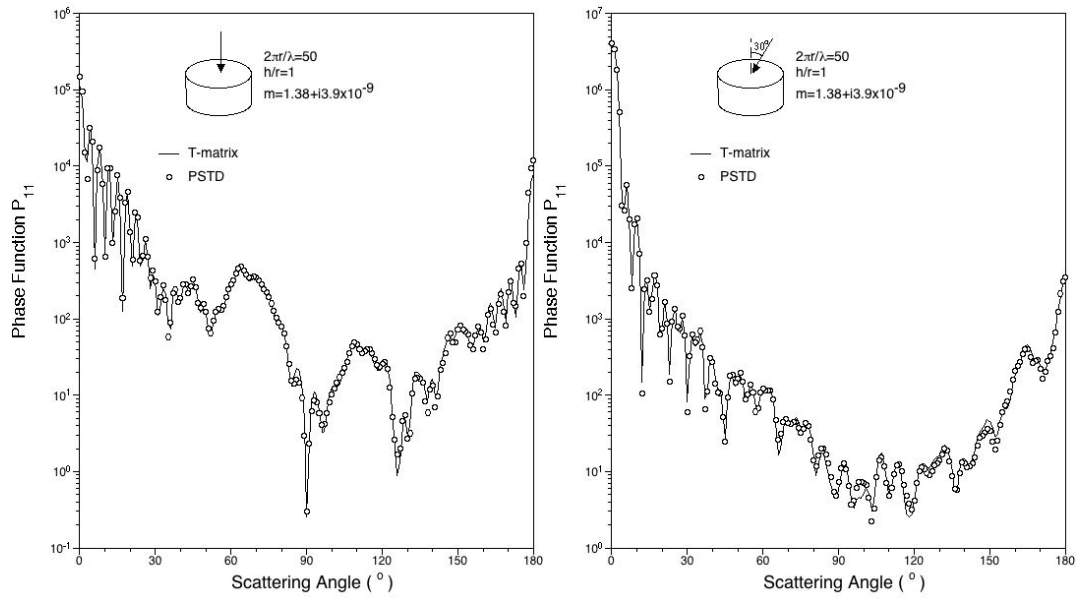
Fig. A.20. Comparison of PSTD and T-matrix solutions in terms of phase functions for circular cylinder with aspect ratio 1 and size parameter 50.
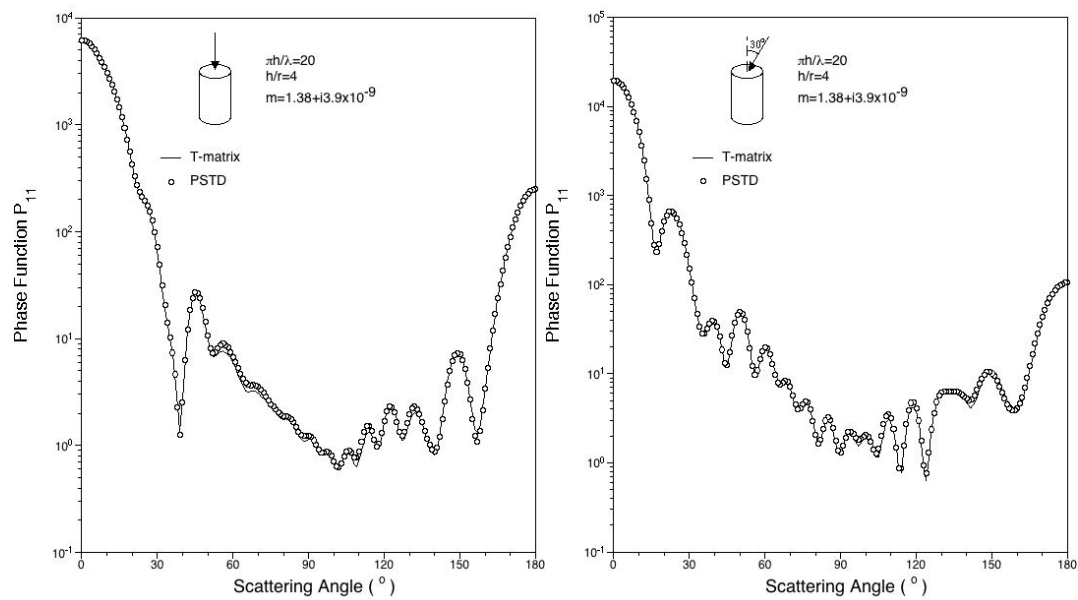
Fig. A.21. Comparison of PSTD and T-matrix solutions in terms of phase functions for circular cylinder with aspect ratio 4 and size parameter 20.
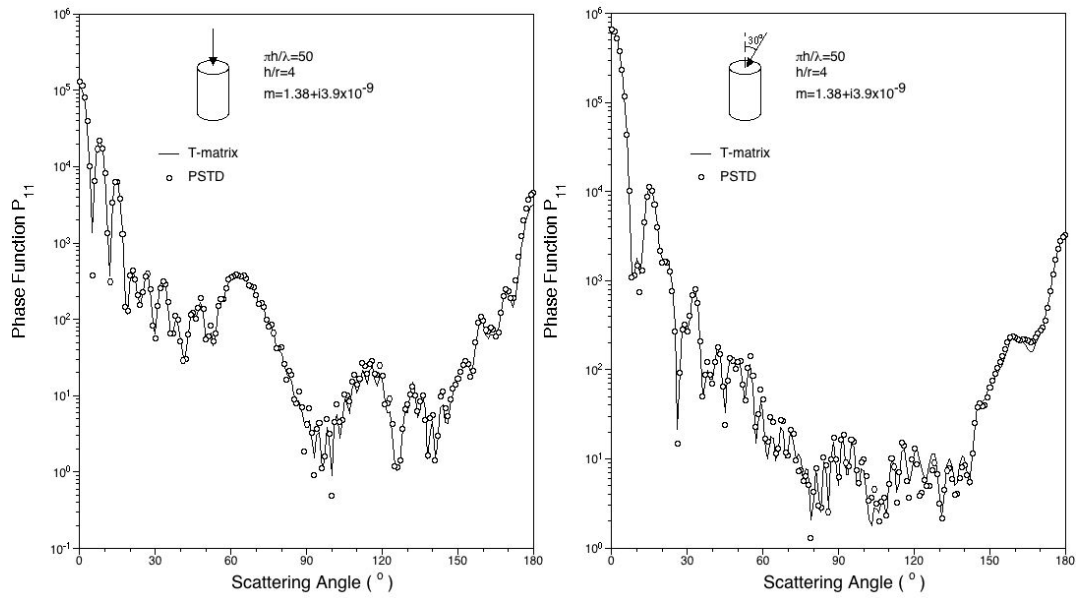
Fig. A.22. Comparison of PSTD and T-matrix solutions in terms of phase functions for circular cylinder with aspect ratio 4 and size parameter 50.
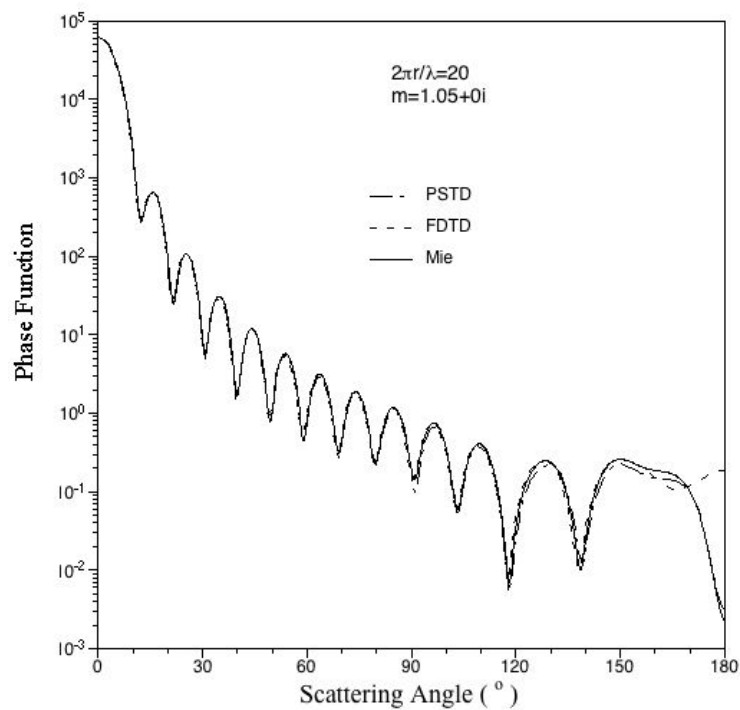
Fig. A.23. Comparison of PSTD, FDTD and Mie solutions in terms of phase functions for a sphere with refractive index 1.05+0j and size parameter 20.
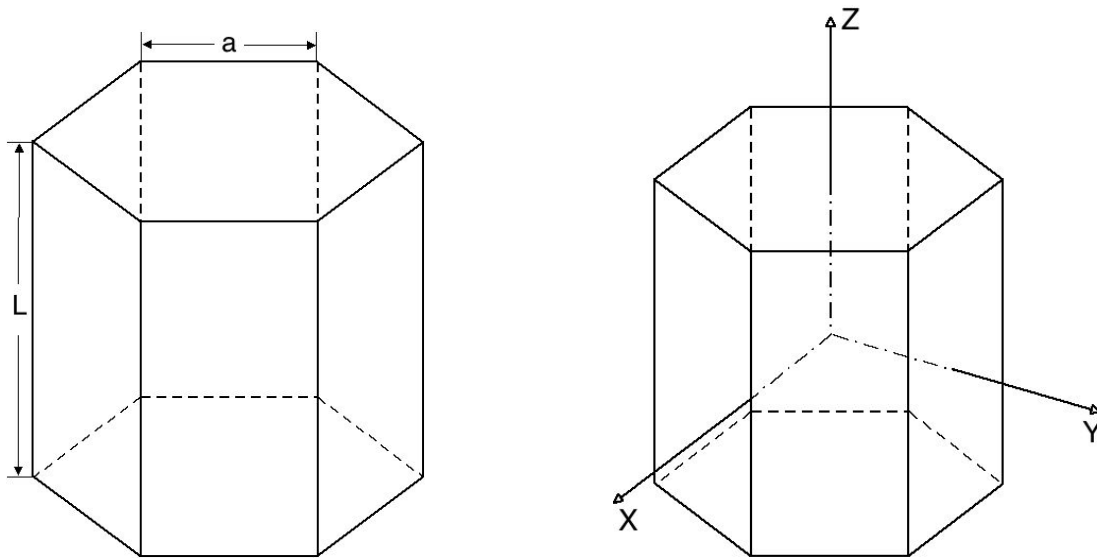
Fig. A.24. Geometry for hexagonal ice prism and its orientation in a laboratory coordinate.
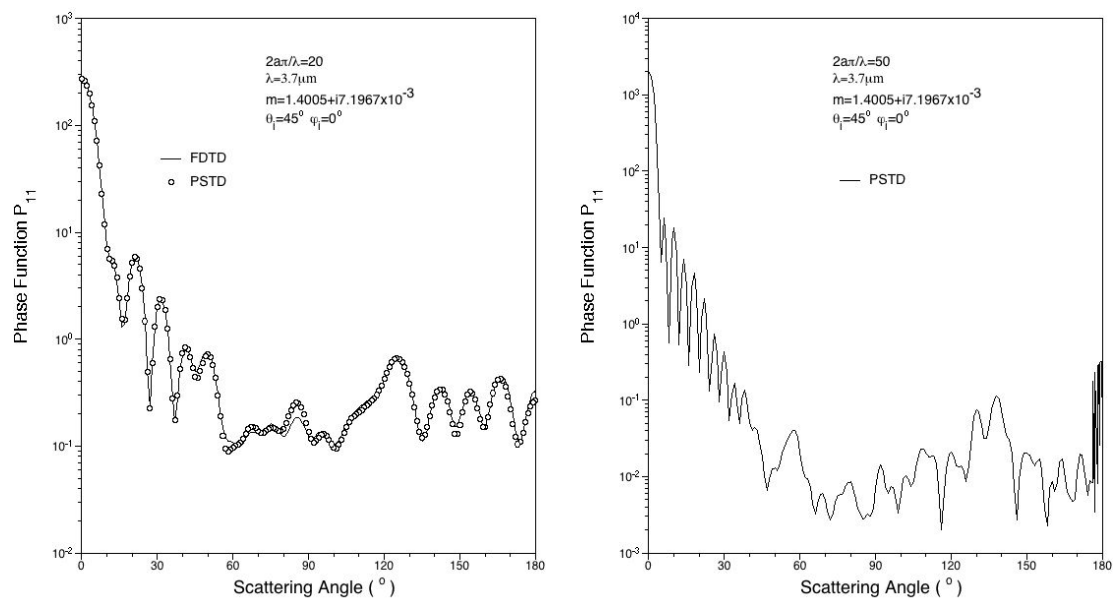
Fig. A.25. Phase functions of fix oriented hexagonal ice plate at incident wavelength of 3.7 μm where $\theta_i = 45°$, $\varphi_i = 0°$ and $\varphi_s = 0°$. Size parameters are 20 and 50.
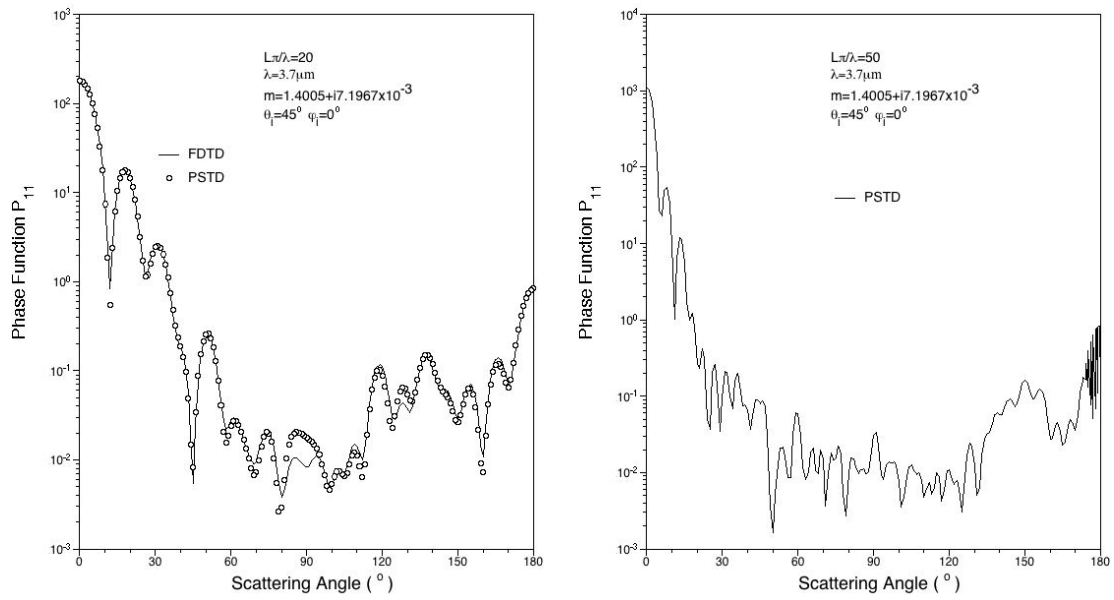
Fig. A.26 Phase functions of oriented hexagonal ice columns at incident wavelength of 3.7 µm where $\theta_i = 45°$, $\varphi_i = 0°$ and $\varphi_s = 0°$. Size parameters are 20 and 50.
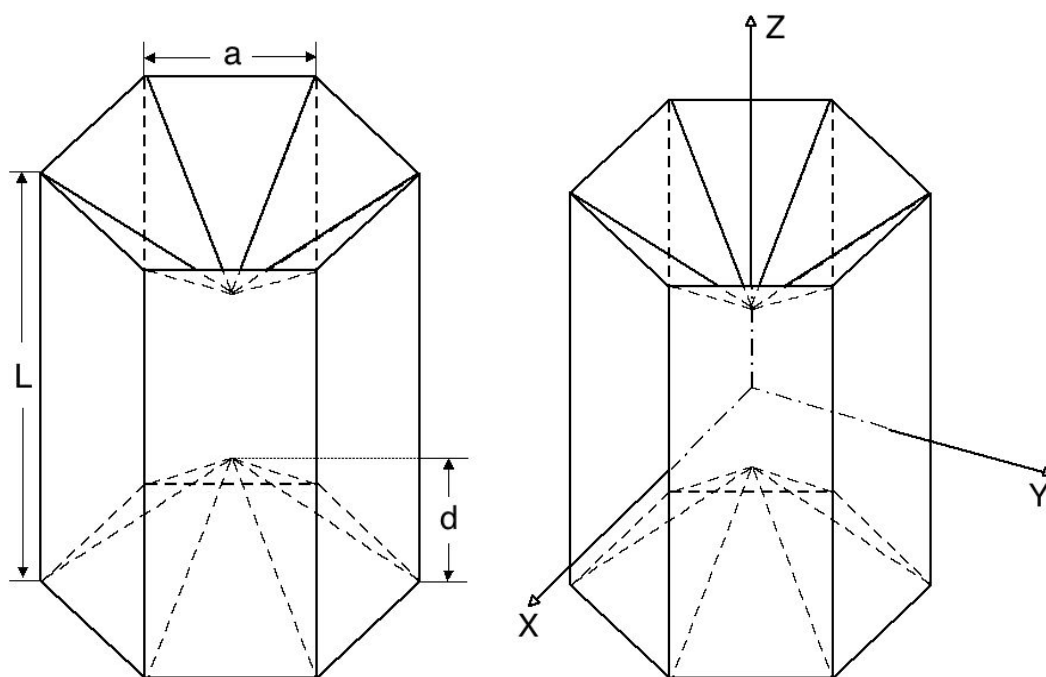
Fig. A.27. Geometry for a hollow hexagonal ice column and its orientation in a laboratory coordinate.
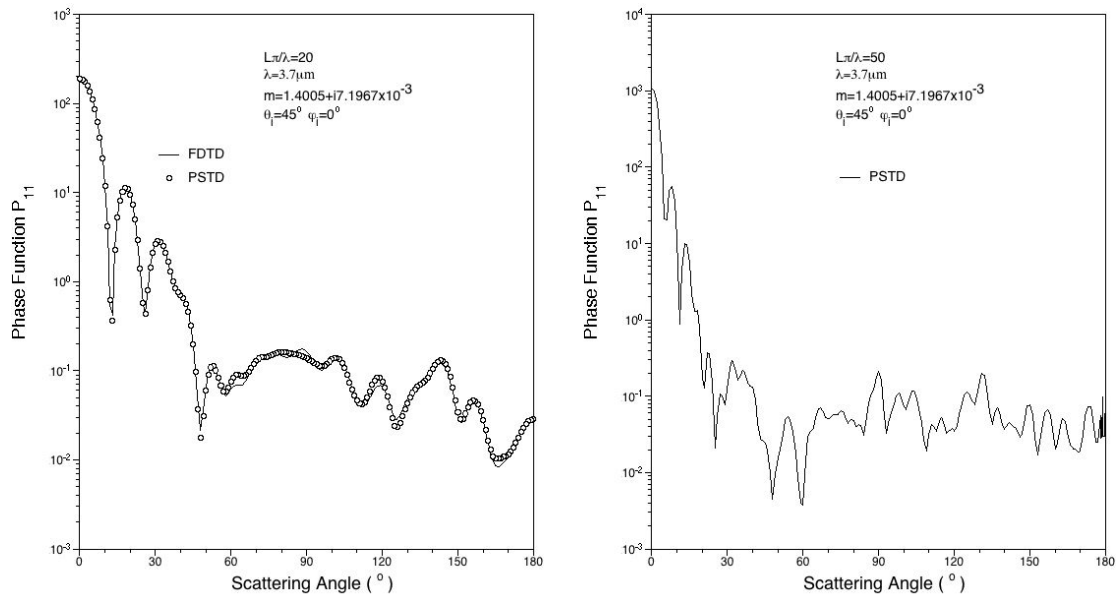
Fig. A.28. Phase functions of oriented hollow hexagonal ice column at incident wavelength of 3.7 μm where $\theta_i = 45°$, $\varphi_i = 0°$ and $\varphi_s = 0°$. Size parameters are 20 and 50.
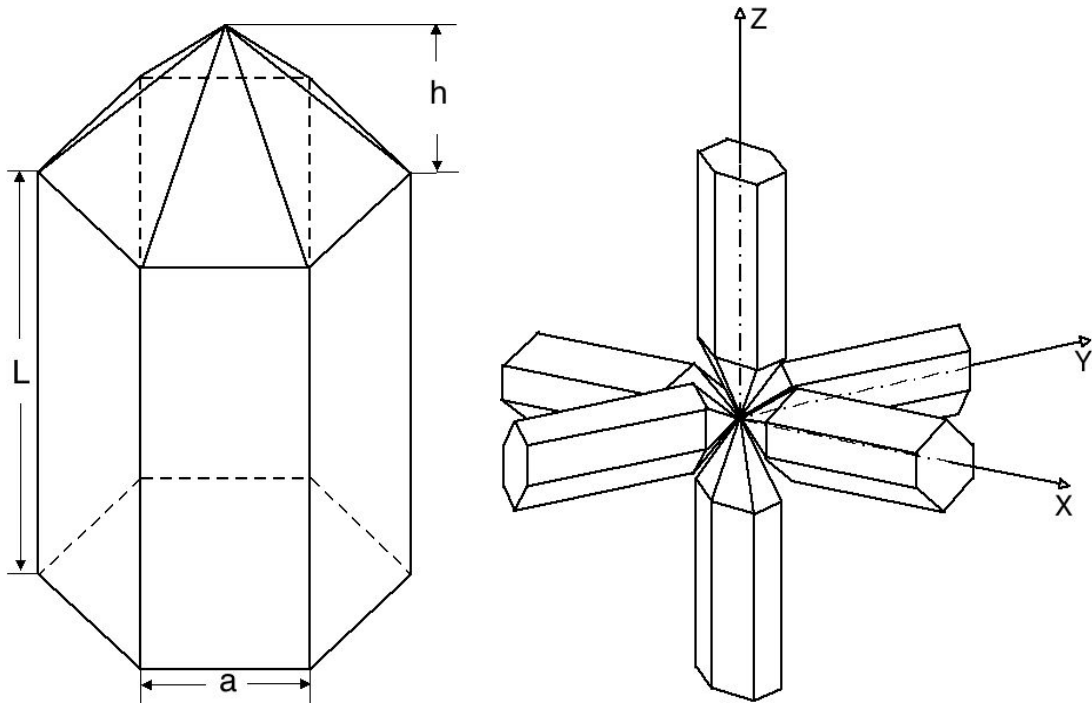
Fig. A.29. Geometry for a bullet and orientation of rosette in a laboratory coordinate.
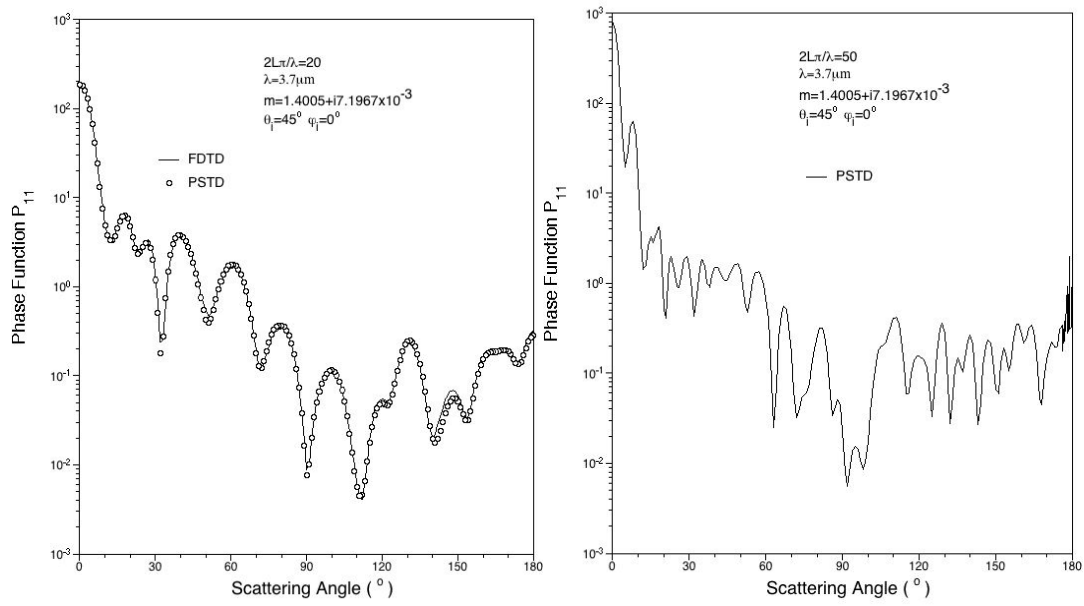
Fig. A.30. Phase functions of oriented ice bullet rosette at incident wavelength of 3.7 μm where $\theta_i = 45°$, $\varphi_i = 0°$, and $\varphi_s = 0°$. Size parameters are 20 and 50.
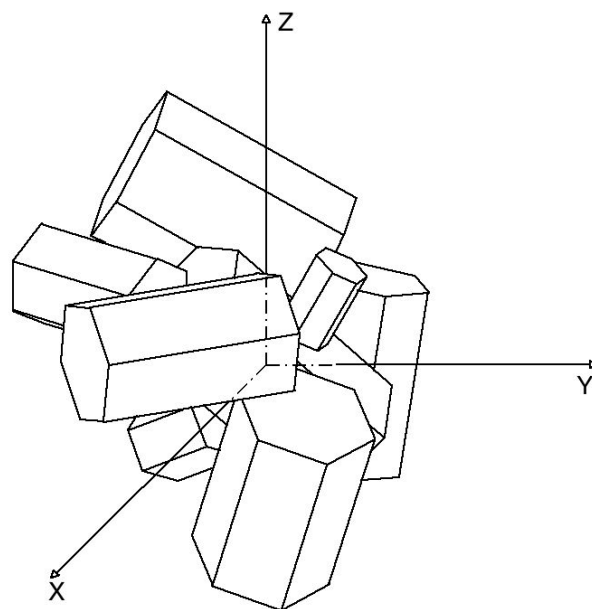
Fig. A.31. Geometry and orientation for an aggregate.
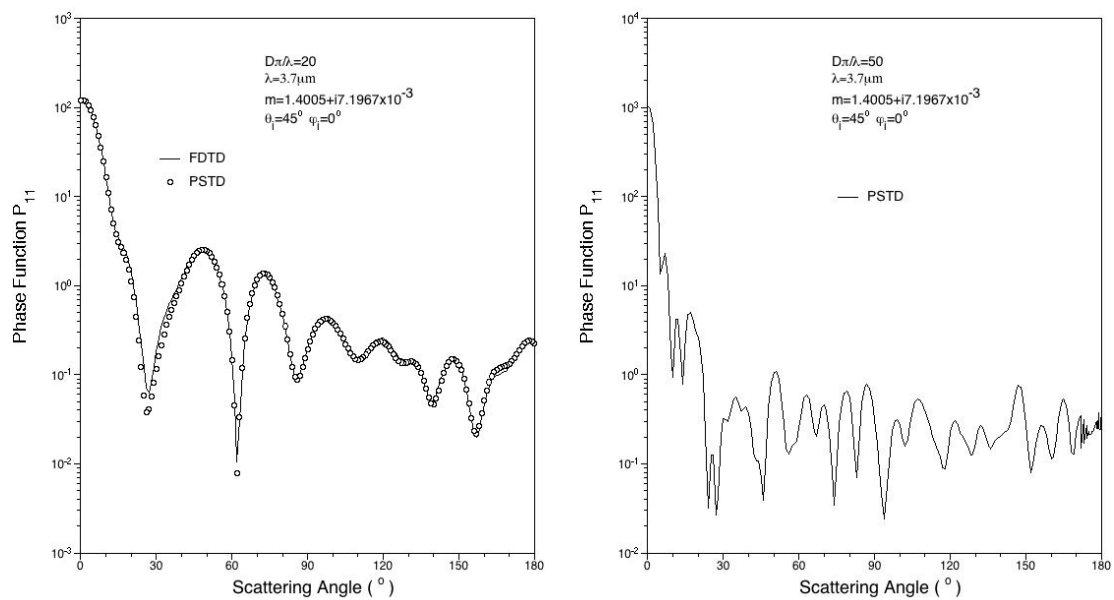
Fig. A.32. Phase functions of oriented ice aggregate at incident wavelength of 3.7 μm where $\theta_i = 45°$, $\varphi_i = 0°$ and $\varphi_s = 0°$. Size parameters are 20 and 50.
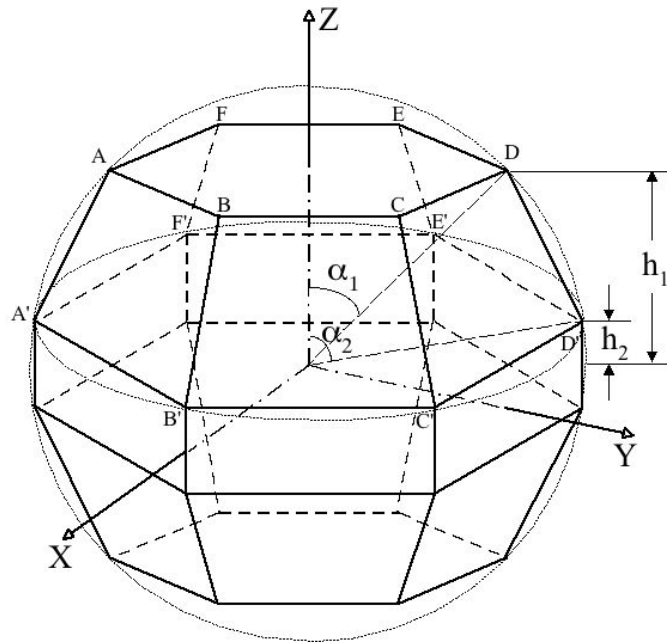
Fig. A.33. Geometry and orientation for a droxtal.
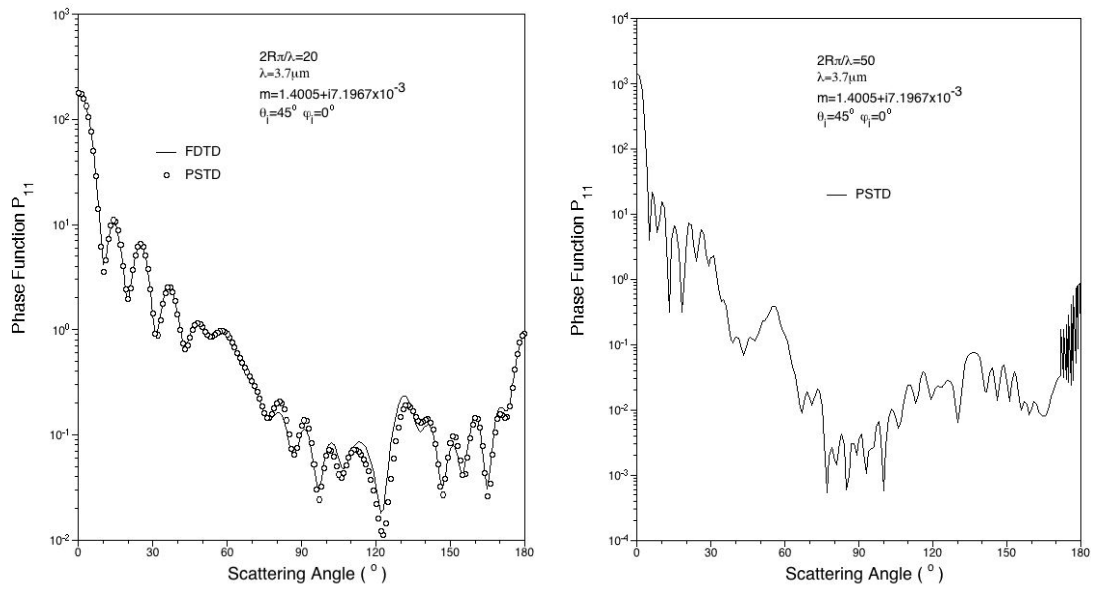
Fig. A.34. Phase functions of oriented ice droxtal at incident wavelength of 3.7 μm where $\theta_i = 45°$, $\varphi_i = 0°$ and $\varphi_s = 0°$. Size parameters are 20 and 50.
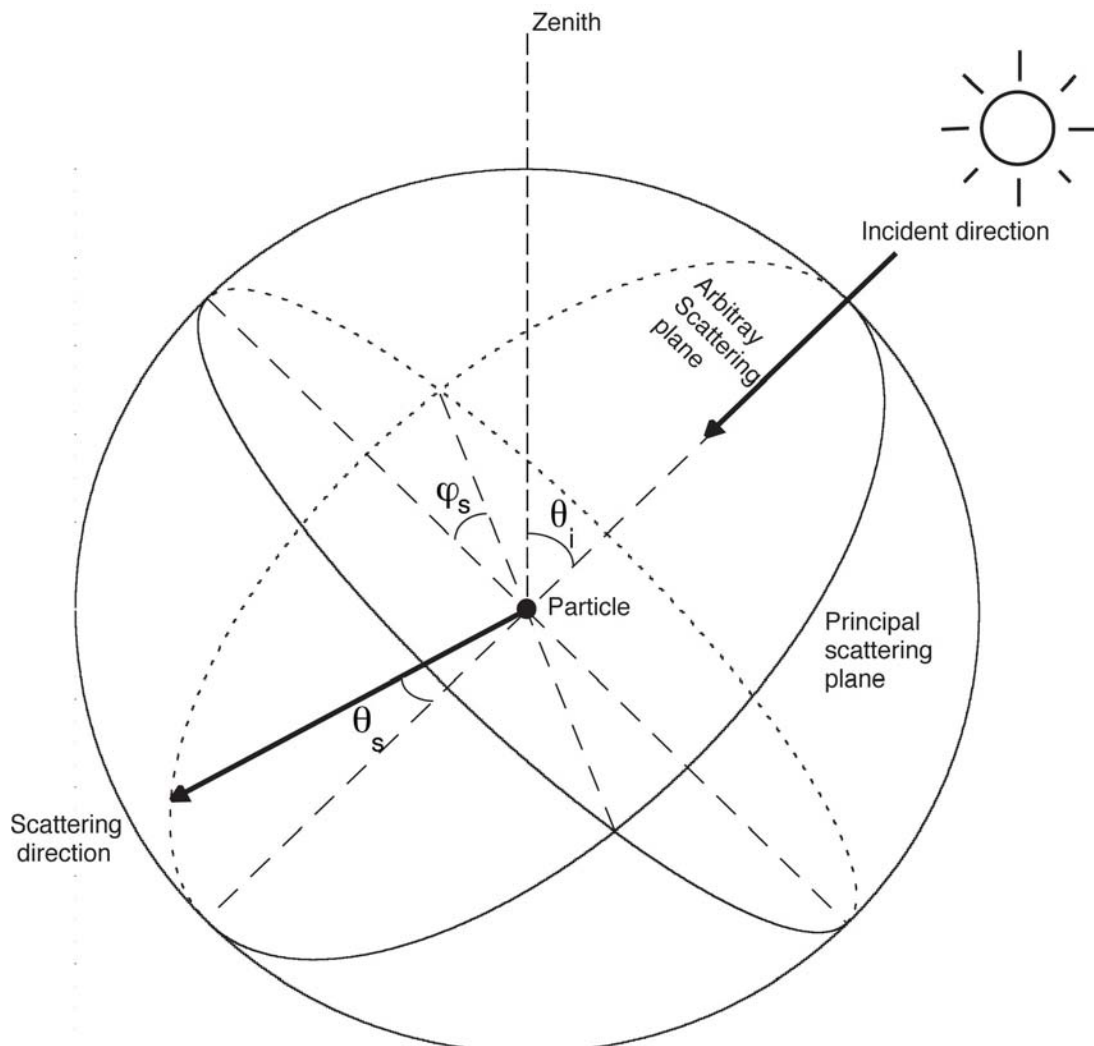
Fig. A.35. Incident scattering configuration.
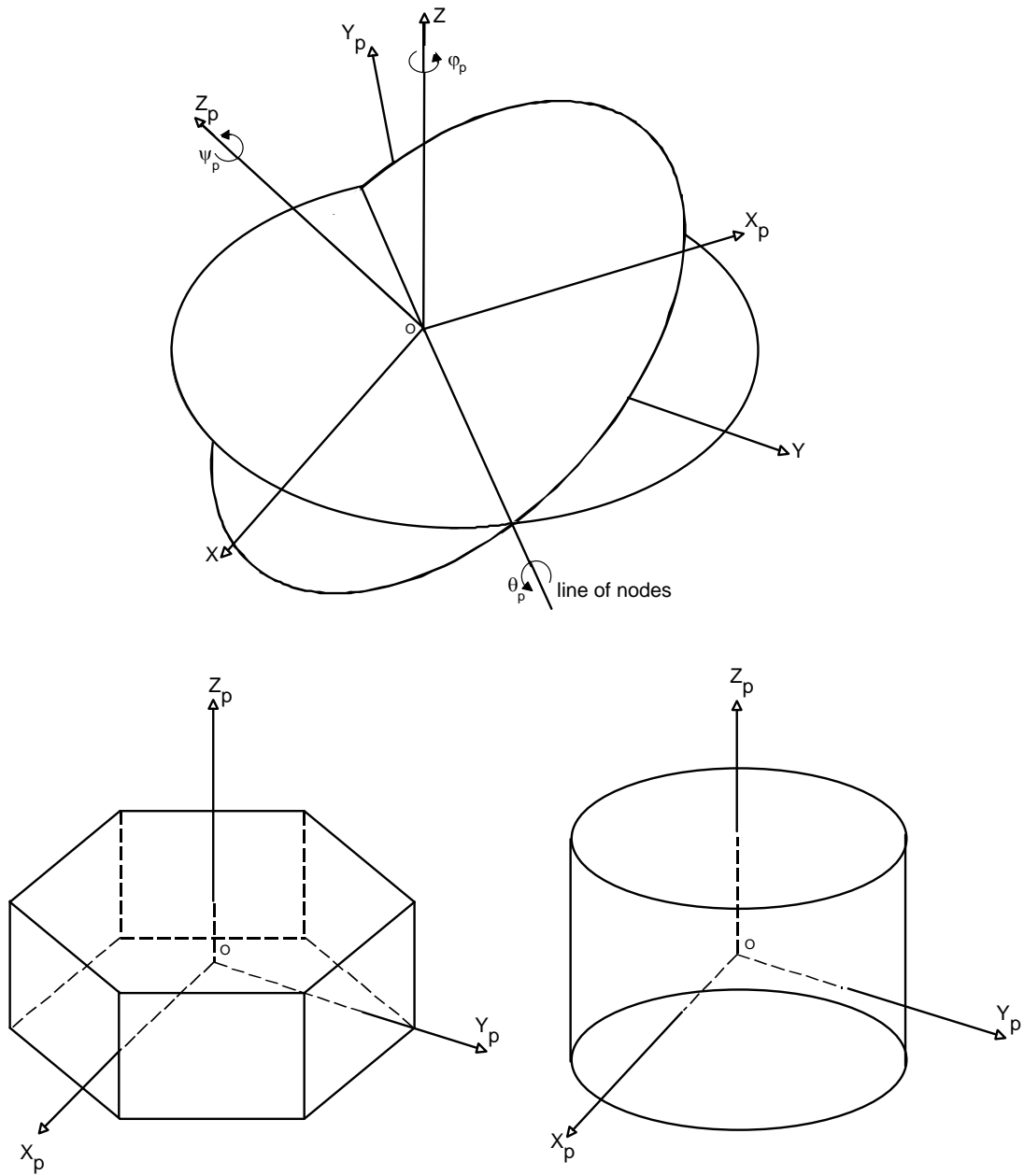
Fig. A.36. Definition of the Euler angler and orientations of geometries of hexagonal column and cylinder in particle coordinates.
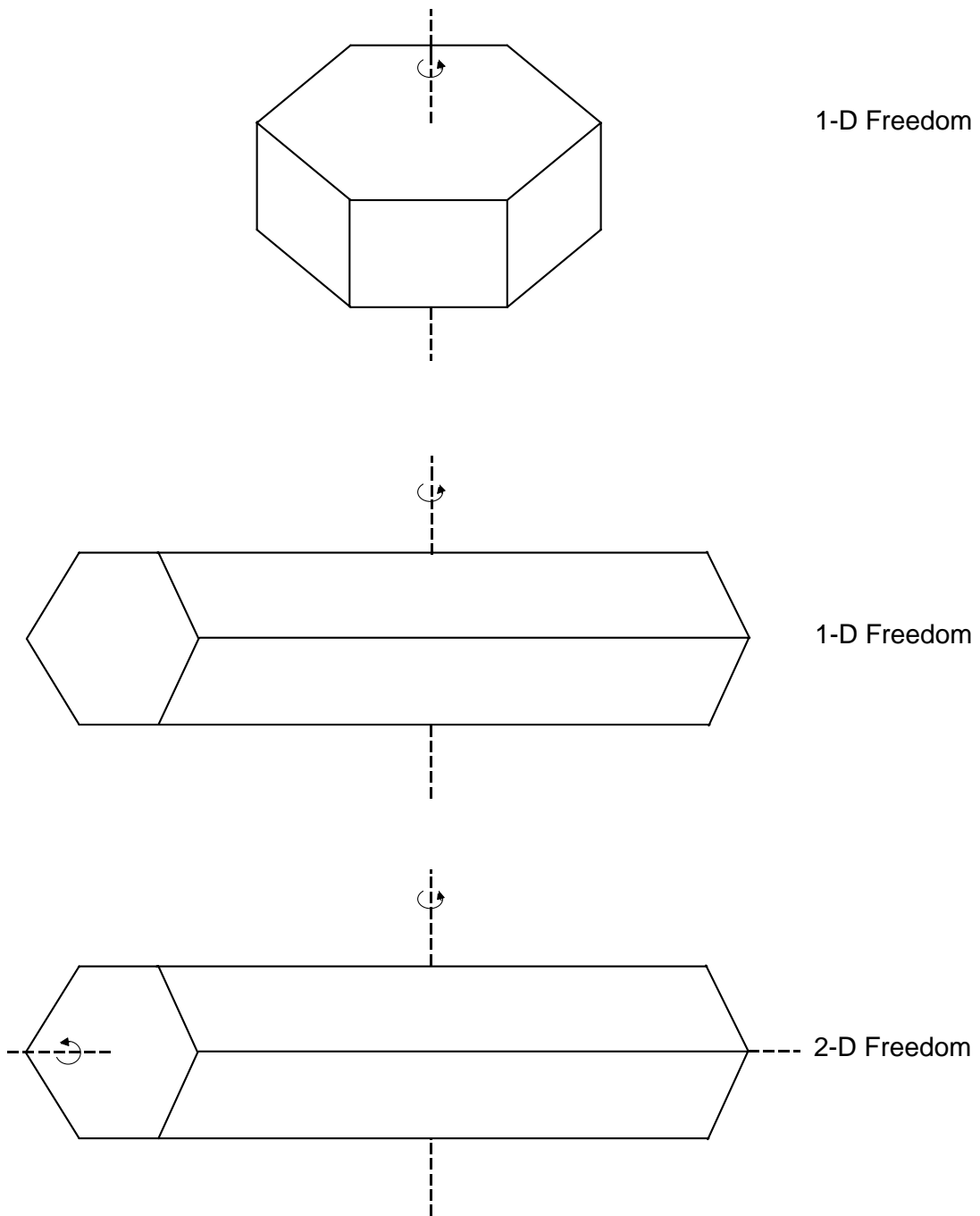
Fig. A.37 Orientation-averaging schemes for the hexagonal plate and column.
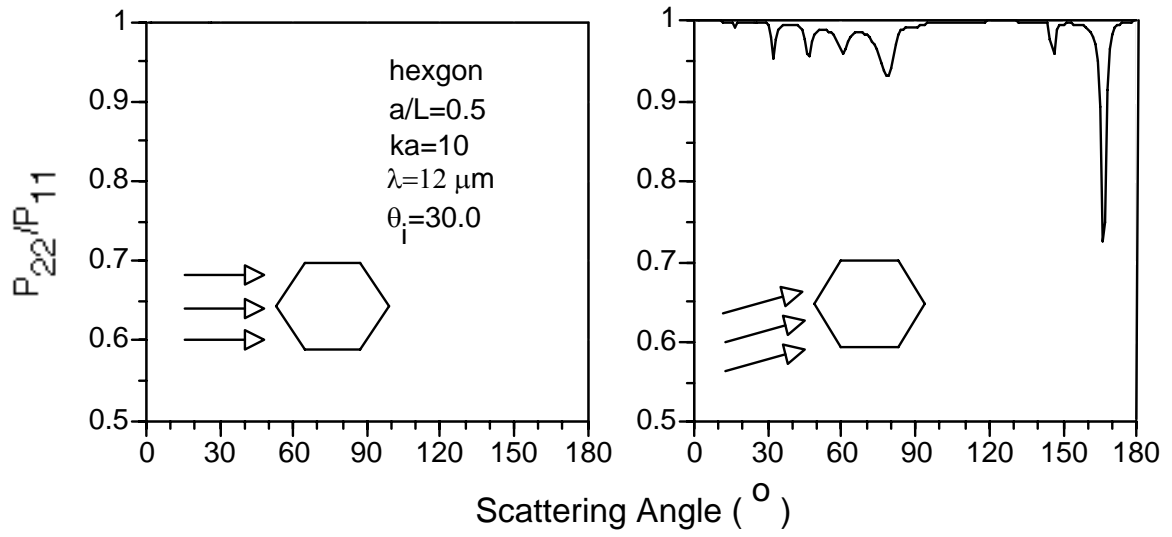
Fig. A.38. Phase matrix element, P_{22} of a fixed oriented ice hexagonal column with a unit aspect ratio at a wavelength of 12μm at an incident angle of 30°.
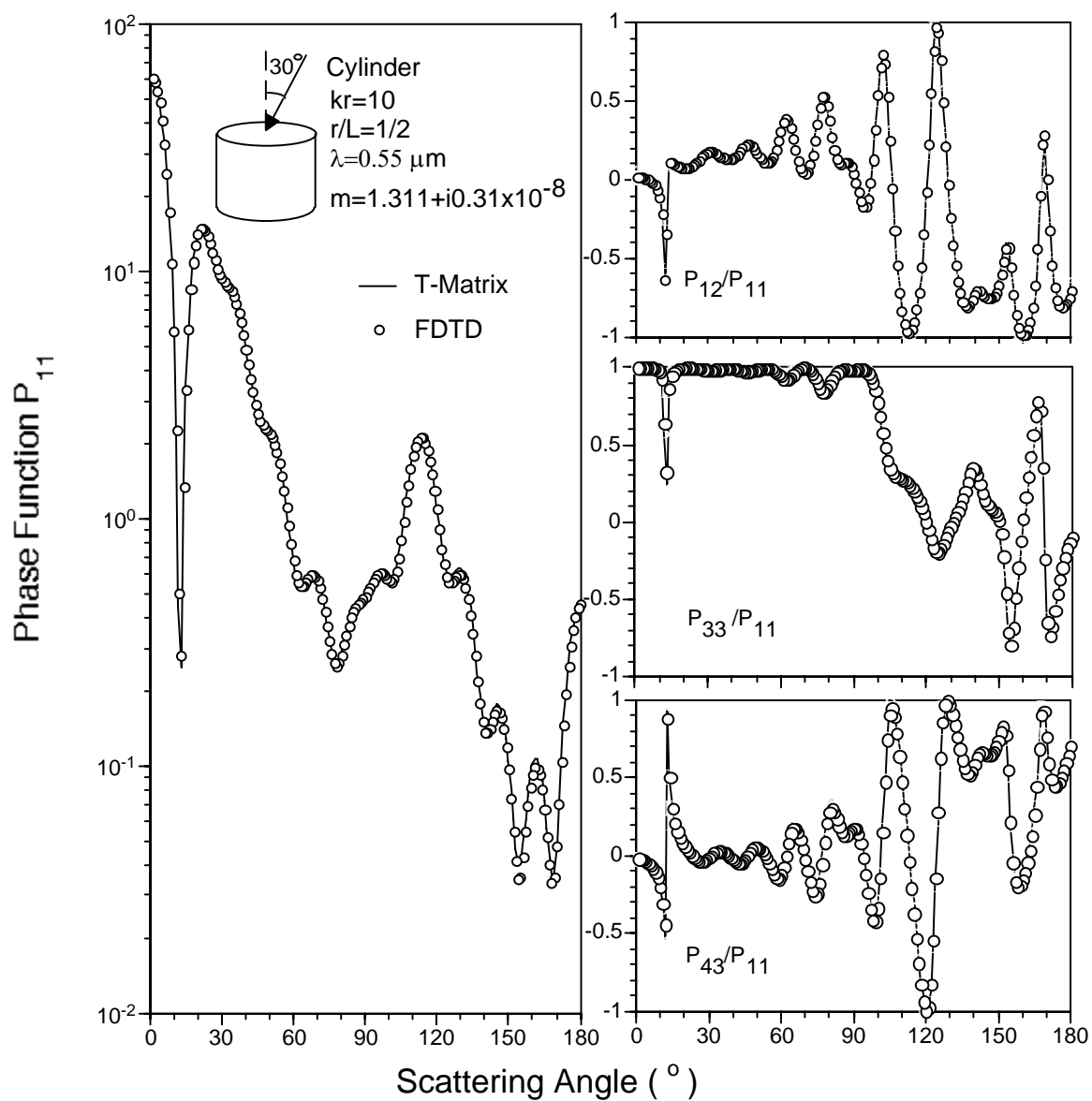
Fig. A.39. Phase matrix elements, P_{11}, P_{12}, P_{33} and P_{34} of a fixed oriented ice cylinder with a unit aspect ratio at a wavelength of 0.55μm at an incident angle of 30°.
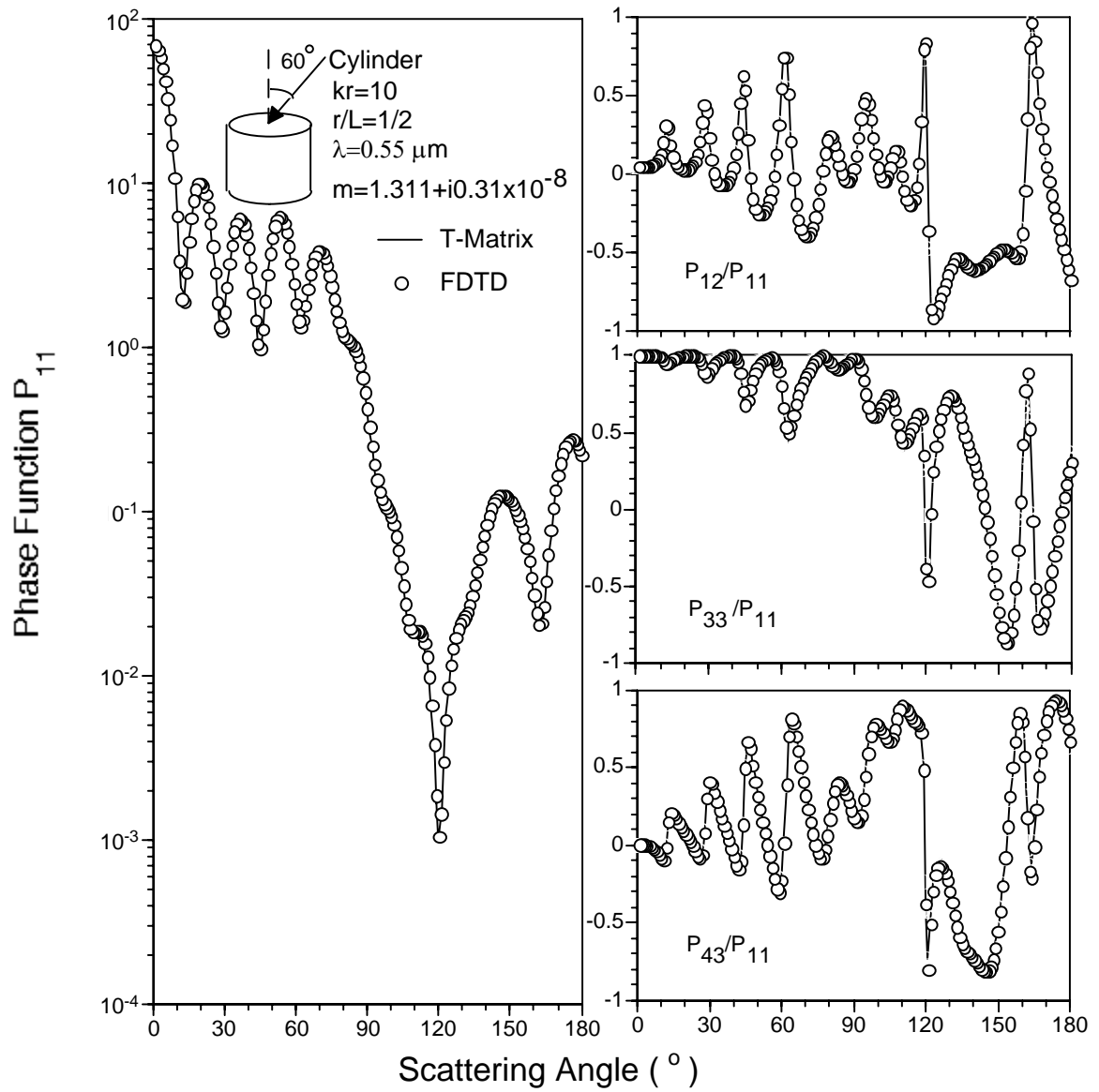
Fig. A.40. Phase matrix elements, P_{11}, P_{12}, P_{33}, and P_{34} of a fixed oriented ice cylinder with a unit aspect ratio at a wavelength of 0.55μm at an incident angle of 60°.
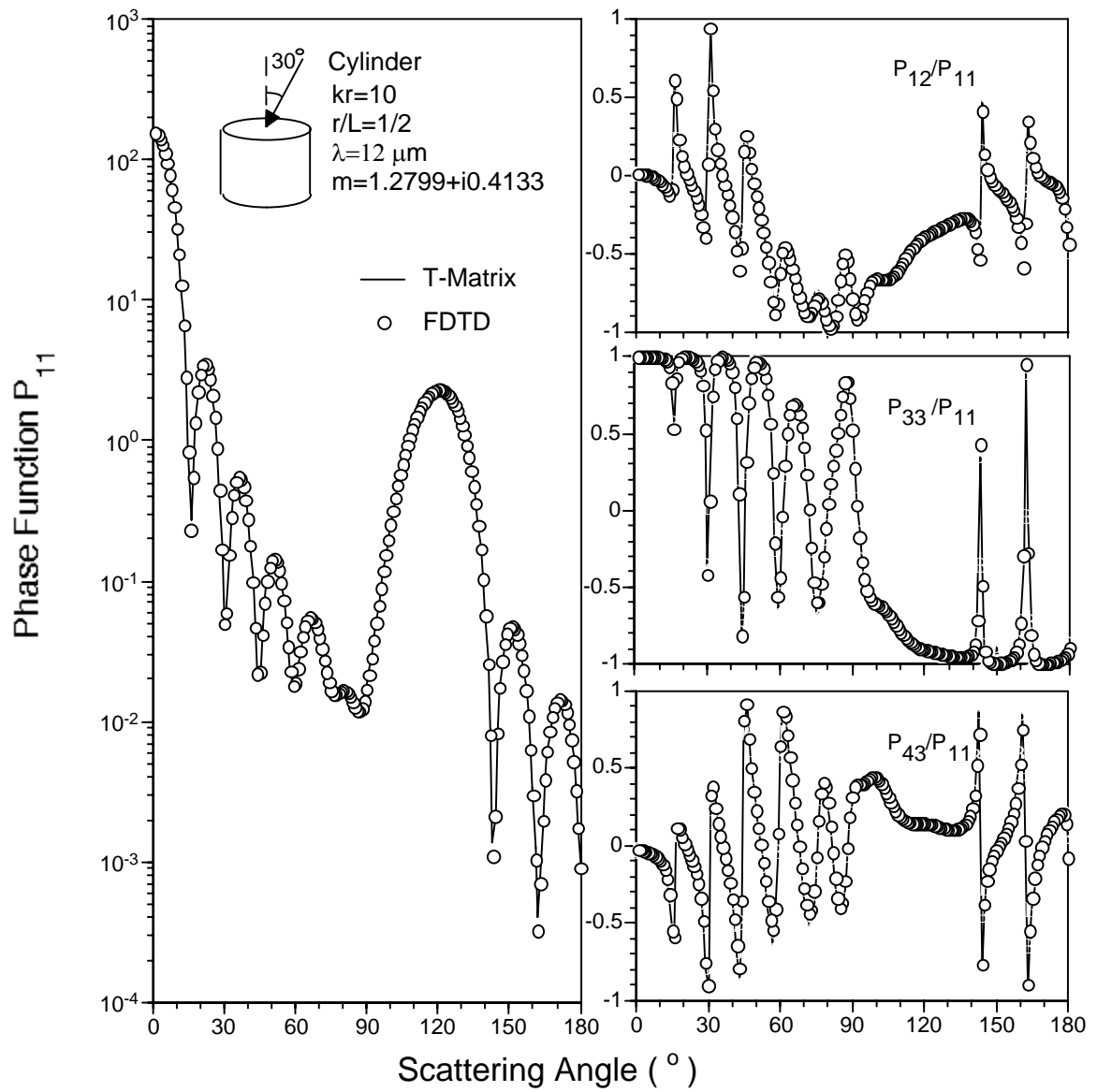
Fig. A.41. Phase matrix elements, P_{11}, P_{12}, P_{33}, and P_{34} of a fixed oriented ice cylinder with a unit aspect ratio at a wavelength of 12μm at an incident angle of 30°.
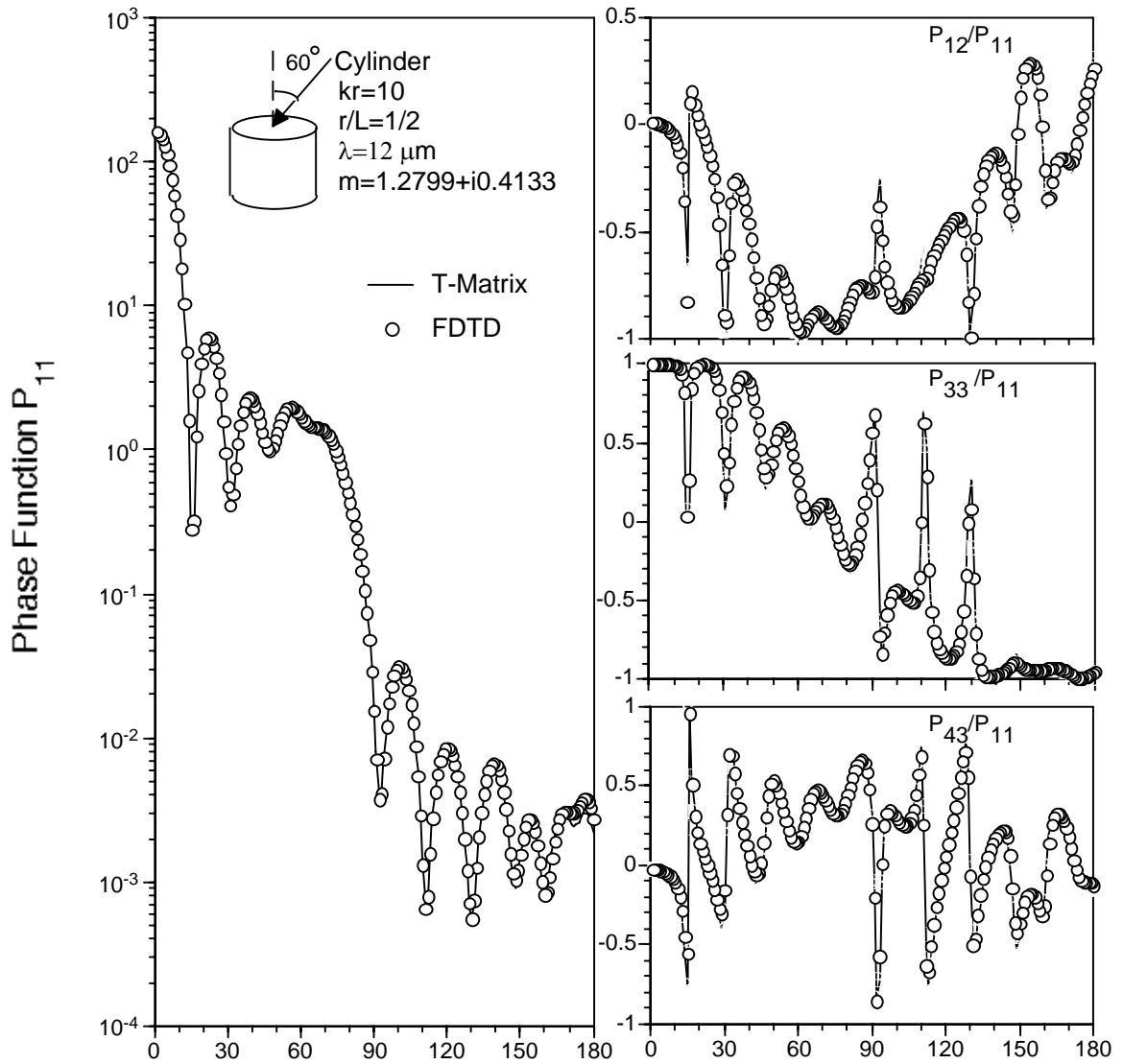
Fig. A.42. The phase matrix elements, P_{11}, P_{12}, P_{33}, and P_{34} of a fixed oriented ice cylinder with a unit aspect ratio at a wavelength of 12μm at an incident angle of 60°.
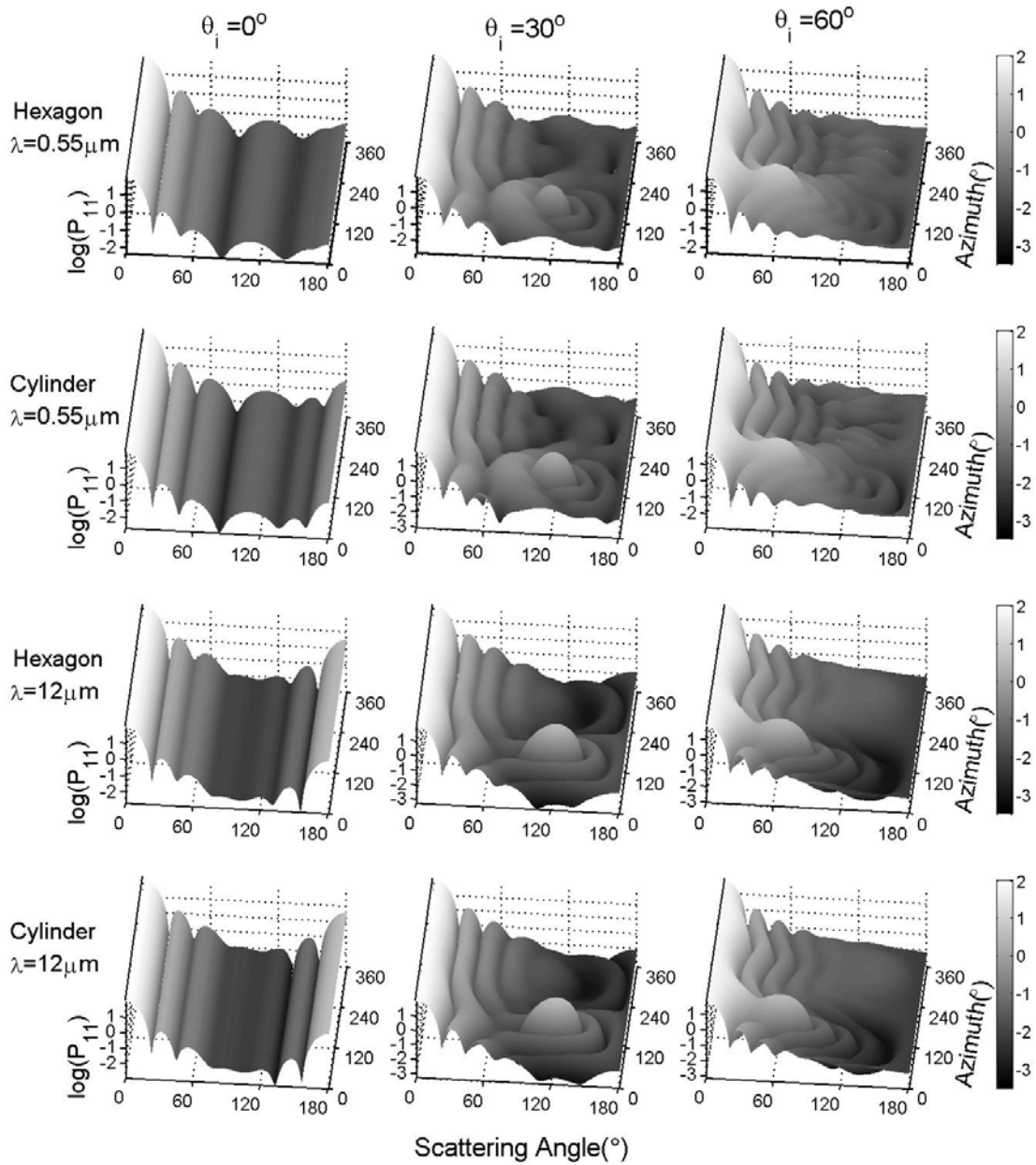
Fig. A.43. Phase functions of the horizontally oriented hexagonal plates and their equivalent cylinder plates with an aspect ratio of 0.25, wavelengths of 12μm and 0.55μm.
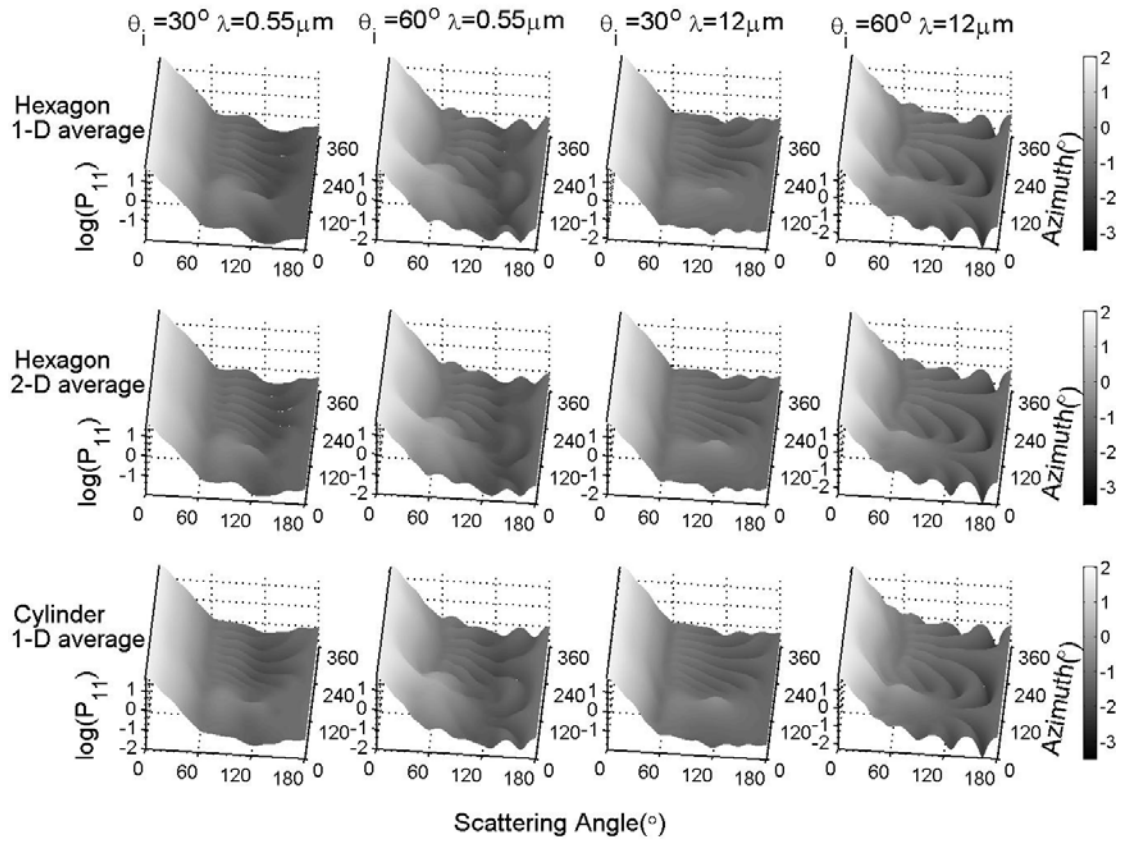
Fig. A.44. Phase functions of the horizontally oriented hexagonal columns and their equivalent cylinders with an aspect ratio of 3, wavelengths of 12 μm and 0.55 μm.
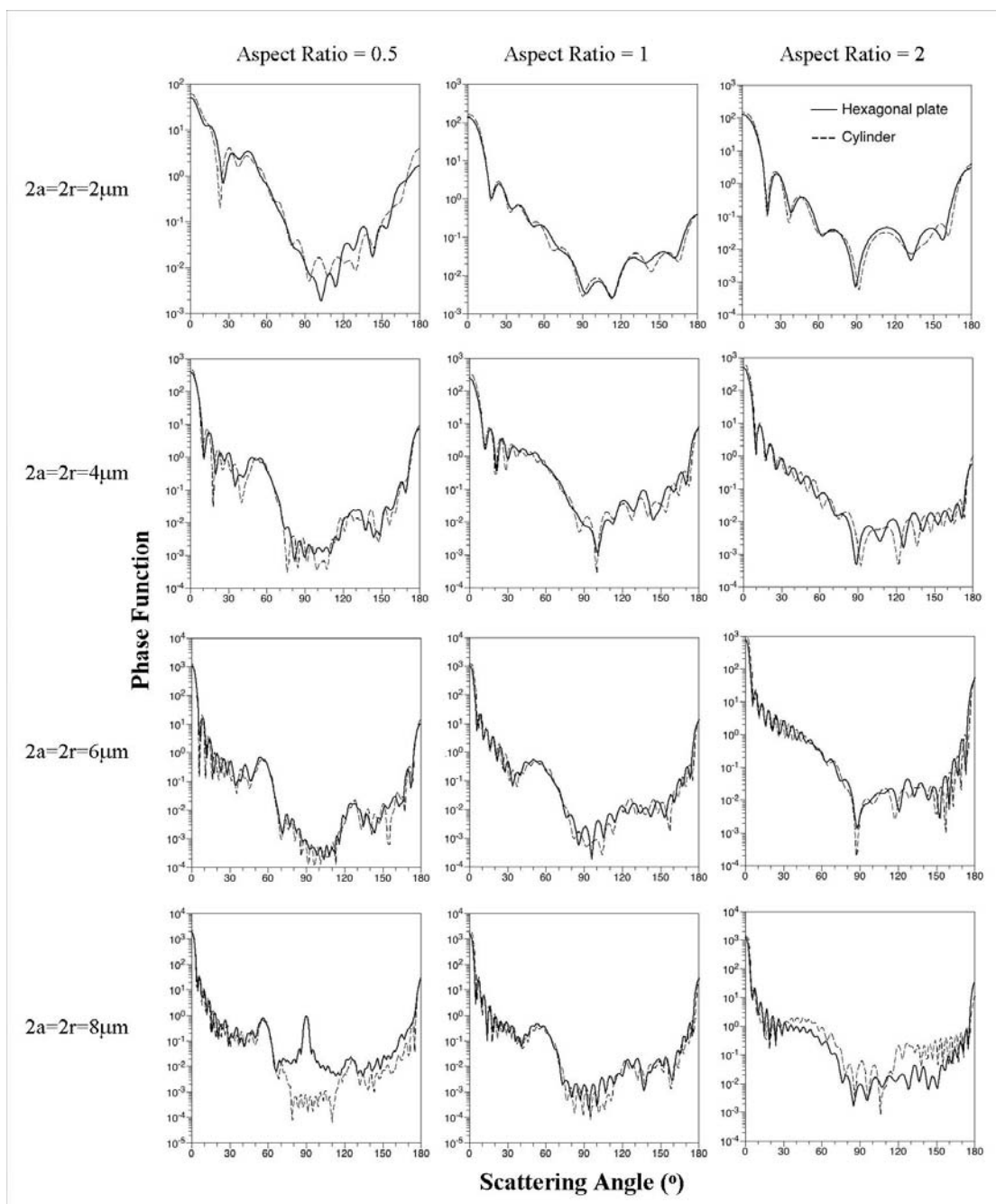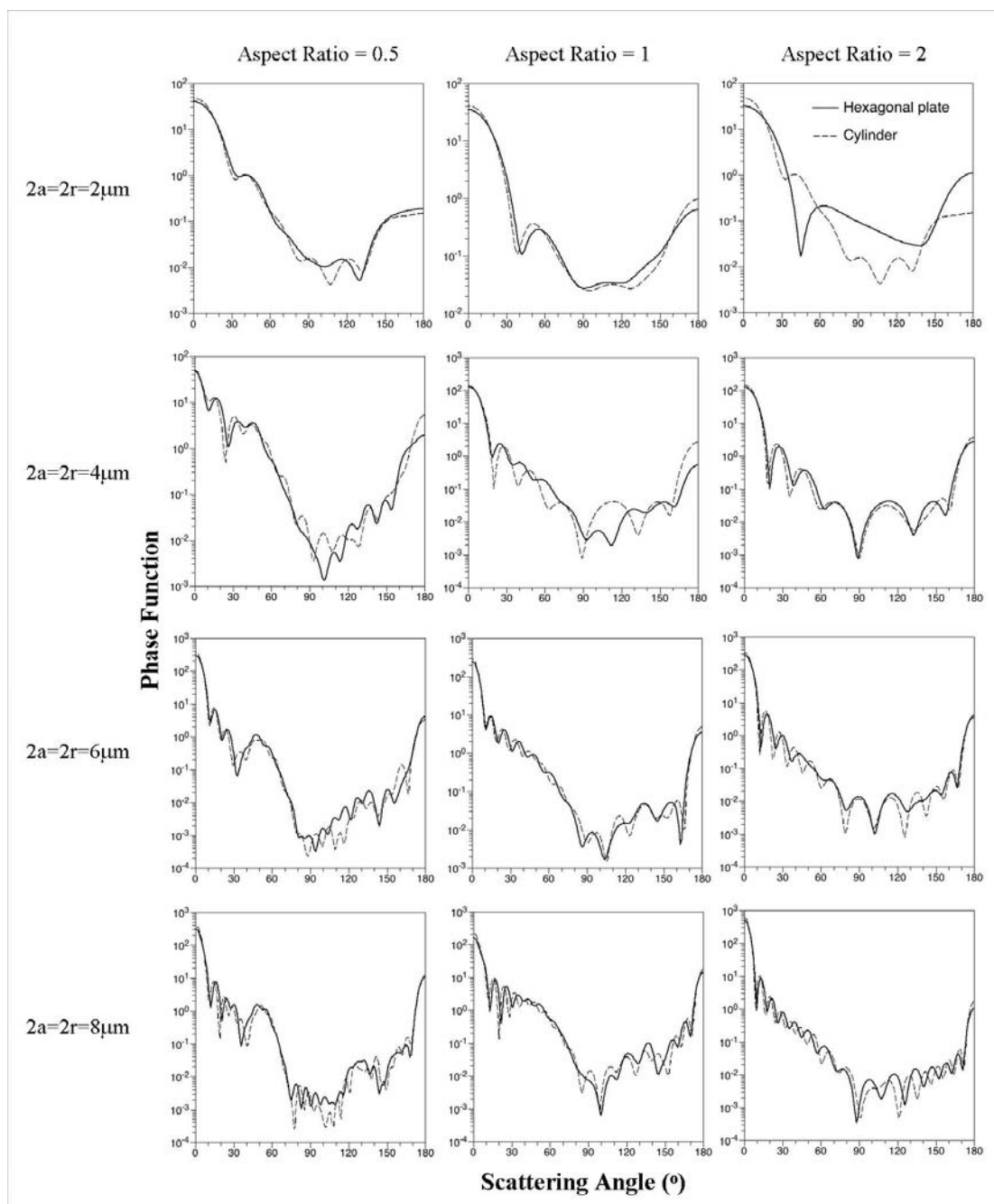
Fig. A.45. Phase functions of the horizontally oriented hexagonal plates and their equivalent cylinders with aspect ratios of 0.5, 1, 2 and the particle largest dimensions of 2 μm, 4 μm, 6 μm, 8 μm at wavelength of 0.532 μm.

Fig. A.46. Phase functions of the horizontally oriented hexagonal plates and their equivalent cylinders with aspect ratios of 0.5, 1, 2, and the particle largest dimensions of 2 μm, 4 μm, 6 μm, and 8 μm at wavelength 1.064 μm.
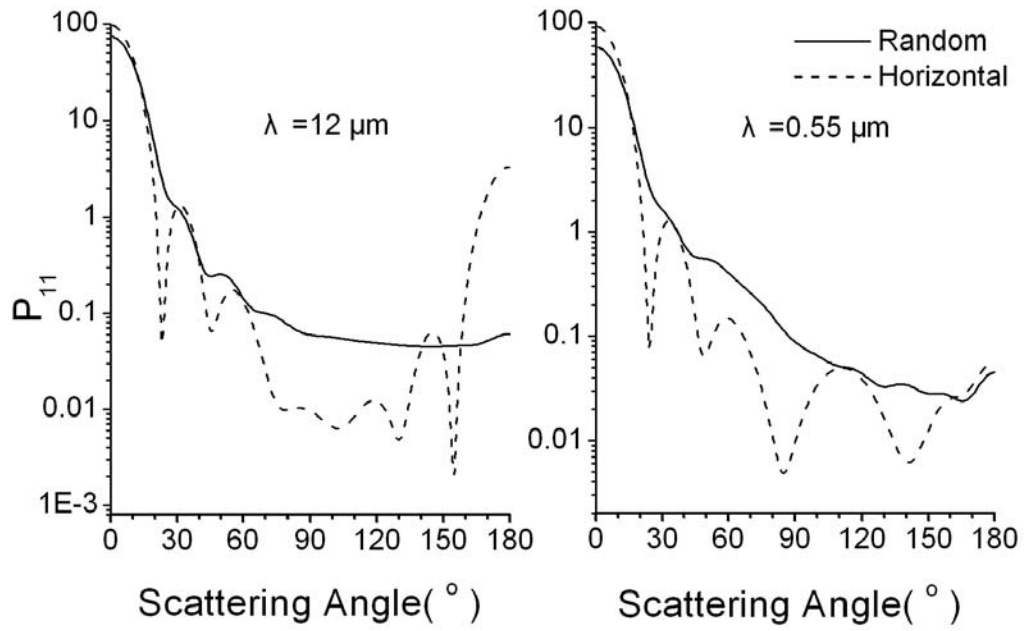
Fig. A.47. Normalized phase functions of the randomly oriented and horizontally oriented ($\theta_i = 0^{\circ}$) ice hexagonal plates with an aspect ratio of 0.25 at the wavelength of 12μm and 0.55μm.

VITA

Guang Chen received a B.S. in physics from Jilin University, Jilin, China in August 1998. In 2003 Mr. Chen received a M.S. degree in electrical engineering from University of Southern California.

Mr. Chen continued his graduate studies in atmospheric sciences at Texas A&M University since August 2003 and received a Ph.D. degree in August 2007.

Mr. Chen can be reached by email at guang_c@hotmail.com or by contacting Dr. Ping Yang at pyang@ariel.met.tamu.edu in Department of Atmospheric Sciences, Texas A&M University, 3150 TAMU, College Station, TX 77843-3150.